A NUMERICAL STUDY AND OPTIMIZATION OF A MORPHING AND PITCHING

BOEING VERTOL VR-12 ROTORCRAFT AIRFOIL

A Thesis
Submitted to the Graduate Faculty
of the
North Dakota State University
of Agriculture and Applied Science

By

Thomas Michael Sprengeler

In Partial Fulfillment of the Requirements
for the degree of
MASTER OF SCIENCE

Major Department:
Mechanical Engineering

June 2022

Fargo, North Dakota

North Dakota State University

Graduate School

Title

A NUMERICAL STUDY AND OPTIMIZATION OF A MORPHING
AND PITCHING BOEING VERTOL VR-12 ROTORCRAFT AIRFOIL

By

Thomas Michael Sprengeler

The Supervisory Committee certifies that this ***disquisition*** complies with North Dakota

State University's regulations and meets the accepted standards for the degree of

MASTER OF SCIENCE

SUPERVISORY COMMITTEE:

Dr. Y. Bora Suzen

Chair

Dr. Jordi Estevadeordal

Dr. Yan Zhang

Dr. Friedrich Littmann

Dr. Forrest Ames

Approved:

July 11, 2022	Dr. Alan Kallmeyer
Date	Department Chair

ABSTRACT

The helicopter blade has not undergone any major change in design in recent history, only minor adjustments like swept blade tips, variable twist blade, and application of small gurney flap style trailing edge devices. With the advancement of technology in both hardware and software this research aims to show the development of a modern shape morphing airfoil, specifically for helicopter application by utilizing high power computing and advanced turbulence modeling to find optimal shape morphing regimes. The experimental development and testing of the new airfoils were performed at North Dakota State University. The result of this research show that a system was developed in order to optimize the flow over a rotorcraft airfoil using advanced CFD methods. Three initial shapes to include leading and trailing edge deflections were chosen for their increase in aerodynamic performance over a wide range of angles of attack.

ACKNOWLEDGMENTS

TABLE OF CONTENTS

LIST OF TABLES

LIST OF FIGURES

LIST OF ABBREVIATIONS

CFD...Computational Fluid Dynamics

LE..Leading Edge

TE..Trailing Edge

VDLE...Variable Droop Leading Edge

RANS...Reynolds Averaged Navier Stokes

URANS...Unsteady Reynolds Averaged Navier Stokes

SST..Shear Stress Transport

SA ....Spalart-Allmaras

SBES ....Stress Blended Eddy Simulation

LES ....Large Eddy Simulation

DNS...Direct Numerical Simulation

CCAST...Center for Computationally Assisted Science and Technology

PIV ....Particle Image Velocimetry

PSP..Pressure Sensitive Paint

UDF...User Defined Function

RAM ....Rapid Access Memory

CPU...Central Processing Unit

AoA...Angle of Attack

TKE...Turbulent Kinetic Energy

BWT..Blower Wind Tunnel

LIST OF SYMBOLS

α ....Angle of attack

Re ....Reynolds number

C_l ....Coefficient of lift

C_d ....Coefficient of drag

C_f ....Coefficient of skin friction

Cp ....Coefficient of pressure

C ....Chord length

k ....Turbulent kinetic energy

ω ....Specific dissipation

γ ....Intermittency

Re_θ ....Momentum thickness Re

ρ ....Density

μ_t ....Turbulent viscosity

$\overline{u'u'}$ ....Reynolds stress X

$\overline{v'v'}$ ....Reynolds stress Y

$\overline{w'w'}$ ....Reynolds stress Z

f ....Frequency

$\emptyset$ ....Starting phase

U_∞ ....Free stream velocity

l ....Turbulent length scale

k_r ....Reduced frequency

Δx_{max} ....Max mesh edge length in X direction

L ....Length of domain

N ....Number of cells in X direction

LIST OF APPENDIX FIGURES

1. INTRODUCTION[1]

1.1. Introduction

The control of flow over an airfoil using camber morphing flight surfaces dates back to the early 1900s to the beginning of manned flight. Traditionally a trailing edge flap or camber morphing device is used to deflect a certain percent of chord on the aft of the airfoil downward in order to increase the lift for lower speed flight like take-off and landing. The increase in lift can be correlated to the increase in airfoil camber when the trailing edge devices are deployed. Around the same time that these trailing edge devices were being utilized on airplane wings, there was another advancement in leading edge devices known as slats, a slat is a device that droops a certain percentage of the chord in the front portion of the airfoil, the main characteristic of a slat is to keep flow attached at higher angles of attack. Thus, the airfoil can delay stall speed allowing for high lift and low speed flight. (**Weisshaar13; Murat19**)

1.2. Objectives

The major goal of this research is to develop a numerical analysis procedure for optimizing flow control of a dynamic morphing and pitching airfoil. The research funded by the Navy outlined the use of the Boeing Vertol VR-12 airfoil for application in full scale rotorcraft. The computational analysis will be used as a guide for the experimental analysis. Experimental design, manufacturing, and testing will be performed by Dr. Jordi Estevadeordal and William Refling in the Advanced Flow Diagnostics lab at NDSU. (**Refling22**) First, using XFLR5 analysis of the shape modifications to the VR-12 airfoil 3 morphed airfoils will be selected for their increase aerodynamic performance. Then, Reynolds Averaged Navier Stokes or RANS

---

[1] The material in this chapter was co-authored by Thomas Sprengeler and Dr. Y. Bora Suzen. Thomas utilized the CFD simulations to lead the experimental group in the tests that they performed. Also, Thomas generated all computational data used in the comparison between experimental and computational data.

simulations at static angles of attack will be performed on the modified VR-12 shapes to validate the findings of the XFLR5 solver. Once completed unsteady RANS or URANS simulations will be performed to analyze the modified VR-12 shapes in different pitching regimes similar to what would be experienced by a rotorcraft airfoil. These tests will be done to provide preliminary insight into where the specific shape changes show the greatest improvement in the pitching regime. Development of a simulation to include a dynamic morphing VR-12 airfoil will be developed in order to look at how the dynamic shape changing of the VR-12 airfoil will affect the flow field. Initial morphing tests using the data found in the static pitching tests will be used to study the benefit to aerodynamic performance as well as the effect of the morphing airfoil in the dynamic stall phenomenon.

1.3. Application

The application of this research is aimed at a full scale rotorcraft, but, due to limitations of the experimental testing that coincides with this study, the Reynolds number and Mach number tested are *Re*=250,000 and *Ma*=0.1. These values are substantially lower than the wide range of Reynolds numbers and Mach numbers experience across the span of a full scale rotorcraft blade. The intent is to scale up these values as the equipment and opportunities become available via a rotor test stand that will represent the rotating blades of a rotorcraft as well as an upgraded closed loop wind tunnel. The other application of this study is smaller, lighter, and slower aircraft such medium sized unmanned helicopters such as the Northrop Grumman MQ-8 Fire scout or even smaller commercial drones. All rotorcrafts experience the same dynamic flow field through the rotation of the blade as well as the issues associated with noise and vibration. These are all issues this research aims to improve and can be scaled and applied to different systems.

2. REVIEW OF AIRFOIL CONTROL SURFACES AND CFD MODELING

2.1. Traditional Fixed Wing Camber Morphing Devices

Traditional camber morphing devices include heavy hydraulic powered mechanisms that utilize pilot input in order to adjust the amount of deflection in the leading and trailing edges. These devices are also traditionally slow to adjust as they are only being utilized in takeoff and landing scenarios and not deployed during cruise flight as the free stream flow is relatively uniform for traditional fixed wing airplanes. Although the hydraulic systems are very heavy in the wing, they are very robust and unlikely to fail with failure modes developed to maintain usability in the event of a hydraulic failure. (**Wang16**)

There are many different types of flaps and slats, slotted, split, plain, etc., but they all rely on the same traditional methods of slow hydraulic deployment as well as more complicated wing shapes and some problems with parasitic drag and unfavorable flow characteristics due to the discontinuous design of the airfoil due to the inclusion of flaps and slats. (**Young47**)

The methods discussed however are only seen in fixed wing application, in order to incorporate a similar style of camber morphing devices to rotorcraft blades will require changes to the methodology. The rotorcraft flow field is very dynamic and constantly changing, the new system will not only have to remain robust but also very fast.

2.2. Rotorcraft Characteristics

Unlike fixed wing aircraft, rotorcraft do not consistently encounter undisturbed free stream flow, in fact the advancing blade will be interacting with the turbulent wake of the blade in front of it. This means that at every azimuth angle the blade will be encountering a slightly different flow field than it did at the previous angle. This requires the pitch of the airfoil to constantly be optimized for the flow conditions it is encountering, this is done via the swash

plate at the rotor hub. This swash plate will induce the pitching of the rotor blade, such that one rotation equals one pitching cycle of the blade. (**Poling89; Costes12**)

This constantly changing flow field is where rotorcraft can benefit from introducing leading and trailing edge deflections throughout the azimuth, unlike a fixed wing aircraft that only utilizes the control surfaces at take-off and landing. Traditional methods of leading and trailing edge manipulation are not applicable to rotorcraft application due to the smaller size of the rotor blade compared to a fixed wing, as well as the weight of the mechanism increasing the hub load and changing the natural frequencies of the blade. (**Fincham19**)

While undoubtedly rotorcraft flight encounters many complexities that are absent in fixed wing flight, there are some simple methods in which rotorcraft manufacturers have been able to implement flow control methods in rotorcraft applications.

2.3. Current Flow Control Methods in Rotorcraft

Current helicopters utilize gurney flaps which are a small vertical tab attached to the trailing edge of the rotor blade and extend downward. This is a passive method of increasing the lift of the airfoil without drastically increasing the weight or complexity of the system. With a lack of active methods of controlling the aerodynamic characteristics of the rotorcraft airfoil there has been recent increase in research on this subject. (**Yee07**)

While the current methods remain relatively basic in comparison to that of fixed wing aircraft, in recent years there has been renewed interest in developing methods of flow control and flight surfaces specifically aimed at optimizing and increasing performance for rotorcraft.

2.4. Advancements in Rotorcraft Camber Morphing

Current research is looking at how camber morphed rotor blades can improve aerodynamic characteristics such as dynamic stall as well as the improvements in vibration and

noise. The Martin, P. B., et al. paper of variable droop leading edge (VDLE) has proven that camber morphing of the leading edge can be beneficial in controlling and reducing the dynamic stall phenomenon of a rotor blade. This is achieved by deflecting downward the first 25 percent of the chord length. The experimental results showed very good agreement with the CFD results utilizing the Spalart-Allmaras one equation turbulence model. The testing included a static drop of the leading edge combined with an unsteady pitching motion of the airfoil. (**Martin03)**

Glaz et al., studied partial spanwise flaps that are simulated to precisely adjusted at different angles along the spanwise direction of the rotor blade to improve performance and reduce vibration. The research showed that a partial span flap on the trailing edge of a rotor blade can be used to actively control the performance of the airfoil being optimized for either a reduction in power consumption or a reduction in overall vibration in the blade by substantial amounts. With further investigation needed in the area there could also be more beneficial properties of these trailing edge flaps. (**Glaz08**)

Maughmer et al., implemented active gurney flaps near the trailing edge that were analyzed using CFD methods. The CFD model utilized the Spalart-Allmaras one equation model turbulence model. These studies utilized a static gurney flap deployed at different angles relative to the chord line at specific regions in the azimuth. The goal of the research being to develop a scheduled deployment of the gurney flap at different azimuth angles to optimize flight characteristics. The results of the CFD study showed great improvement over the baseline airfoil at high thrust and high speeds showing overall better flight characteristics with the gurney flap than without. (**Maughmer08**)

Gandhi et al., performed simulations on an airfoil with an extendable trailing chord, this airfoil was designed to increase performance of the rotor as well as widen the envelope of the

5

helicopter. The extendable chord came out of the trailing edge a prescribed amount with 2° of angle downward. This airfoil did not show improvements in performance at lower speeds but the operational speed of the airfoil increased from 115 knots to 133 knots when operating at 8000 feet. (**Khoshlahjeh14**)

The above cases all study methods of flow control and camber morphing of rotorcraft airfoils in various ways. The common short coming is the lack of dynamic shape changing of the airfoil itself. While some may represent unsteady flow by way of pitching the airfoil similar to that of a rotorcraft, they are testing the shape optimization as static cases under various flight conditions i.e., Reynolds number, angle of deflection, Mach number. This is where the need for a system of testing a dynamic shape changing and pitching rotorcraft airfoil arises.

2.5. Active Shape Morphing

Active shape morphing of an airfoil during an unsteady CFD simulation provides great benefit over the traditional method of studying shape deflections in a steady manner and interpreting results based on a series of static shape morphed airfoils, with the ability to actively shape morph an airfoil during an unsteady simulation the results will better represent the idea of an active shape morphing airfoil. Marouf et al., performed unsteady CFD simulation of a shape morphing airfoil to actively adjust the camber of an airfoil to optimize the Lift/Drag values before introducing other methods of flow control. These simulations used fluid structure interaction (FSI) to impose the morphing on the airfoil. (**Marouf20**)

Abdessemed et al., simulated a NACA0012 actively morphed using user defined functions in ANSYS Fluent which utilizes code written in C+ to control the shape of the airfoil via interpretation of the mesh nodes as X, Y, and Z coordinates that can be manipulated via the UDF. In this case the airfoil was studied at near stall scenarios, with results showing that the

dynamic morphing trailing edge did not prevent stall with the studied parameters. The research did show a relationship between morphing frequency and the drag coefficient spikes induced by the morphing trailing edge. (**Abdessemed18**)

Research by Mishra et al., studies a trailing edge flap that can dynamically change to help reduce the effects of dynamic stall on the retreating blades of a rotor. They use a RANS CFD solver that also dynamically changes the mesh each time step to adjust for an increase or decrease in the trailing edge flap deflection. The results of these simulations showed a great reduction in the effects of dynamic stall in the retreating blade when the activation of the flap occurred and the azimuth angle of 300°. (**Mishra09**)

Based on the previous research in the field it is possible to take a goal of shape changing airfoils and apply that to the theory of shape optimizing an airfoil specifically for rotorcraft application and develop a CFD model and method of finding optimized deflection angles and frequencies to control the flight characteristics of that airfoil.

Research performed by Marouf et al., research done in industry and academics often utilizes lower accuracy and highly efficient Reynolds Averaged Navier Stokes (RANS) simulations, while some research similar to the work done by Abdessemed et al. utilize a hybrid method that utilizes a combination of Large Eddy Simulations (LES) and RANS simulations for higher accuracy while maintaining higher efficiency.

2.6. CFD Turbulence Modeling

Much of the CFD done on rotorcraft flow control includes simulations utilizing lower order RANS turbulence model like the one equation Spalart-Allmaras model. While this and similar models are widely used in industry applications for their accuracy vs computational cost relationship, they do not give a complete picture of the turbulent structures in the flow field. For

this reason, hybrid turbulence models have been developed that utilize both Large Eddy Simulation (LES) and Reynolds Averaged Navier Stokes (RANS) models. Using just LES models result in very accurate simulations where the user can control the definition in turbulent structures based on the definition of the grid, but the cost of this is a large increase in computation time. The RANS model cannot solve the wide range of turbulent structures that LES can, but it can provide accurate results very efficiently which is the reason for its wide acceptance in industry applications. (**Menter16; Menter21**)

The use of the hybrid methods allows the LES model to be used to capture the turbulent structure away from the wall where LES is more computationally efficient and utilize RANS models near wall where the LES is less computationally efficient. This will allow for a great decrease in computational time when compared to a traditionally LES simulation while also providing a lot more detail in the turbulent structures than is possible with a RANS only simulation. (**Menter16; Menter21**)

This research aimed to use a continuous leading and trailing edge deflections with the ability to morph independently of one another in order to attempt to control the flow and improve the aerodynamic characteristics of the airfoil. The computational model will begin development using potential flow solver methods and progress into RANS, URANS, and hybrid methods, with the development of a shape morphing simulation in order to study the effects of a dynamic moving airfoil under various conditions, effectively utilizing aspects from almost all the aforementioned research while channeling the different aspects to apply to the specific case being studied.

3. SHAPE EVALUATION AND SELECTION

3.1. Leading and Trailing Edge Deflection

Initial analysis of the VR-12 was performed using XFLR5 (**XFLR521**). XFLR5 utilizes the flow5 solver, XFLR5 is optimized for low Reynolds number simulations. The built-in tools allowed for modification to airfoil camber, thickness, leading edge, and trailing edge deflections. The use of XFLR5 viscous calculations allowed for rapid 2D testing of different shape modifications to the VR-12. A shape change could be added and tested for a range of Reynolds numbers and angles of attack very rapidly. Although not a comprehensive analysis, it provided the initial insight into how the VR-12 may react to different shape modifications. Further analysis was performed using Ansys CFX to validate the results in XFLR5. The initial tests were conducted for three different Reynolds numbers, 125,000, 175,000, and 250,000 and a range of angle of attack from -10° to 30° based on previous research. (**Goecks18; De Hugues93**) Using work previously done on the VR-12 airfoil as a starting point an initial leading edge deflection at 25% chord and trailing edge deflection at 85% chord was selected. (**De Hugues93; Wang19; Martin03**)

These initial shape changes were used to guide the experimental analysis of the same airfoil. The experimental testing, design, and manufacturing of the shape modified airfoils was performed at NDSU by Dr. Jordi Estevadeordal and William Refling. Utilizing the findings of the potential flow solver results the experimental group will begin manufacturing the same airfoil shapes in order to compare experimental data with the computational data. (**Refling22**)

The deflections can be visualized below in figure 1 where the red line represents the baseline airfoil, and the black line represents the new airfoil with leading and trailing edge

9

deflections. The leading edge will deflect counterclockwise with an increase in positive angle. The trailing edge will deflect clockwise with an increase in negative angle.
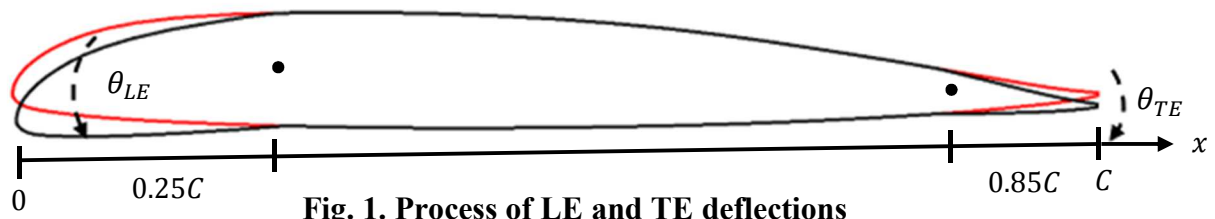
Fig. 1. Process of LE and TE deflections

Then using XFLR5 to simulate these airfoils with 1° to 12° of leading and trailing edge deflection at a clockwise and counterclockwise directions respectively, the airfoil shapes can be seen below in figures 2 and 3.

Fig. 2. TE deflection of VR-12 airfoil

Fig. 3. LE deflection of Boeing VR-12 airfoil

In order to decide which angles of deflection to use as the initial designs the aerodynamic characteristics of these airfoils were analyzed at Re=250,000 as per the capabilities of the wind tunnel in the NDSU Advanced Flow Diagnostics Lab.

(a) Lift coefficient variations

(b) Drag coefficient variations
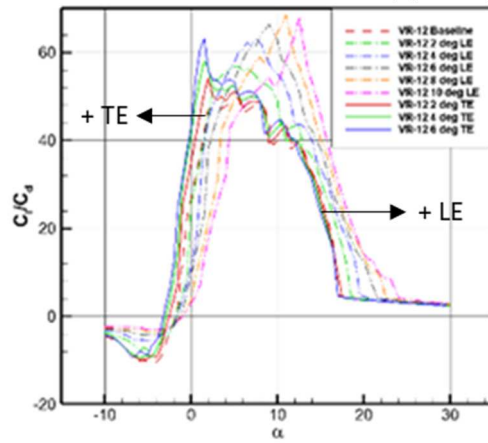
(c) Lift/Drag variations

Fig. 4. Effects of LE and TE deflections on VR-12 airfoil aerodynamics: (a) C_l vs α, (b) C_d vs α, (c) C_l / C_d vs α

Above in Figures 4a, 4b, and 4c are the computed lift and drag coefficients for the 2 shape morphed airfoils with the respective degree of LE and TE deflections alongside 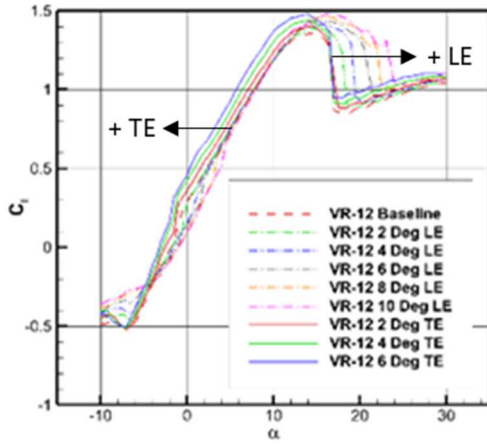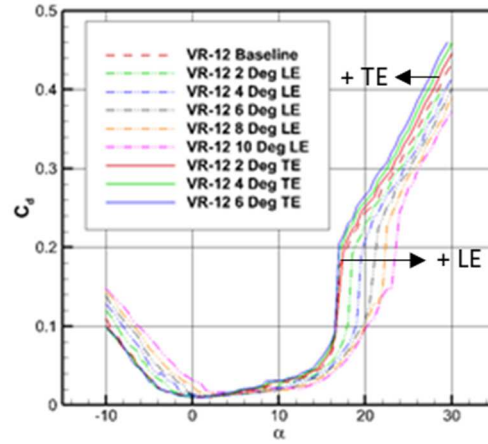the baseline VR-12 airfoil. The arrows represent the trending direction the LE and TE results. In figure 4a the LE deflection shows an increase in $C_{l_{max}}$, resulting in the delay of the stall angle of attack to nearly 20°, while the trailing edge shows in increase in C_l at lower angles of attack reducing the stall angle of attack to nearly 12°. In figure 4b the coefficient of drag is analyzed with the LE deflection showing an increase in C_d before angle of attack of 5° and decrease in C_d after 5° of angle of attack. While not as prevalent the TE deflection decreases C_d prior to 5°

11

angle of attack and increases C_d after 5° angle of attack. In figure 4c the C_l/C_d shows that with a LE deflection the C_l/C_d performance is increased at higher angles of attack (>5°) while the TE deflection increases C_l/C_d performance at lower angles of attack (<4°). From this data two deflections where choses, a 6° LE deflection and a 4° TE deflection. These were chosen based on their complimentary and broad coverage of C_l/C_d over the entire range of angle of attack. One important factor that played a role in this decision is the usable range of angle of attack, some deflections outperformed the chosen deflections, but it reduced the usable range of angle of attack, so the performance benefit would only be seen in very small ranges of angle of attack.

Below in figures 5a, 5b, 5c, and 4d the aerodynamic characteristics of the chosen deflected airfoils, LE 6° and TE 4° and the baseline VR-12 airfoil are compared. In figure 5a the increase in lift over the baseline airfoil can be seen notably the TE deflected airfoil providing an increase in C_l at angles of attack less than 14° and the LE deflection providing increase in C_l at angles of attack greater than 14° while also increasing the stall angle of attack to nearly 20°. In figure 5d the TE provides reduced C_d at angles of attack less than 0° and the LE deflection provides reduced C_d at angles of attack greater than 0°. In figure 5c it is important to note that the C_l/C_d is increased over the entire engage of angle of attack, this shows the complimentary performance of the LE 6° and TE 4° deflection. In figure 5d showing C_l vs C_d it can be seen that C_d is greatly minimized in the region where values of C_l range from 0 to 1.

(a) Lift coefficient variations

(b) Drag coefficient variations
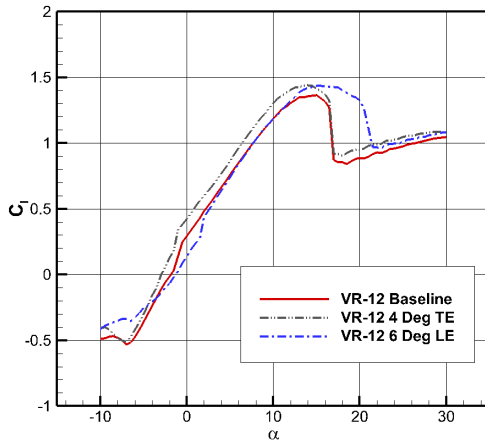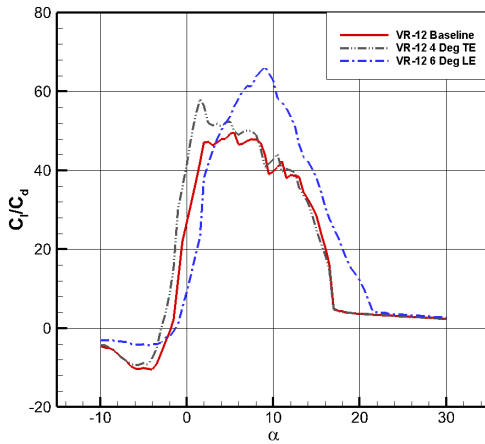
(c) Lift coefficient vs drag coefficient
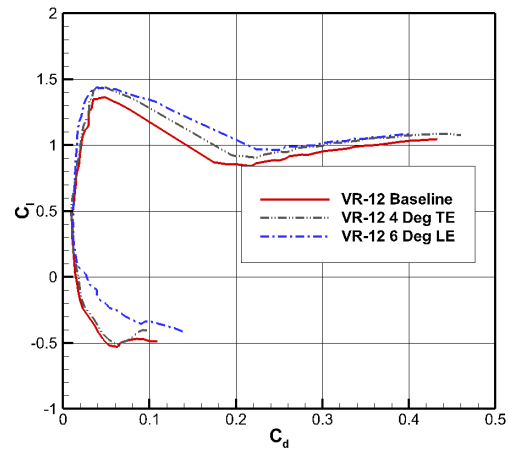
(d) Lift/Drag variations

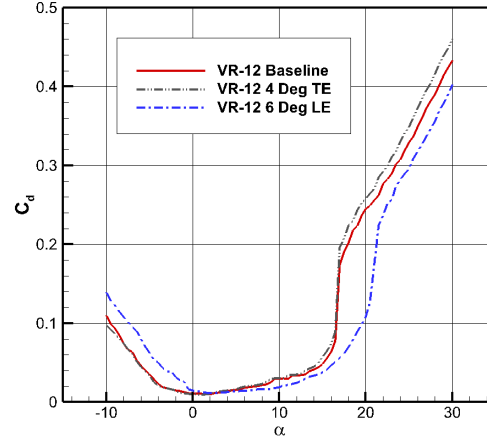**Fig. 5. Effects of 6° LE and 4° TE deflections on VR-12 airfoil aerodynamics: (a) C_l vs α, (b) C_d vs α, (c) C_l/ C_d vs α, (d) C_l vs C_d**

3.2. Combination Deflection

Next, the goal was to choose a fourth shape modification based on evaluations of a combination of LE and TE deflections together on a single airfoil that show an improvement in aerodynamic characteristics. In order to streamline the process, the initial locations of deflection remained the same, 25% chord for the LE and 85% chord for the TE, as shown in figure 6. The evaluation of these airfoils maintained the same flow conditions as the previous set of tests for the LE and TE deflections.
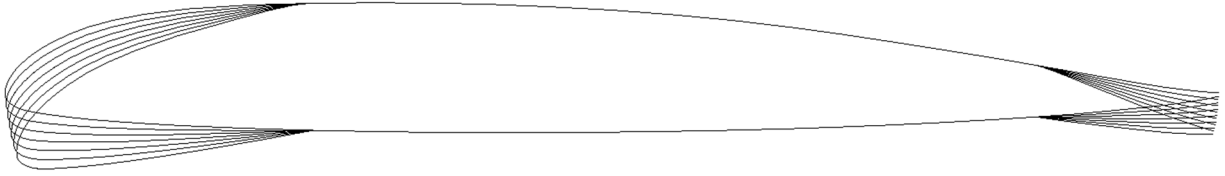
Fig. 6. Combined LE & TE deflections of VR-12 airfoil

Figures 7a through 7d show the comparison between aerodynamic characteristics of different combinations of leading and trailing edge deflection modifications as well as comparison to the baseline VR-12, the 6° LE, and 4° TE.

The comparisons in figure 7 indicate promising results for the utilization of a combination airfoil to help increase aerodynamic performance in areas between the benefit of the LE and TE deflections. Below in figure 7a it can be seen that the C_l is increased throughout the entire range of angle of attack from -10° to 23° angle of attack. In figure 7b, C_d is reduced near the middle range of angle of attack showing its benefit to cover ranges of angle of attack that the single LE or TE deflections lacked. Figure 7c shows the increase in performance of C_l/C_d from 4° to 16° angle of attack, this region corresponds to the region that the TE and LE airfoils showed a drop in performance. In figure 7d it is noted that the drag is minimal in a range of C_l values from 0.5 to 1.2.
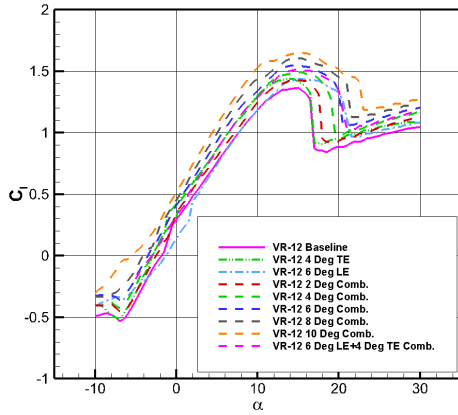
(a) Lift coefficient variations
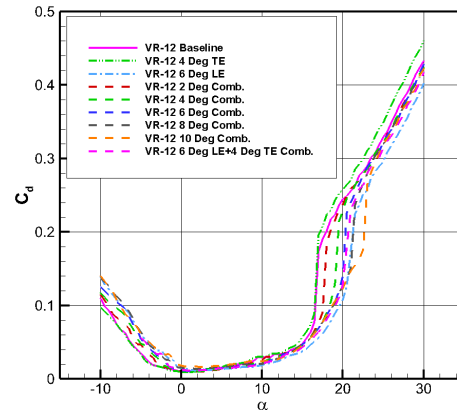
(b) Drag coefficient variations
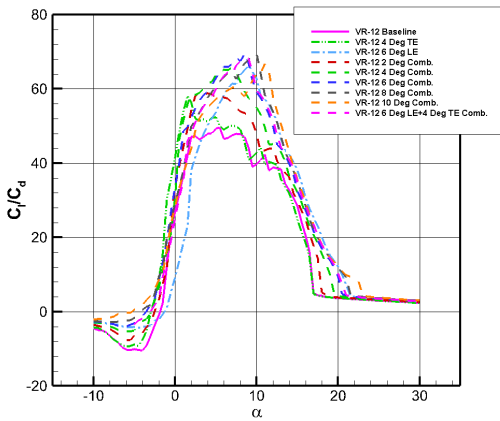
(c) Lift/Drag variations
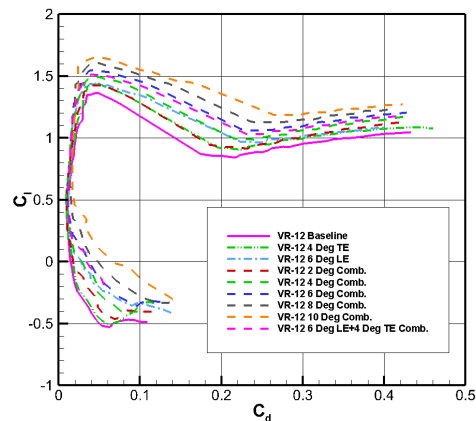
(d) Lift coefficient vs drag coefficient

Fig. 7. Effects of combined TE & LE deflections on VR-12 aerodynamics: (a) C_l vs α, (b) C_d vs α, (c) C_l / C_d vs α, (d) C_l vs C_d

From the data in figure 7 a fourth airfoil was chosen with a combination of a 6° LE and 4° TE deflection. This airfoil was chosen based on its aerodynamic performance in the region of angles of attack that the previous two airfoils lacked, as well as its ability to generate this increase in aerodynamic performance over a wider and more usable range of angle of attack.

The modified airfoils work together to show increase in aerodynamic performance across the entire range of angle of attack, in figure 8a through 8d shows the aerodynamic characteristics of the baseline VR-12 and the 3 shape modified airfoils. Figures 8a and 8b show the benefit of

increasing C_l and decreasing C_d over the entire range of angles of attack. In figure 8c it is notable that the C_l/C_d performance shows clear evidence of the ability of the 3 modified airfoils to work together to provide an aerodynamic performance increase at all angles of attack in the range from -10° to 30°. Lastly in figure 8d it shows a decrease in C_d for a wider spectrum of values of C_l.
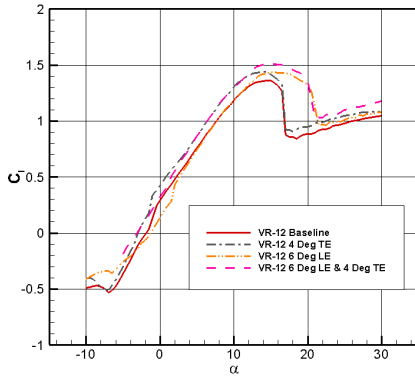
(a) Lift coefficient variations

(b) Drag coefficient variations
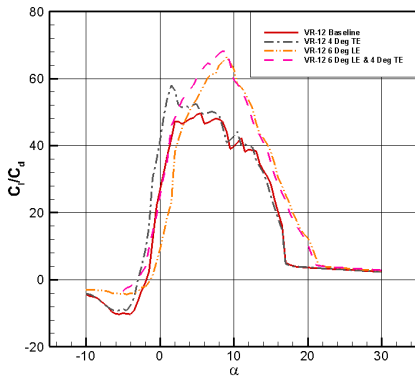
(c) Lift coefficient vs drag coefficient
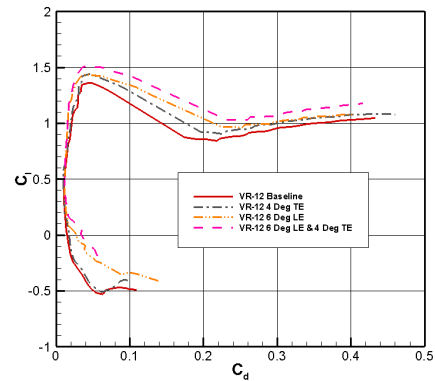
(d) Lift/Drag variations

Fig. 8. Effects of combined TE & LE deflections on VR-12 aerodynamics: *(a) C_l vs α, (b) C_d vs α, (c) C_l/ C_d vs α, (d) C_l vs C_d*
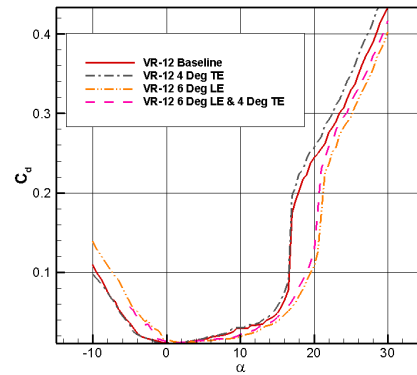
4. FLOW EXPERIMENTS[2]

Alongside the work of this paper, experimental testing was performed at NDSU to validate the CFD model. This work was led by Dr. Jordi Estevadeordal and William Refling. This group was tasked with the creation of a working morphing VR-12 airfoil as well as the advanced flow diagnostics.

Fig. 9. Blower wind tunnel at NDSU

The flow experimentation was performed in the advanced flow diagnostics lab in the blower wind tunnel that was developed at NDSU. Shown in figure 9. Capable of up to 60 m/s at turbulence levels of 0.5% to 2% in the test section. The test section itself is 12"x12"x36" and contains all necessary equipment to incorporate airfoil pitching and plunging.

---

[2] The material in this chapter was co-authored by Thomas Sprengeler and Dr. Y. Bora Suzen. Thomas utilized the CFD simulations to lead the experimental group in the tests that they performed. Also, Thomas generated all computational data used in the comparison between experimental and computational data.

Fig. 10. 2D PIV set up for blower wind tunnel

The types of diagnostics performed consisted of 2D PIV (figure 10), 3D tomographic

PIV, and surface PSP. The majority of the data was sampled at 100 images with some results

consisting of 1000 images to verify data. The PIV and PSP data was processed in house and used

for the validation of the various CFD models. Further detail is given in Refling22. (**Refling22**)

5. COMPUTATIONAL METHODS

This research utilized ANSYS-Fluent 18.2 for the further advancement of the simulations and analysis of the baseline VR-12 and its shape modified airfoils. The ANSYS-Fluent solver utilizes a Finite Volume Method that is closely based on elements with a Cell Vortex Formulation. ANSYS-Fluent incorporates seamlessly many different turbulence and transitional turbulence models that can be used to validate experimental results, as well as allow for the inclusion of moving and deforming domains utilizing well validated models and application in high performance parallel computing methods. (**ANSYS21**)

5.1. RANS Turbulence Modeling

All RANS simulations utilized the Shear Stress Transport (SST) k-ω two equation turbulence model as well as the $\gamma - Re_\theta$ transitional model for the final simulations used in the comparison between experimental and CFD data. (**Menter94; Menter06; Langtry06**) The SST model was chosen for its well documented and well accepted performance in detached flow, as well free shear, and wall bounded flow. The SST k-ω model does so well because of the ability to blend the complexity of the boundary layer near wall flow with the far field and free stream flow containing large eddies. This is achieved by blending k-ω and k-ε into the SST model. This model utilizes the k-ω equations for near wall boundary layer flow and the k-ε equations for far field free stream flow. The details of the SST model are given in Menter94. (**Menter94**)

Transitional modeling is very important as not all flow can be classified as either only laminar or only turbulent, there is often a transition from laminar to turbulent that introduces new aspects to the flow field. In order to capture the transition of flow from laminar to turbulent flow in the Fluent simulations the $\gamma - Re_\theta$ model was utilized. (**Langtry06**) This first term for γ coupled with the Shear Stress Transport turbulence model is used to determine if the local flow is

laminar or turbulent and if it should turn on downstream turbulence production at the point of transition.

5.2. Hybrid RANS/LES Turbulence Modeling

Later simulations advanced to incorporate hybrid RANS-LES models, specifically the Stress Blended Eddy Simulation (SBES). The hybrid model is advantageous for two reasons, it provides more accurate results, as the LES portion of the model is able to solve for more fine detail in the flow, while also maintaining lower computational cost by utilizing the RANS methods in regions that are traditionally more expensive for LES, i.e., the near wall regions. As its name suggests, this simulation blends together the RANS and LES methods of solving turbulence at the stress level. This can be visualized in equation 1.

$$\tau_{ij} = \tau_{ij}{}^{RANS} f_s + \tau_{ij}{}^{LES}(1 - f_s) \tag{1}$$

The term f_s is the shielding function or the blending function that controls how the RANS model and LES model are blended together to form this hybrid model. The primary goal of this model is to use RANS model near the wall, to reduce the computational cost since LES model near wall is much more computationally expensive. Then use LES model away from the wall where computationally LES is less expensive but far more capable of capturing fine detail in the flow. Equation 1 is used in order to blend the two different turbulence models together. Menter mentions five major complexities with developing a proper hybrid model, these are the ability to shield the RANS boundary layer, switch from RANS to LES reliably in separated shear layers, operate in wall modeled LES, allow for the use of all RANS and LES models, and be able to operate with lower quality meshes. (**Menter16**)

5.3. Computational Domain and Setup

5.3.1. Geometry and Boundary Conditions

The computational domain was modeled directly after the test domain of the wind tunnel with a 0.3048-meter-tall and a 0.9144-meter-long domain. The initial simulations were extruded to 1% of the chord length and the proceeding 3D simulations utilized a 1/3 thickness of the actual wind tunnel which was achieved by adding a symmetry boundary to both sides of the model. Below in figure 10 the dimensions of the domain can be seen as values non-dimensional in regard to the 0.1016 meter chord length. The domain is 3c tall, 9c long, with a 1.5c diameter inner domain. The boundary conditions were set to directly represent the conditions seen in the wind tunnel, a prescribed inlet velocity was used to match the Reynolds number being tested with an inlet turbulence intensity of 0.5% as recorded via hot wire data from previous testing of the wind tunnel, all wall boundaries were set as no-slip condition, and the outlet was prescribed a 0 relative pressure to represent the wind tunnel being open to the atmosphere, the two domains are joined via a fluid-fluid interface to allow for the seamless flow of fluid into and out of the two domains as seen below in figure 11.
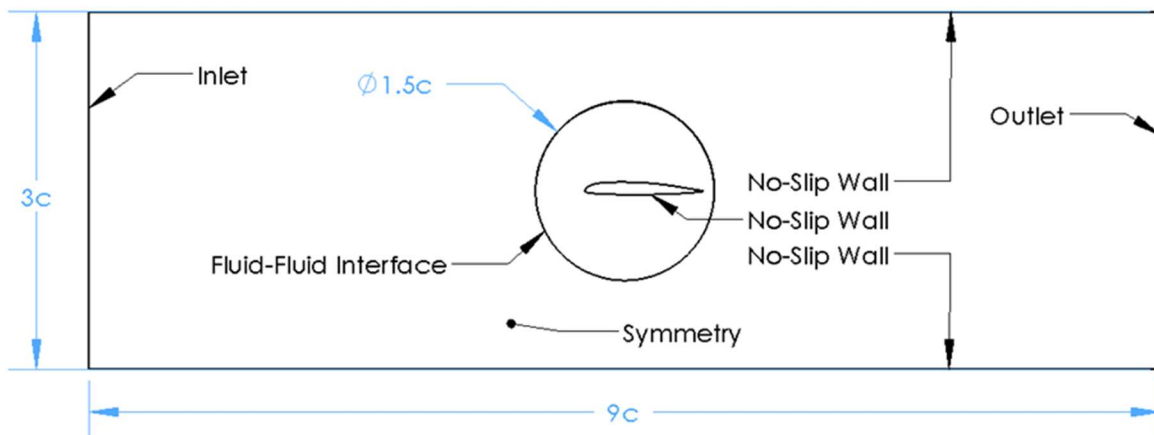

Fig. 11. Flow domain and boundary details

21

5.3.2. Mesh

The mesh utilized in the computations for this research were generated using ANSYS-ICEM. (**ANSYS21**) The final mesh for the initial 2D tests seen in figure 12a resulted in the use of 1,157,640 nodes, 1,279,760 elements, and a $y^+=1$ near the surface of the airfoil. This mesh utilized an inflation layer to increase the node density in regions of important flow and less nodes away from the important areas to reduce the computational cost. This final mesh was the result of a grid independence study to ensure an adequate mesh. This mesh remained entirely hexahedral with very low skewness as seen in figure 12c. This initial mesh also utilizes a two part domain, the first being the outer domain representing a majority of the wind tunnel and a second domain that is round that encompasses the airfoil. This round inner domain seen in figure 12b allows for the rotating of the airfoil to different angles of attack, while also allowing for the smooth transition to pitching simulations later on.
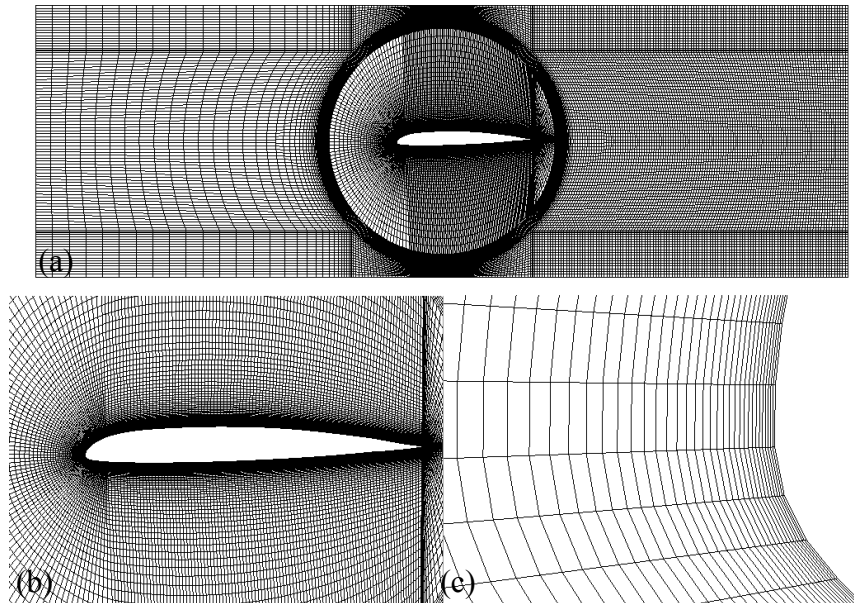

Fig. 12. Computational RANS/URANS Mesh (a) Entire mesh (b) Inner domain (c) Leading edge detail

After a series of 2D test where run using this set up, it was extruded 4 inches to represent the center 4 inches of the experimental airfoil that were used for testing. The z-direction mesh spacing was set to 4% of the chord or 0.04*C. This resulted in 26 nodes in the span wise direction for 3D RANS and URANS simulations.

5.3.3. Temporal Resolution

In order to accurately simulate the natural unsteadiness involved in these simulations a proper time step must be chosen. Equation 2 was used in order to accurately predict the time step for a specific grid. This equation considers how fast a particle flows through the domain in relation to the amount of grid cells in the freestream direction in order to predict the necessary time step. The results of this equation were $\Delta t = 7x10^{-4}\ s$ for the URANS grid.

$$\Delta t = \frac{\frac{L}{U_\infty}}{N * CFL} \tag{2}$$

5.3.4. Solver

These simulations were run using the ANSYS-Fluent solver set to the High-Resolution scheme which is a second order accurate solver. This scheme was utilized for all flow equations as well as the turbulence and transitional modeling equations. All simulations were set to achieve convergence at an RMS value of $1x10^{-6}$. The convergence criteria were achieved for all simulations.

5.3.5. Hardware

These simulations were run on NDSU Center for Computationally Assisted Science and Technology (CCAST) computing clusters. The cluster contained up to 10 available compute nodes, each node was able to provide up to 20 CPUS and 42 GB of rapid access memory (RAM). Depending on the complexity and mesh size of the simulation, runs requested 2-10 compute nodes.

5.3.6. Adjustments for SBES Model

The mesh used in the hybrid SBES method was an adaptation of the mesh used in the RANS/URANS simulations. The most notable change is the relaxation of mesh spacing in the regions of least interest in order to reduce the computational cost required to generate/solve the grid, seen below in figure 13. Local refinement was added to the downstream region of the airfoil to better capture the small scale structures as a result of flow interacting with the airfoil. Along with local refinement in the downstream region the mesh was also increase in the spanwise direction in order to get rid of any spanwise instabilities due to inadequate span wise meshing. This mesh also used a $y^+=1$ near the surface of the airfoil. The final mesh resulted in 10,463,625 million nodes and 10,252,744 million elements.
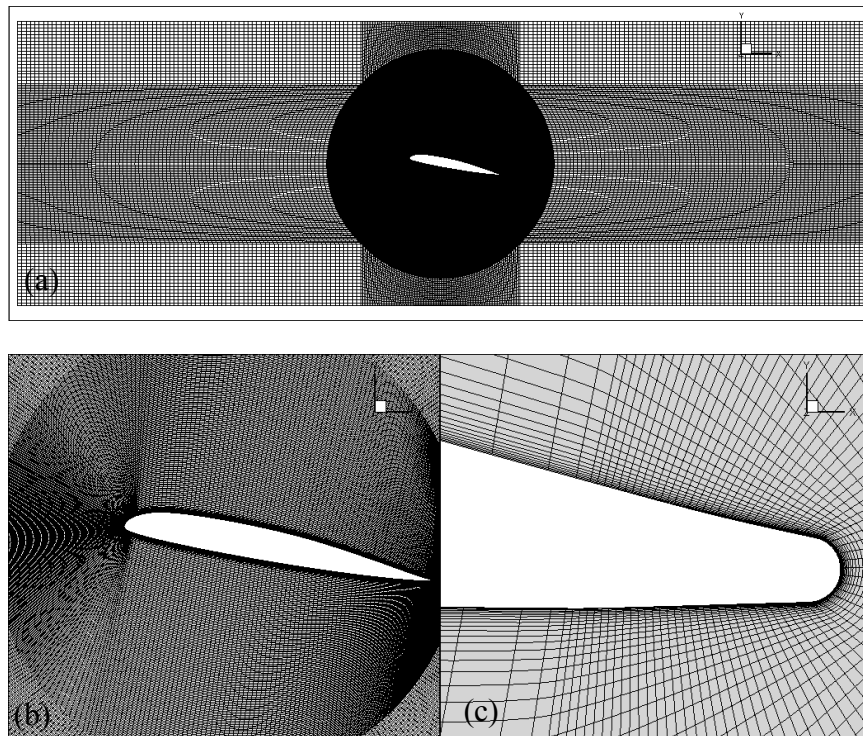

Fig. 13. Computational RANS/URANS Mesh (a) Entire mesh (b) Inner domain (c) Trailing edge detail

Another adjustment needed in order to properly run using the SBES model is to adjust the wall boundaries. The use of symmetry boundaries coupled with unresolved turbulence near

24

boundary results in unrealistic results. This was tested and when left as symmetries the side

boundaries performed as solid walls. In order to adjust the simulation to run properly using the

SBES method, the side boundaries needed to be changed to translational periodic boundaries.

Lastly in order to properly resolve the small scale flow structure the time step needs to be

adjusted to fit the finer mesh used for the SBES simulations. To do this equation 7 was used, this

resulted in a time step of $\Delta t = 7.5x10^{-5}\ s$ for the Hybrid SBES grid. (**Menter16**)

6. PITCHING & MORPHING AIRFOIL

6.1. Pitching Airfoil

The pitching motion is induced to represent a rotorcraft blade rapidly changing angle of attack as it rotates around the azimuth constantly adjusting for the new flow field that it is going to encounter. To do so, a rotating interface was added between the outer square domain and the inner circular domain with equation 3 used to induce a pitching motion.

$$\alpha = \theta_{PO} + A_P \cos(2\pi f_P t + \varphi_P) \tag{3}$$

The term φ is used to adjust where the airfoil starts its pitching motion, for instance to start at negative 2° and pitch up a value of $\varphi = \pi$ is used to offset the sinusoidal motion so that the airfoil can begin its pitching at negative 2° and advance into an upward pitching motion.

The domain used is the same as the previous simulations, the only change to the domain set up is the chord length, the new simulation utilizes a 6 inch chord length. This chord length change was done in order to make assembly of the experimental airfoil easier. This resulted in a reduction of the inlet velocity to 25 m/s in order to meet the required Reynolds number of 250,000.

$$K_r = \frac{\pi f c}{U_\infty} \tag{4}$$

In order to pitch the airfoil at a proper frequency a reduced frequency value is used. This reduced frequency value shown in equation 4 is a way to nondimensionalize the frequency of pitching the smaller chord airfoil used in experimentation to that of the full size rotor blade.

6.2. Shape Morphing Airfoil

The next stage of simulations involves the dynamic morphing of the leading and trailing edges of the VR-12 airfoil. These morphing simulations are going to mimic the types of deflection seen in the previous simulations but to incorporate a time dependent aspect to show

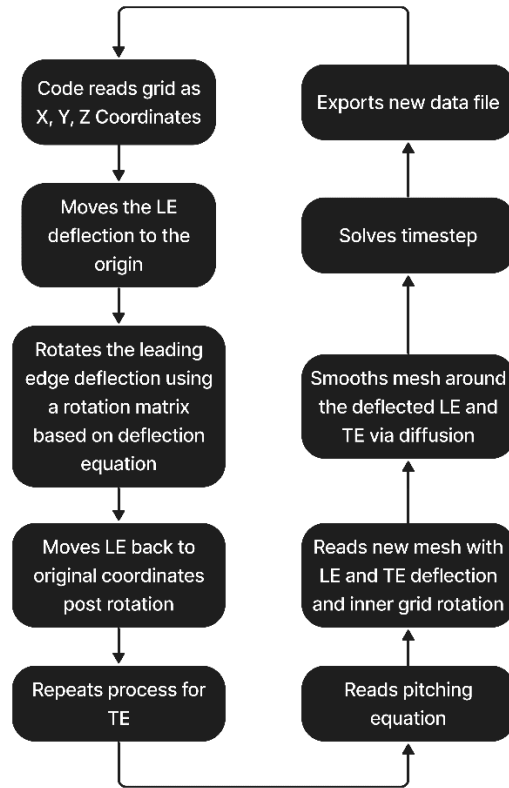how the flapping of the leading and trailing edges dynamically affect the aerodynamic characteristics.

Fig. 14. Flow chart of UDF morphing and pitching process

These simulations were performed using ANSYS Fluent because of the re-meshing and smoothing capabilities built into the flow solver. In order to have control of the airfoil shape during the simulation a user defined function (UDF) was utilized that allows for the control of the upper and lower airfoil surface, the process of the UDF morphing procedure can be seen above in figure 14. This code reads the nodes of the grid along the upper and lower surface as coordinates and applies a rotation matrix to rotate the leading and trailing edge about a set point. The motion is induced by a time dependent equation for theta and can be adjusted to match many

different types of motion. Initial tests were conducted using equations 5 and 6 respectively for

the sinusoidal motion of the leading and trailing edges.

$$\theta_{LE} = \theta_{LEo} + A_{LE} \cos(2\pi f_{LE} t + \varphi_{LE}) \tag{5}$$

$$\theta_{TE} = \theta_{TEo} + A_{TE} \cos(2\pi f_{TE} t + \varphi_{TE}) \tag{6}$$

The term φ is a term introduced to add a phase offset to set the starting deflection angle

to 0°. (**Alam09**)

In order to smooth and re-mesh the dynamically changing airfoil properly the diffusion

setting was chosen for the smoothing method. The diffusion method moves nodes at the surface

of the airfoil in response to the movement of the boundary, this method is best for simulating

small movements like the rotation of and airfoil surface. The diffusion parameter was set to 1.5

which helps preserve the mesh in the boundary layer region and moves the deformed mesh

further away from the surface. (**Abdessemed18**) Similar to previous meshes used, initial

morphing meshes utilized a completely quadrilateral mesh with a $y^+ = 1$ near the surface of the

airfoil to ensure all boundary layer flow is captured. Initial simulations are being computed in

2D. The 3D method of morphing performs in a very similar matter with adjustments to some

dynamic mesh settings.

Initial testing has produced results valuable in validating the shape of the morphing

airfoil produced using the UDF against the actual VR-12 coordinates. In figure 15 below the

baseline and combination VR-12 shapes are plotted to show a comparison between the actual

coordinates and those calculated with the UDF. The UDF results show a faithful shape when

compared to the actual coordinates. This agreement certifies that the UDF will morph the airfoil

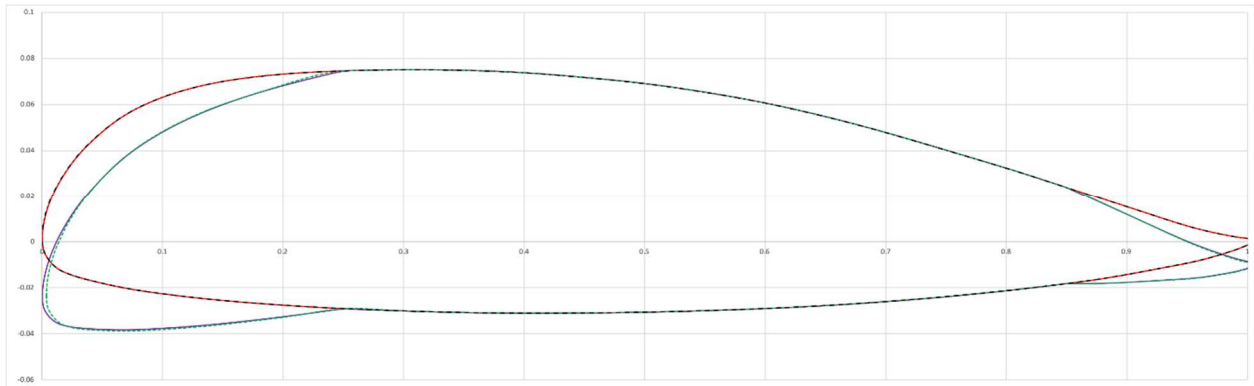while keeping the surfaces true to the original design.

Fig. 15. Showing the non-dimensional X/c vs Y/c baseline VR-12 (red) and the LE 6° and TE 4° combination (green)

7. RESULTS AND DISCUSSION

7.1. 2D &3D RANS Results

Initial comparisons between Fluent and XFLR5 data will be used to validate the data used in the initial shape selection process. Then data from 2D and 3D RANS will be compared with experimental PIV data to show vorticity magnitude contours. These comparisons consist of the baseline VR-12 and the three modified airfoils at a Re=250,000 and angles of attack of 0, 5, and 10°. Initial 3D simulations were computed using the SST k-ω turbulence model with the $\gamma - Re_\theta$ transitional model.

Initial comparisons between CFX and the experimental data were showing discrepancies in the amount of separation and the location in which separation was occurring. This is where the k-ω model was able to aid in the reproduction of the flow scenario seen in the wind tunnel. The k and ω quantities can be controlled at the inlet of the domain and since k was calculated based on the known turbulence intensity in the wind tunnel such that k=0.0326 $\frac{m^2}{s^2}$, ω was adjusted in order to control the specific dissipation of turbulence so that the correct amount of turbulent kinetic energy level was observed near the airfoil as compared to the experiments. The turbulence kinetic energy calculations were done using equations 7, 8, and 9.

$$k = \frac{1}{2}(\overline{u'u'} + \overline{v'v'} + \overline{w'w'}) \tag{7}$$

Assuming isotropic turbulence, k reduces to:

$$k = \frac{1}{2}(3\,\overline{u'u'}) = \frac{3}{2}(\overline{u'u'}) \tag{8}$$

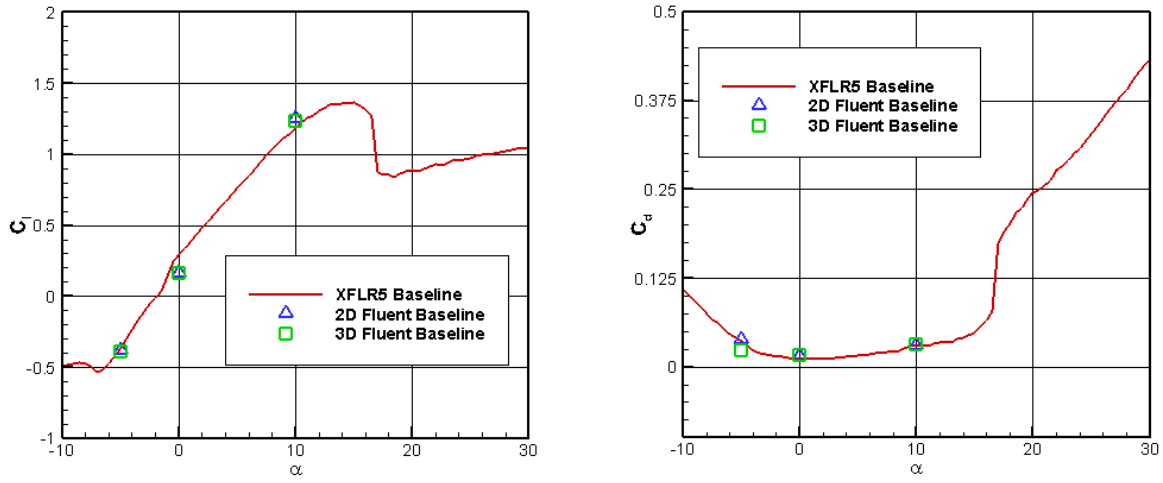The freestream turbulence intensity (FSTI) is defined in terms of k as:

$$FSTI = \sqrt{\frac{\overline{u'u'}}{U_\infty^2}} * 100 = \sqrt{\frac{\frac{2}{3}k}{U_\infty^2}} * 100 \tag{9}$$

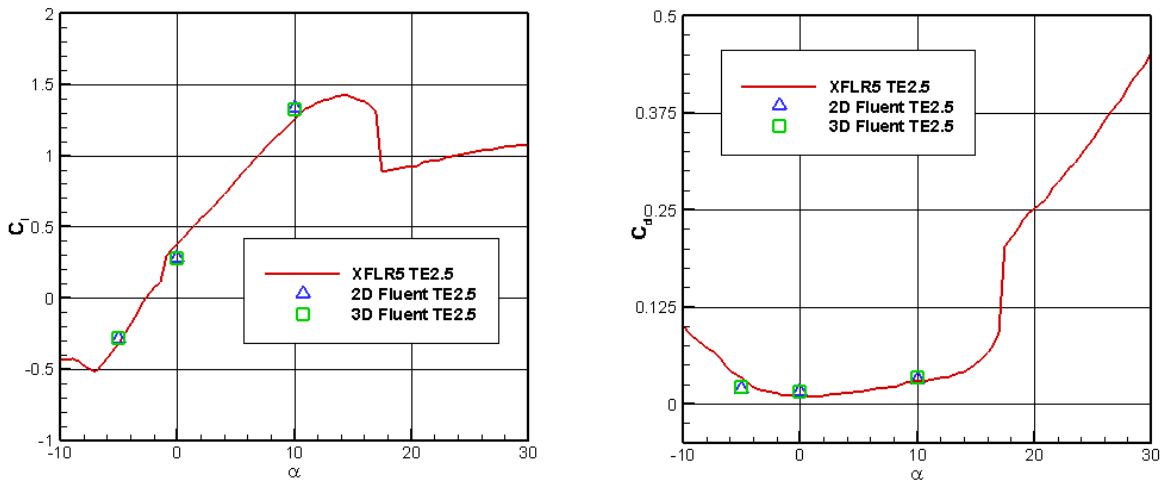The turbulent length scale can be calculated using equation 10.

$$l = \frac{\sqrt{k}}{\omega} \tag{10}$$

This quantity is important because in order to match the decay of turbulence as observed in the experiments. The ω is adjusted until the simulation results more closely match the decay seen in the experimental results. After many adjustments of ω the final value showing the best agreement between experimental and CFX results was $\omega = 8450\frac{1}{s}$ for the specific computational domain and inlet turbulence intensity.

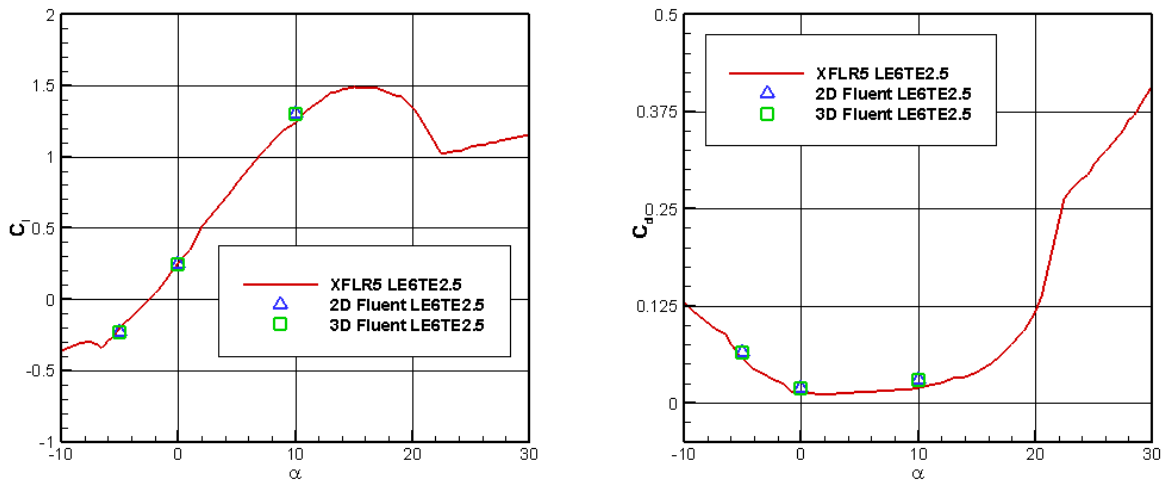7.1.1. Coefficient of Lift and Drag

(a) Baseline VR-12

(b) Trailing edge deflected 2.5°

Fig. 16. Comparing effects of LE and TE deflections on coefficients of lift (left) and drag (right) for ANSYS Fluent vs XFLR5: (a) Baseline VR-12 (b) Trailing edge deflected 2.5° (c) Leading edge deflected 6° (d) Trailing edge deflected 2.5° + Leading edge deflected 2.5°
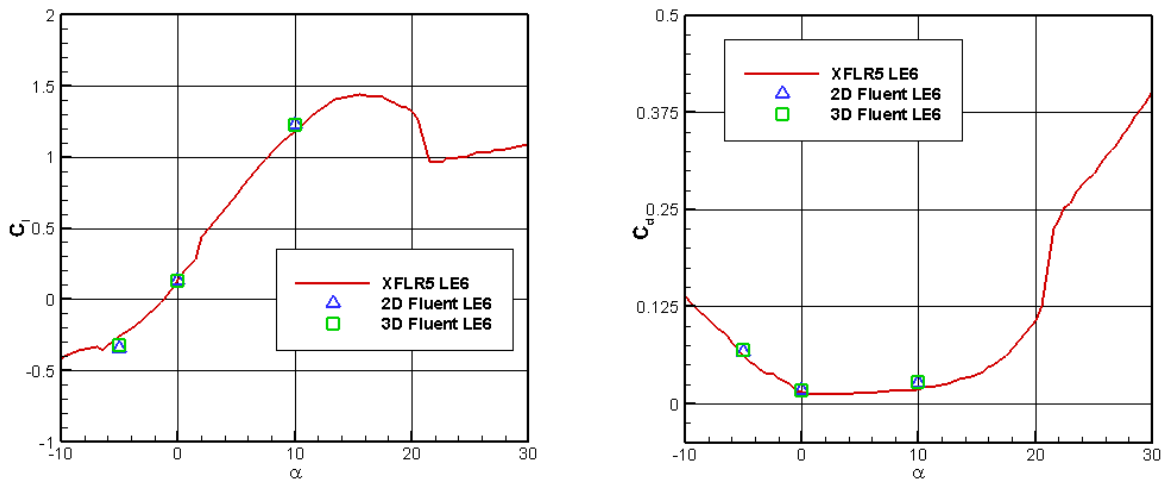
(c) Leading edge deflected 6°

(d) Trailing edge deflected 2.5° + Leading edge deflected 2.5°

Fig. 16. Comparing effects of LE and TE deflections on coefficients of lift (left) and drag (right) for ANSYS Fluent vs XFLR5: (a) Baseline VR-12 (b) Trailing edge deflected 2.5° (c) Leading edge deflected 6° (d) Trailing edge deflected 2.5° + Leading edge deflected 2.5° (continued)

In figure 16 the comparison of the coefficients of lift and drag is made between 2D RANS, 3D RANS, and XFLR5 data. This comparison between the three models is made to verify that the increase in aerodynamic performance seen in initial XFLR5 results will also be seen in the more accurate RANS calculations. When looking at the baseline airfoil in plot 16a,

the lift values from the RANS calculations show an error of less than 5% when compared to the XFLR5 data. When looking at the drag values on the right, the 0° and 10° cases again show that same less than 5% error value between RANS and XFLR5 models, the -5° case shows a slightly higher error value of 9% when comparing the 3D RANS to the XFLR5 model. The rest of the cases for figure 16b, 16c, and 16d all show error values less than 5% when comparing RANS to XFLR5 results.

Figure 14 also shows the increase in coefficient of lift and reduction in drag of the new modified airfoil shapes. When looking at figures 14a and 14c, the leading edge deflection of 6° greatly increases the stall angle of attack, from 16° to nearly 22° angle of attack. The leading edge deflection also greatly reduces the drag produced at higher angles of attack. Figure 14a and 14b show a slightly less noticeable improvement of lift, most notable looking at the zero angle of attack coefficient of lift there is an increase of lift and reduction of drag overall at lower angles of attack when utilizing the trailing edge deflection airfoil. Further static testing at median angles of attack would need to be testing to see the full effect of the combination airfoil at the median angles of attack where it was designed to perform the best.

7.1.2. Velocity Magnitude

The following results show comparison between experimental results (left) to 2D RANS (middle) and 3D RANS (right). This comparison is used to verify that a similar flow field is seen in both experimental and computational results.

The experimental data is a composite of three separate images, the first image from -0.2 to 0.2 x/c, the middle image from 0 to 0.85 x/c, and the last image is from 0.85 to 1.2 x/c. There are dashed lines on the CFD data that correspond to the start and end of the middle image that

represents the majority of the body of the airfoil. Fore and aft of the dashed lines represent the close up of the leading edge and trailing edge respectively.

Looking at figure 17 first for the baseline VR-12 shape, figure 17a at -5° AoA shows good agreement between the three cases with very similar streamline and velocity patterns with no visible flow circulation. Figure 17b at 0° AoA also shows very similar results across all three cases. Figure 17c at 10° AoA starts to show region of separation near the TE for the RANS cases, this is not seen in the experimental results. The experimental case shows a smaller low velocity region near the trailing edge which would also be the reason that there is no circulation seen in the streamlines for the experimental case.
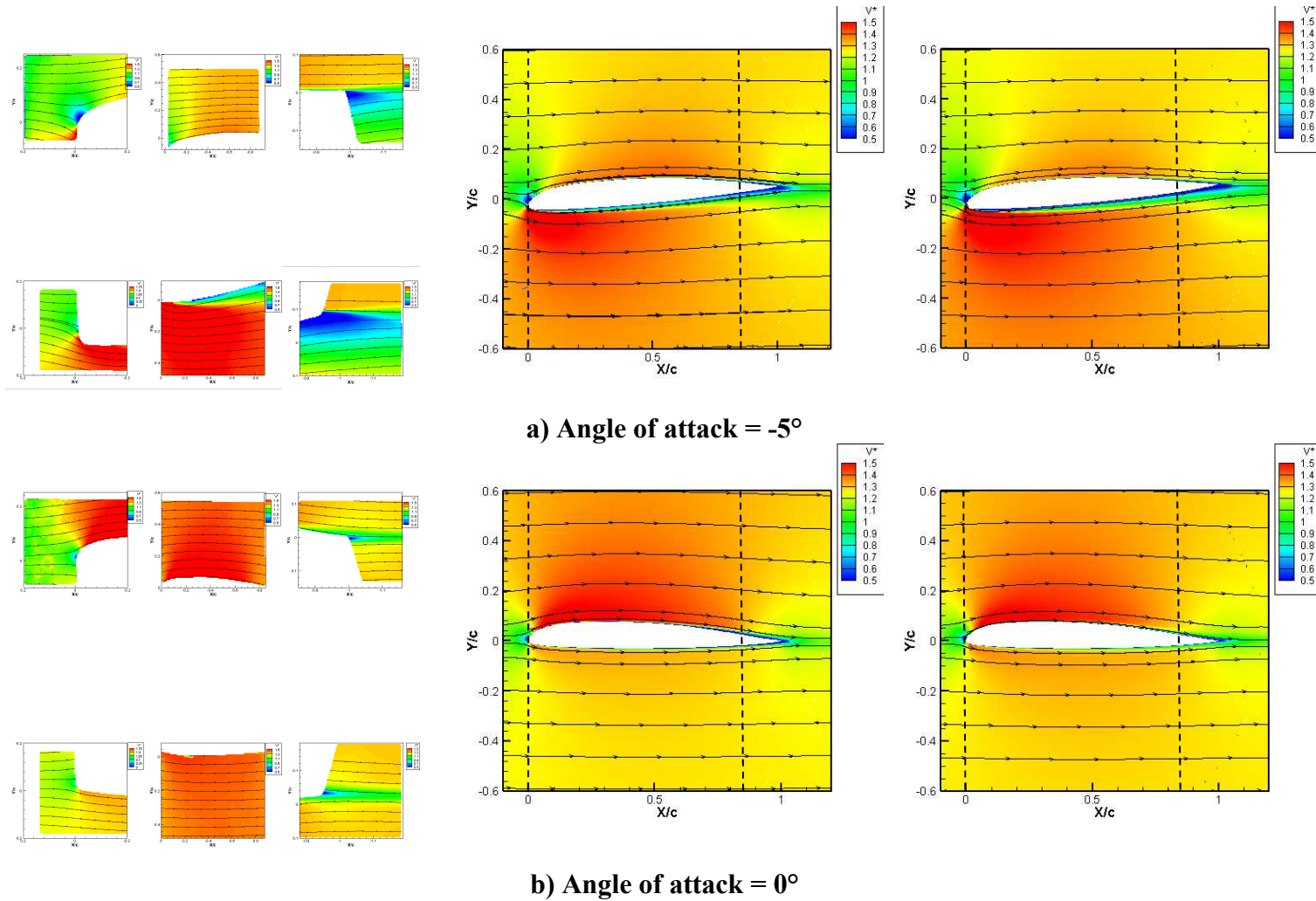
a) Angle of attack = -5°

b) Angle of attack = 0°

Fig. 17. Comparison of experimental (left) 2D Computed (middle), and 3D computed (right) velocity contours and streamlines for Baseline VR-12 at Re=200,000: (a) α=-5° (b) α=0° (c) α=10°
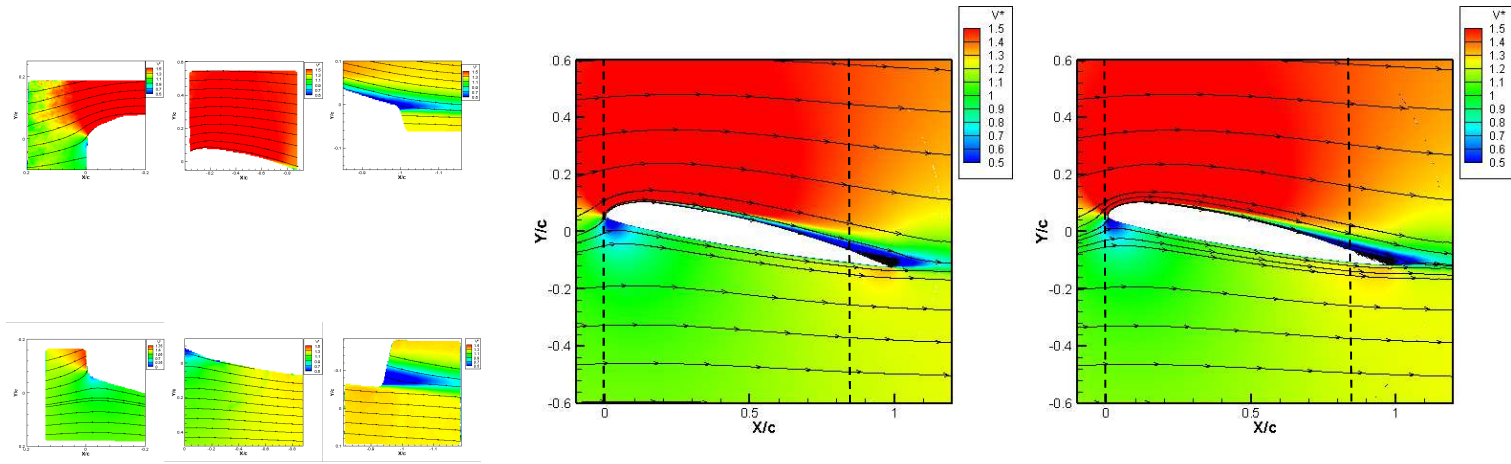
c) Angle of attack = 10°

Fig. 17. Comparison of experimental (left) 2D computed (middle), and 3D computed (right) velocity contours and streamlines for Baseline VR-12 at Re=200,000: (a) α=-5º (b) α=0º (c) α=10º (continued)

Figure 18 shows the comparisons for the TE 2.5° case. When looking at figure 18a at -5° AoA, it can be seen that the TE deflection creates a smaller low velocity region along the bottom surface of the airfoil when compared to the baseline case. Similar results can also be seen in the 0° AoA case in figure 18b. The trailing edge deflection shows clear improvements at lower angles of attack when compared to the baseline VR-12 airfoil. Figure 18c shows the trailing edge deflection at 10° AoA, this case does not show any improvement when compared to the baseline case, as the cases are almost identical.

These results show that at the lower angles of attack of 0° and -5° that the trailing edge deflection is creating a reduction in the amount of low velocity region near the trailing edge. This low velocity region leads to an increase in drag. Being able to reduce the size of this region and reduce the separated flow will increase the performance of the airfoil. It is also shown that at the lower angles of attack the trailing edge airfoil is creating a large pressure differential over the airfoil than compared to the baseline airfoil.

a) Angle of attack = -5°
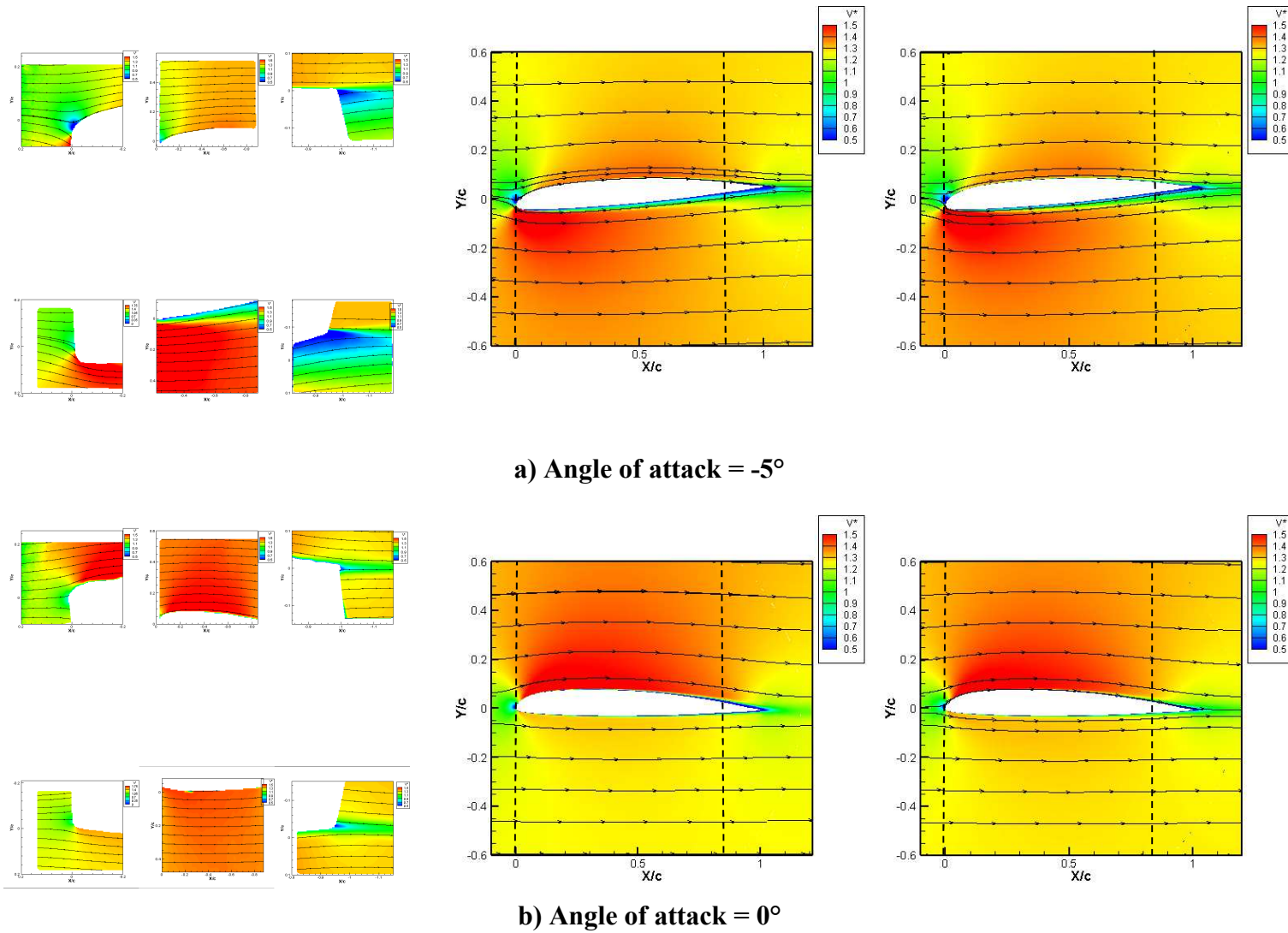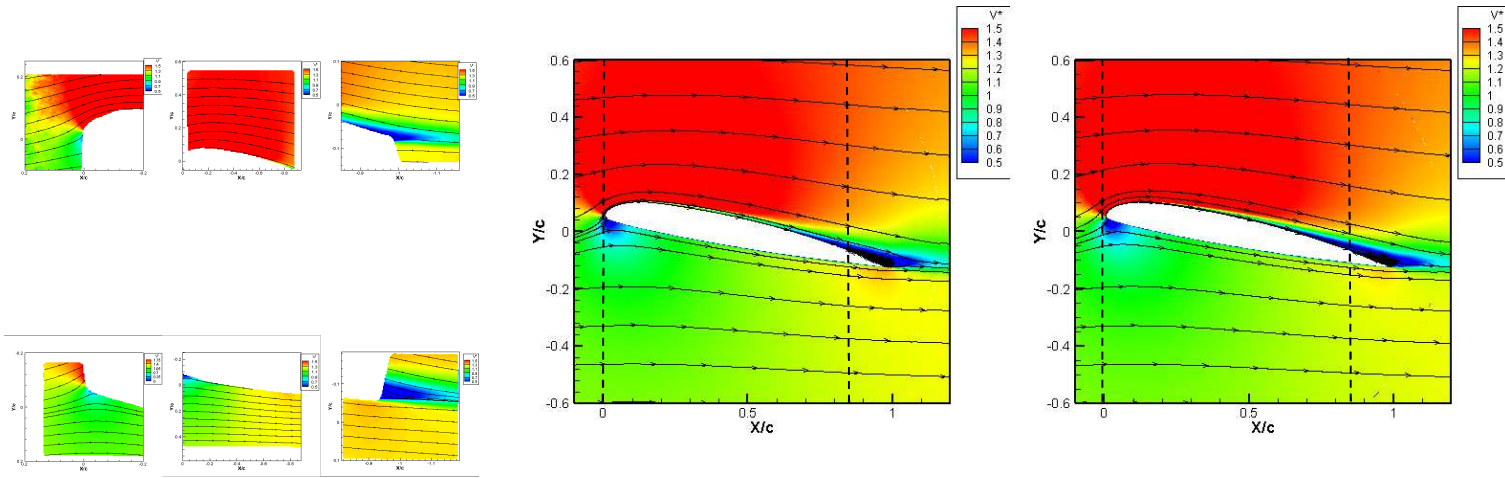

b) Angle of attack = 0°

Fig. 18. Comparison of experimental (left), 2D computed (middle), and 3D computed (right) velocity contours and streamlines for VR-12 with TE 2.5° deflection at Re=200,000: (a) α=-5º (b) α=0º (c) α=10º

c) Angle of attack = 10°

Fig. 18. Comparison of experimental (left), 2D computed (middle), and 3D computed (right) velocity contours and streamlines for VR-12 with TE 2.5° deflection at Re=200,000: (a) α=-5o (b) α=0o (c) α=10o (continued)

In figure 19 the leading edge deflection of 6° is analyzed, initially at -5° AoA in figure 19a it is clear that the leading edge deflection is causing a large separation bubble near the leading edge of the bottom surface of the airfoil. This is going to result in a decrease in the lift and increase in drag at lower angles of attack. Next, in figure 19b at 0° AoA the leading edge deflection is causing a region of high velocity or low pressure along the leading edge of the bottom surface, this is causing a reduction of lift further decreasing the performance of the airfoil at this location. Looking at figure 19c at 10° AoA, the leading edge greatly reduced the separation region that was seen near the trailing edge in the baseline VR-12 case. These results again fall in line with what was expected after the initial results from XFLR5.

The leading edge deflection shows that it is very well designed for higher angle of attack flow, it can be seen that at low angles of attack the deflection is creating unwanted separated flow and increased drag. Whereas at higher angles of attack the deflected airfoil ultimately helps to decrease the angle of incidence where the flow reaches the leading edge of the airfoil, resulting in the flow staying attached over more of the airfoil and greatly reducing the low velocity region near the trailing edge. This shows that this leading edge deflected airfoil is much more suited for higher angles of attack.
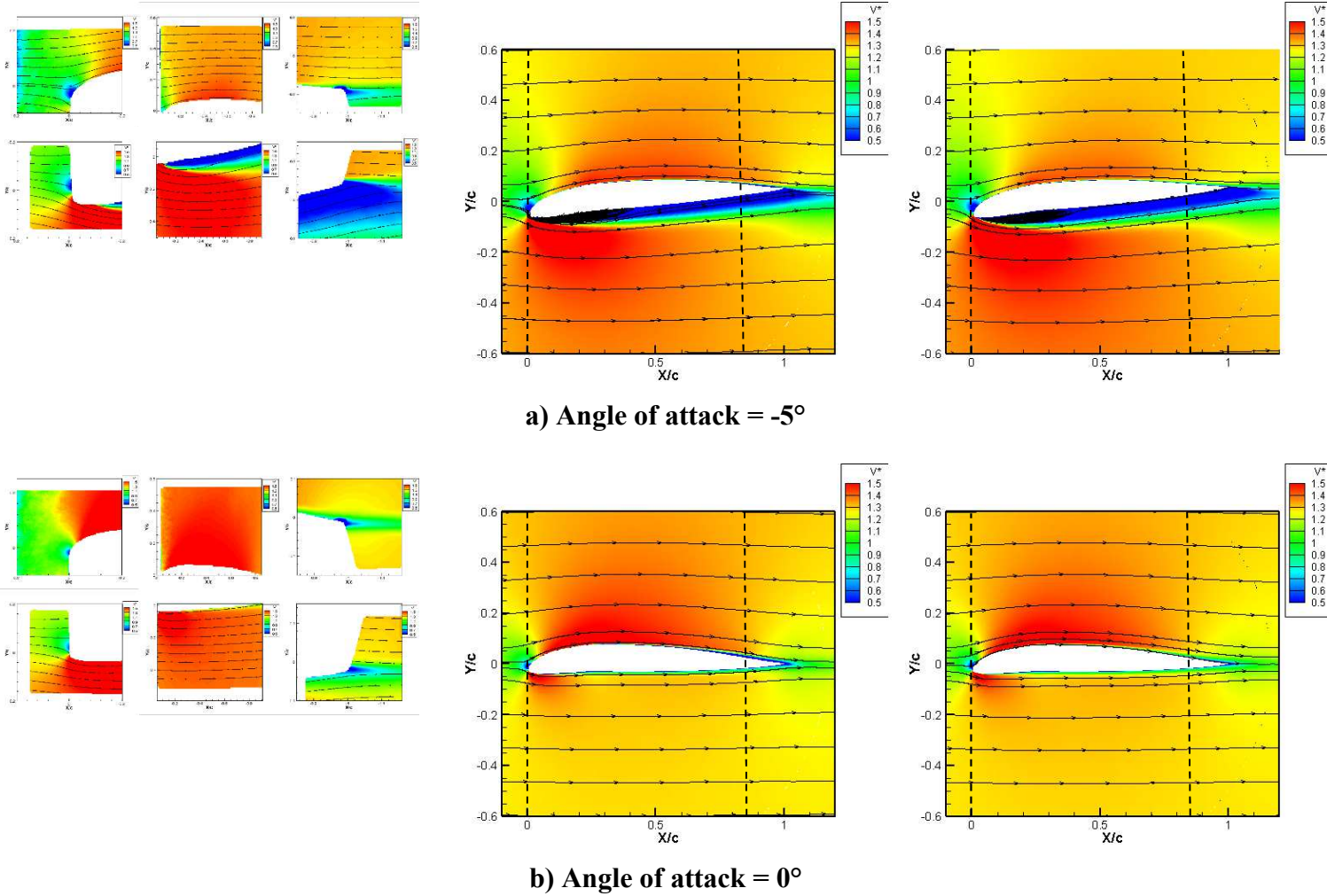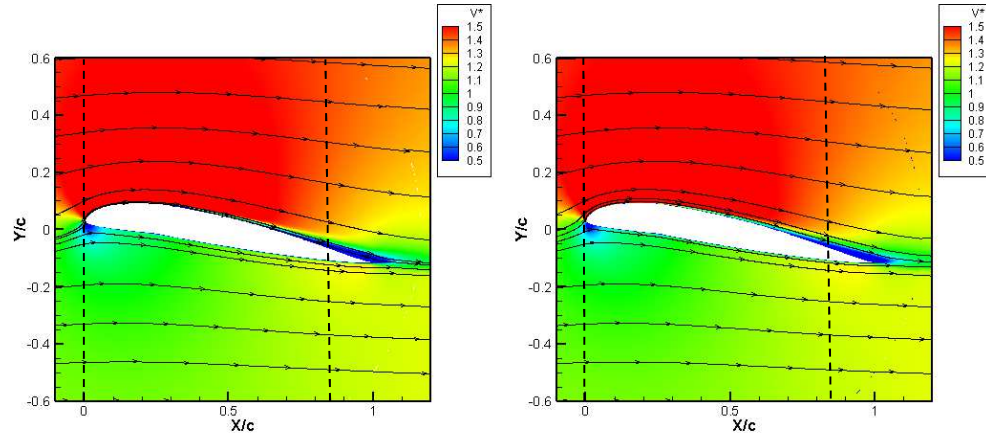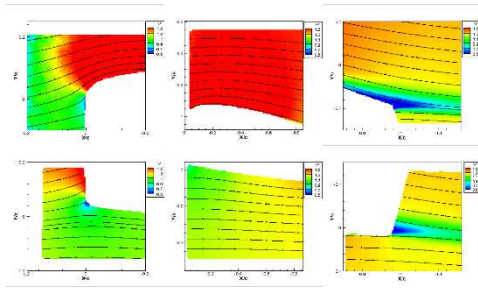
a) Angle of attack = -5°

b) Angle of attack = 0°

Fig. 19. Comparison of experimental (left), 2D computed (middle), and 3D computed (right) velocity contours and streamlines for VR-12 with LE 6° deflection at Re=200,000: (a) α=-5º (b) α=0º (c) α=10º

c) Angle of attack = 10°

Fig. 19. Comparison of experimental (left), 2D computed (middle), and 3D computed (right) velocity contours and streamlines for VR-12 with LE 6° deflection at Re=200,000: (a) α=-5º (b) α=0º (c) α=10º (continued)

Figure 20 represents the data comparisons for the leading and trailing edge combination case. Figure 20a shows very large separation near the leading edge when compared to the baseline VR-12, this can be attributed to the leading edge deflection in combination with the negative angle of attack. Figure 20b at 0° AoA shows an undesired low pressure region near the leading edge of the bottom surface, this is going to cause decreased lift and overall reduced performance. Figure 20c at 10° AoA shows improvement over the baseline and trailing edge deflected airfoil with the leading edge helping to maintain flow attachment over the entire airfoil. While it is unclear from this data the performance difference between the LE6 and the combination airfoil, later analysis will show that the LE6 is better at higher angles of attack while the combination case excels at intermediate angles.

The combination airfoil doesn't have as clear of an advantage in the static testing as it will later on in the unsteady pitching results. Though, it can be noted that while not as optimal at 10° as the leading edge airfoil it does provide less separation than the baseline airfoil. If more static tests were performed at median angles of attack the benefit of the combination airfoil would be more prominent.

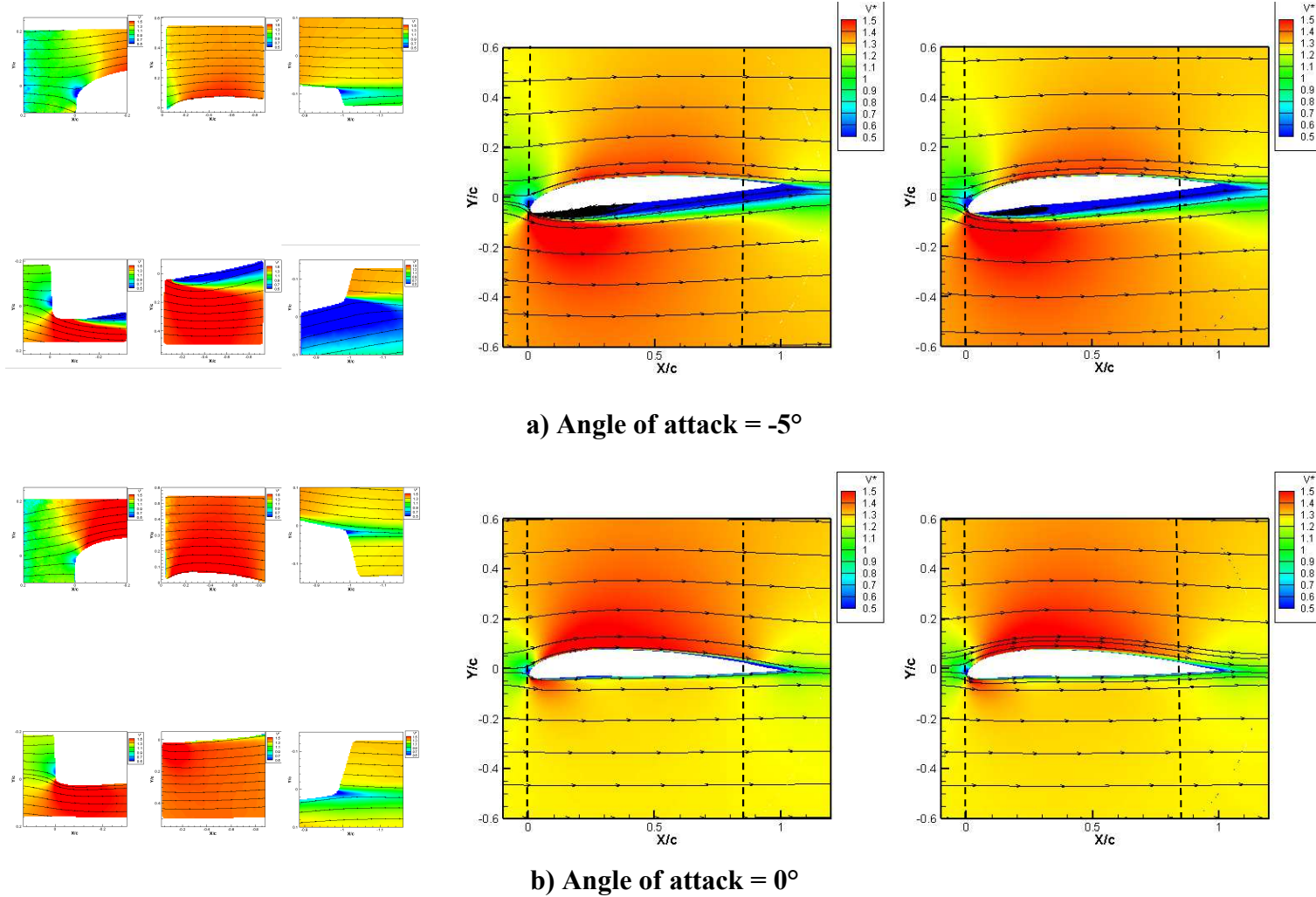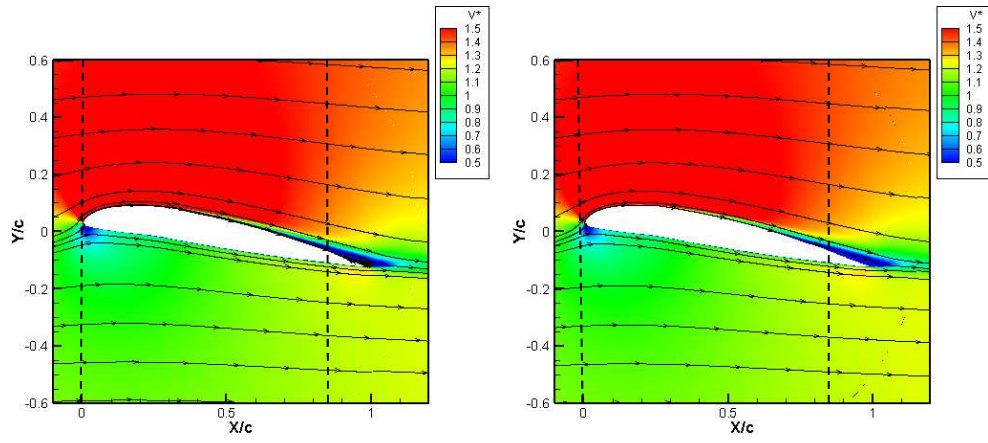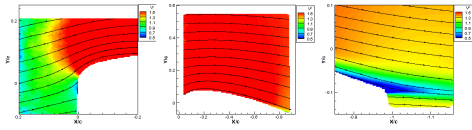**a) Angle of attack = -5°**

b) Angle of attack = 0°

Fig. 20. Comparison of experimental (left), 2D computed (middle), and 3D computed (right) velocity contours and streamlines for VR-12 with 6° LE & 2.5° TE combined deflection at Re=200,000: (a) α=-5º **(b)** α=0º **(c)** α=10º

c) Angle of attack = 10°

Fig. 20. Comparison of experimental (left), 2D computed (middle), and 3D computed (right) velocity contours and streamlines for VR-12 with 6° LE & 2.5° TE combined deflection at Re=200,000: (a) *α*=-5º (b) *α*=0º (c) *α*=10º (continued)

7.1.3. Coefficient of Pressure 2D & 3D RANS

Figure 21 shows the comparison of coefficient of pressure for all three angles of attack as well as the four different airfoil shapes for 2D and 3D RANS simulations. Figure 21a shows the comparison for the baseline VR-12 with a minor under prediction in pressure for the 2D case at -5°. At 0° the 2D and 3D model show a perfect match. At 10° the 2D shows a minor under prediction near the leading edge and a slight over prediction near the trailing edge. Figure 21b TE2.5, shows near perfect results for both the -5 and 0° cases with a small under prediction in the 2D model near the leading edge and small over prediction near the trailing edge. For figures 21c and 21d, LE6 and LE6TE2.5 respectively, there is a near perfect match for all three angles of attack for both cases, with only a minor discrepancy near the leading edge of the 10° LE6TE2.5 case.

Overall, the pressure distribution of the VR-12 airfoil increases as angle of attack increases. This results in an increase in lift as the angle of attack is increased. It is also important to note that there is not a large discernable increase in pressure distribution when comparing the cases to each other, for instance the leading edge 6 degree airfoil out performs the base line airfoil yet when looking at figure 21a and 21c the baseline airfoil has a larger pressure differential, which means that it is creating more lift yet it is outperforming the baseline airfoil in coefficient of lift over drag because that leading edge deflection greatly reduces the amount of separation over the airfoil which results in a large reduction in drag. This reduction in drag is the key to the better performance of the leading edge deflection. Inversely for the trailing edge, the trailing edge shows better performance at lower angles of attack, this is due to an increase in pressure differential seen when comparing figure 21a and 21b, as well as showing a reduction in flow separation at lower angles of attack. These both culminate in the increase performance.
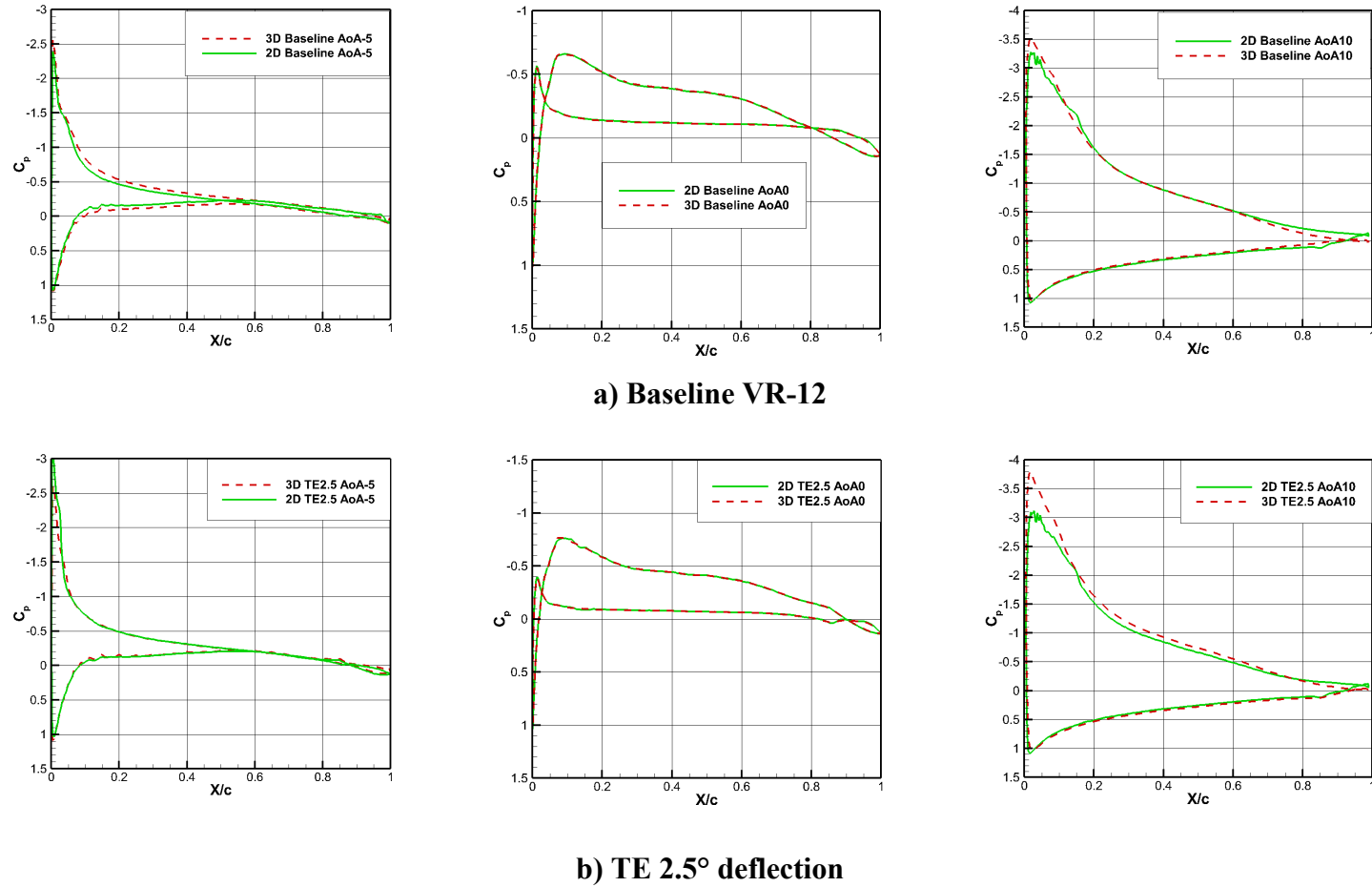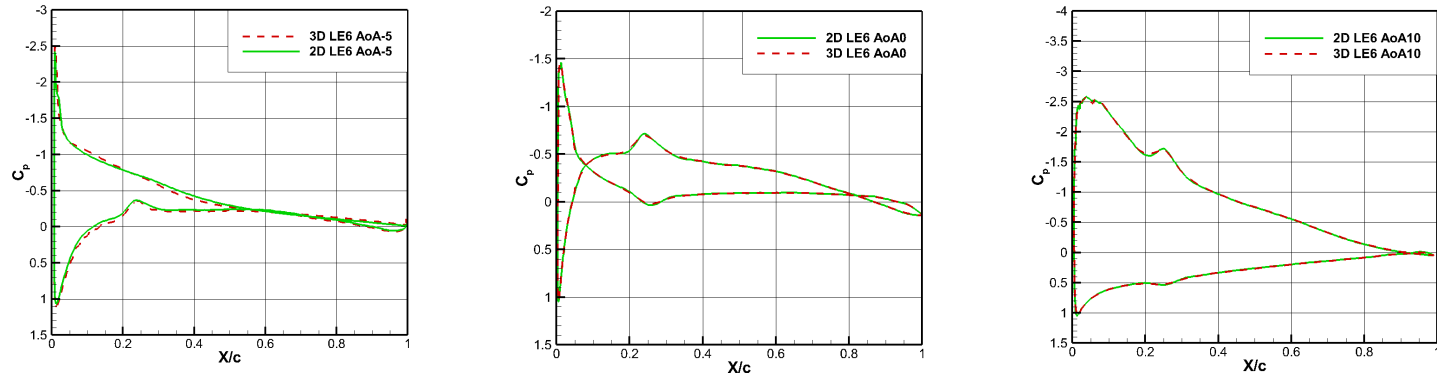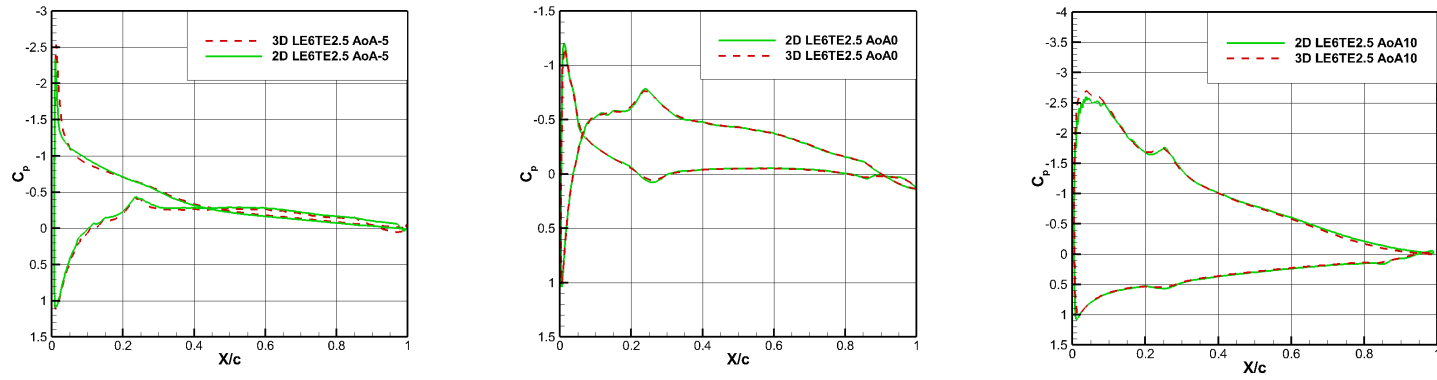
47

a) Baseline VR-12

b) TE 2.5° deflection

Fig. 21. Computed coefficient of pressure at Re=250,000, *α*=-5º (left), *α*=0º (middle), *α*=10º (right): (a) *Baseline VR-12* (b) *TE2.5°* (c) *LE6°* (d) *LE6TE2.5°*

c) LE6 6° deflection

d) LE6TE2.5° deflection

Fig. 21. Computed coefficient of pressure at Re=250,000, *α*=-5º (left), *α*=0º (middle), *α*=10º (right): (a) *Baseline VR-12* (b) *TE2.5°* (c) *LE6°* (d) *LE6TE2.5°* (continued)

7.1.4. Coefficient of Skin Friction

Figure 22 shows the comparisons for coefficient of skin friction at all angles of attack for all four airfoil shapes starting with the baseline VR-12 in figure 22a. At 0° AoA the baseline airfoil shows separation from 0c to roughly 0.075c on the lower surface and from 0.85c to 1c on the upper surface. At -5° AoA the baseline VR-12 shows no separation. At 10° AoA the baseline airfoil shows separation from 0.1c to 0.2c and 0.75c to 1c on the upper surface. Figure 22b shows that at -5° AoA the TE2.5 airfoil shows separation only from 0c to 0.05c which is less than what was seen for the baseline VR-12. At 0° AoA the TE2.5 airfoil shows no separation. At 10° AoA the TE2.5 airfoil shows separation from 0.1c to 0.15c and again at 0.75c to 1c along the upper surface, very similar to the baseline VR-12. Figure 22c shows that at -5° AoA the LE6 airfoil has separation from 0c to 0.5c along the bottom surface, which is a massive increase when compared to the baseline case. At 0° AoA there is a small region of separation from 0c to 0.05c on the bottom surface which is a minor increase over the baseline airfoil. At 10° AoA the LE6 airfoil shows only separation near the leading edge from 0c to 0.05c and near the trailing edge from 0.9c to 1c on the upper surface, this is a great improvement over the baseline VR-12 and TE2.5 airfoil. Lastly, in figure 22d for the combination of LE6TE2.5 airfoil all results are the same as in figure 22c except for the 10° AoA case the combination airfoil shows slightly more separation near the trailing edge starting at 0.85c until 1c.

The skin friction coefficient in the X direction is another key to the increase in performance of these new airfoil shapes. It shows that the morphed airfoils are creating less separation which directly correlates to less drag over the airfoil. The large reduction in separated flow is leading to the large reduction in drag and the better performance that is seen in the coefficient of lift over drag curves.
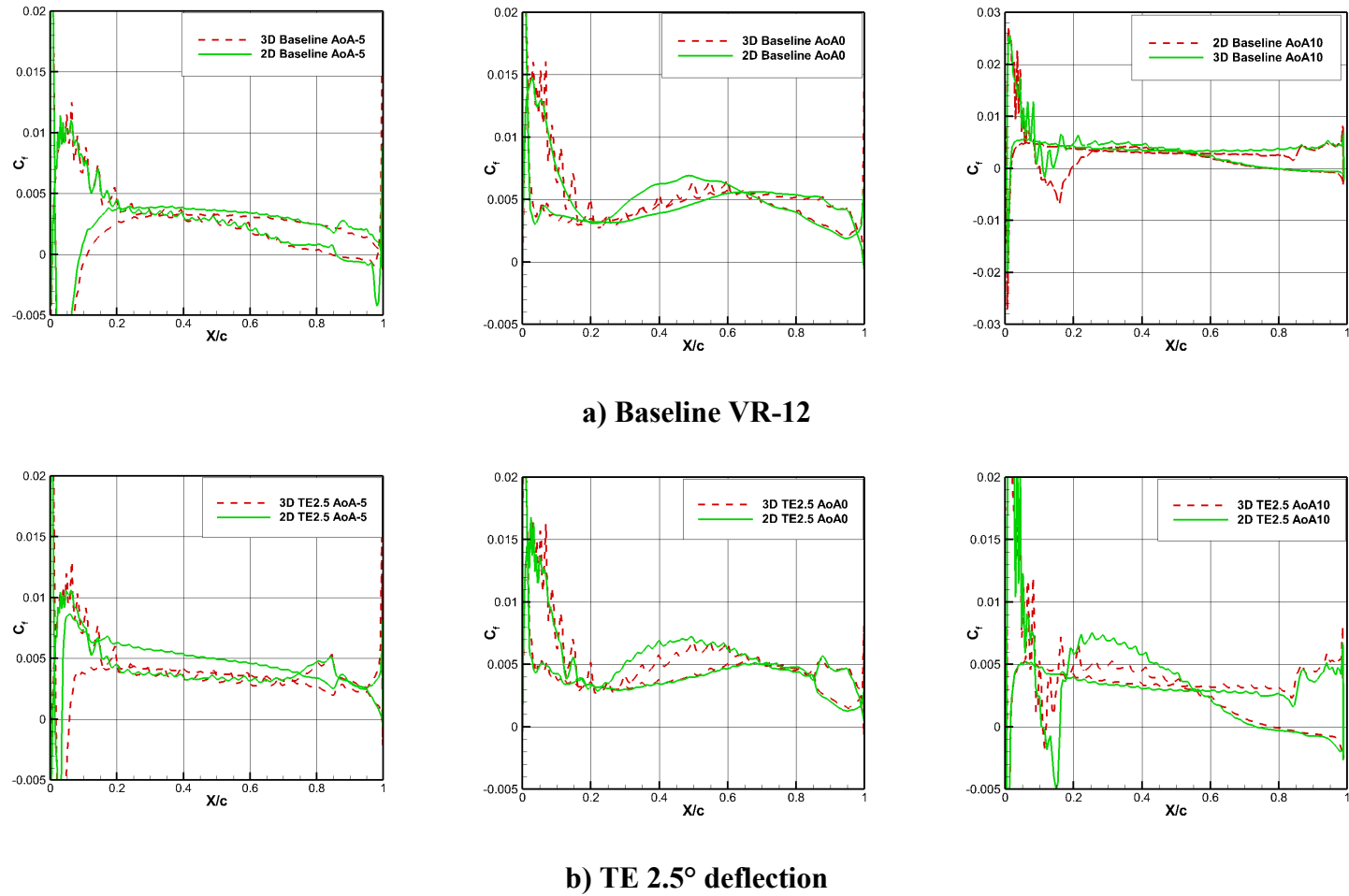
a) Baseline VR-12

b) TE 2.5° deflection

Fig. 22. Computed coefficient of skin friction at Re=250,000, α=-5º (left), *α*=0º (middle), *α*=10º (right): (a) *Baseline VR-12* (b) *TE2.5°* (c) *LE6°* (d) *LE6TE2.5°*
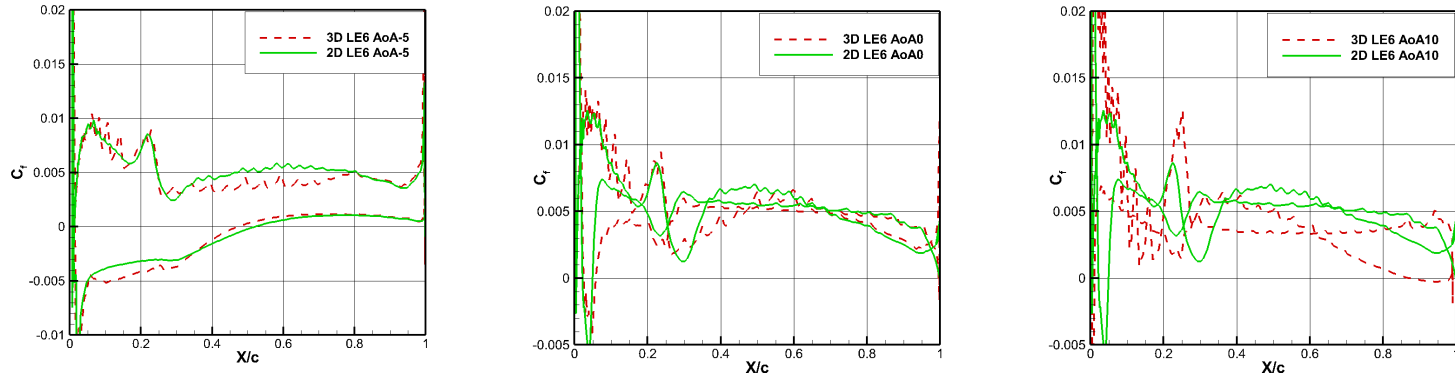
c) LE6 6° deflection
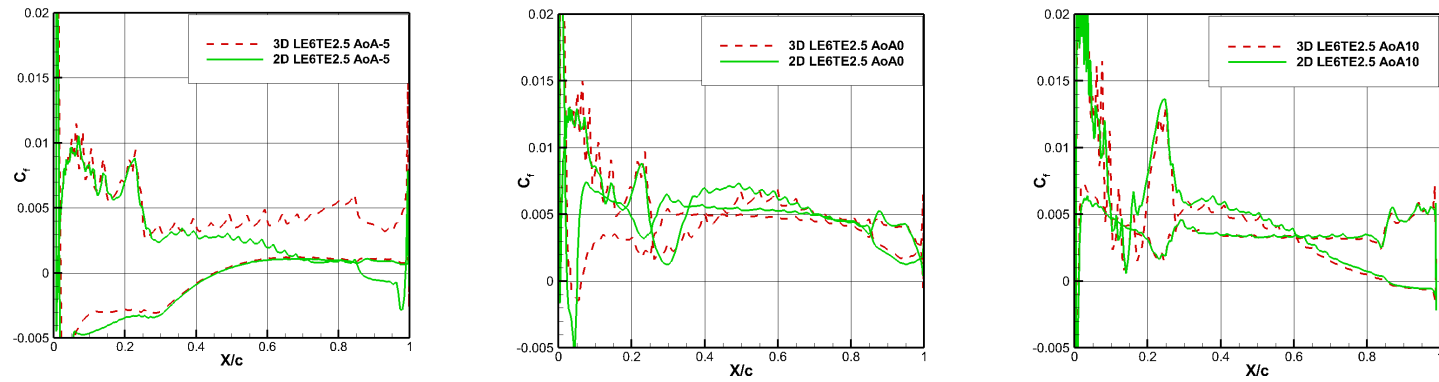
d) LE6TE2.5° deflection

Fig. 22. Computed coefficient of skin friction at Re=250,000, α=-5º (left), *α*=0º (middle), *α*=10º (right): (a) *Baseline VR-12* (b) *TE2.5°* (c) *LE6°* (d) *LE6TE2.5°* (continued)

7.2. 3D URANS Results

7.2.1. Pitching Static Morphed Airfoil

The first set of data for the pitching VR-12 airfoil includes data of the baseline VR-12 shape, the trailing edge deflection of 2.5°, the leading edge deflection of 6°, and a combination of the leading edge deflection of 6° and the trailing edge deflection of 2.5°. These tests were performed with static deflections to see how these different static airfoil deflections perform over an entire pitching regime.

The first set of tests were performed by pitching the airfoils at an AoA range from -2° up to 14°, with a frequency of 2.28 Hz based on the reduced frequency. These conditions were chosen based on nominal operation conditions for a rotorcraft at a cruise with an average load. These simulations used the URANS $SST - \gamma Re_\theta$ turbulence and transitional turbulence models.
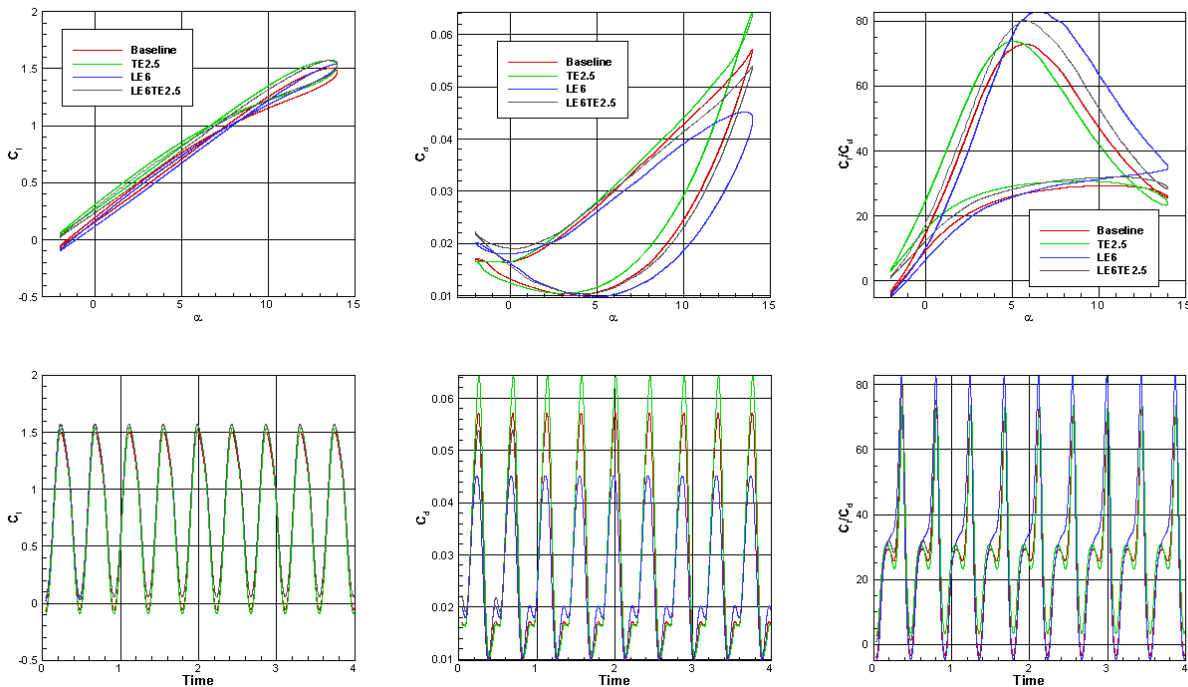
Fig. 23. Computed coefficient of lift, drag, and lift over drag at Re=250,000, C_l (left), C_d (middle), C_l/C_d (right)
Top row: vs AoA, Bottom row : vs Time

Figure 23 shows the computed C_l, C_d, and C_l/C_d, this data was used as an initial idea as to what deflection of leading and trailing edge is going to be needed at what angles of attack in order to optimize the airfoil shape dynamically to control the C_l/C_d performance. This data shows that on the upstroke from -2 to 4° AoA the trailing edge deflection of 2.5° is the most optimal, from 4 to 5.5° AoA the combination of leading edge deflection 6° and trailing edge deflection of 2.5° is the most optimal, and from 5.5 to 14° AoA the leading edge deflection performed the best. Then on the downstroke from 14 to 11° AoA the leading edge deflection of 6° is the most optimal, from 11 to 7° AoA the combination of leading edge deflection of 6° and trailing edge deflection of 2.5° is most optimal, and from 7 to -2° the trailing edge deflection of 2.5° is most optimal. This data is summarized in Table 1 below.

The data also shows that the increase in C_l/C_d wasn't solely reliant on an increase in the lift coefficient. For the leading edge deflection, it can be seen that the lift coefficient is slight greater than that of the baseline airfoil, but much of its performance increase comes from the decrease in drag coefficient due to the leading edge deflection maintaining flow separation over a majority of the airfoil. This is unlike the trailing edge deflection where the increase in performance comes from an increase in lift as the drag values remain very close to that of the baseline VR-12.

Table 1. Optimal shape deflection for AoA -2 to 14°

| Range of AoA	Optimal Deflection
Upstroke	
-2 to 4°	TE2.5
4 to 5.5°	LE6TE2.5
5.5 to 14°	LE6
Downstroke	
14 to 11°	LE6
11 to 7°	LE6TE2.5
7 to -2°	TE2.5

The results of these test do not consider of the dynamic morphing of the airfoil surfaces which will inevitably have an effect on the performance of the airfoil. The statically morphed pitching airfoil tests show that a regime can be developed where a vast improvement is seen over the entire regime when compared to the baseline airfoil. This data is used in the initial development of a dynamic morphing regime of the VR-12.

The vorticity contours and coefficient of pressure distributions for the upstroke from 14° to -2° angle of attack can be seen below in figure 24. Starting at -2° angle of attack shown in figure 24a the third case from the left shows the trailing edge deflection of 2.5°. This case shows an improved pressure differential over the baseline airfoil. When compared to the leading edge of 6° second from the left and the combination case on the far right, the leading edge and combination cases produce an even greater pressure differential. At 6° angle of attack shown in figure 24b the leading edge deflection of 6°, second from the left, shows the best pressure differential compared to the trailing edge deflection and the combination case, making it the optimal deflection at this angle of attack. Lastly, in figure 24c, again the leading edge deflection of 6°, second from the left, shows the best performance in terms of providing an increase in pressure differential over the baseline VR-12.

Figure 25 shows τ_{xy}/Dynamic pressure along the surface of the airfoil. In figure 25a and 25b there is no major point of flow seperation of where $\boldsymbol{\tau_{xy}}$/Dynamic pressure is below zero. Moving to the last case in figure 25c the leading edge deflection delays the onset of seperation by 0.1c. This results in an overall 25% reduction in the size of the seperation near the trailing edge of the airfoil resulting in less drag induced by circulating flow. The next set of data will analyze the same angles of attack for the downstroke from 14° to -2° angle of attack.
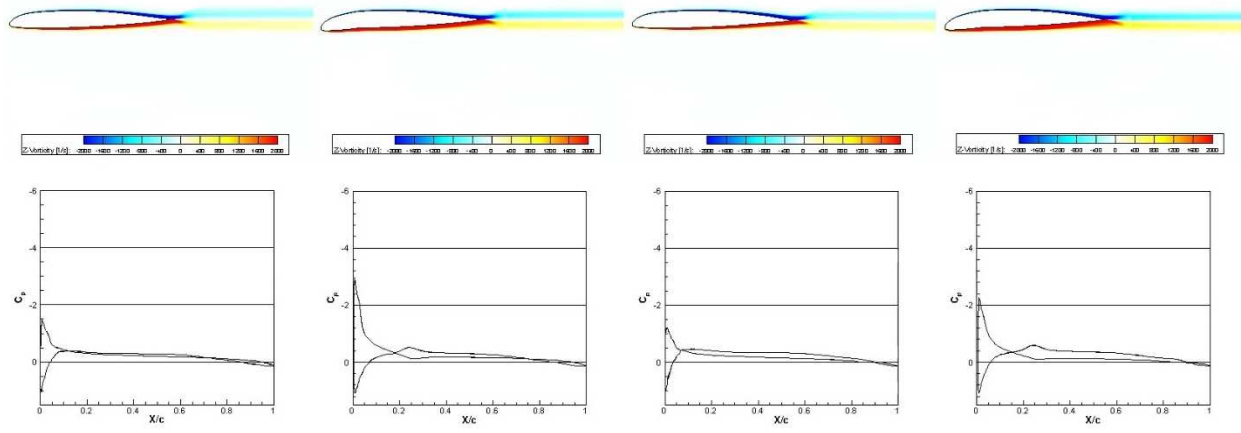
(a) -2° AoA
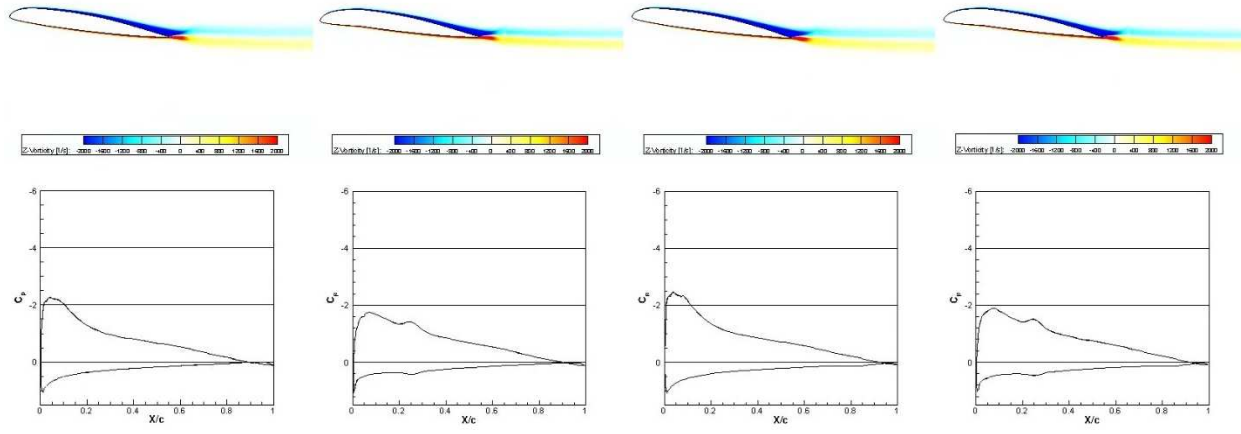
(b) 6° AoA
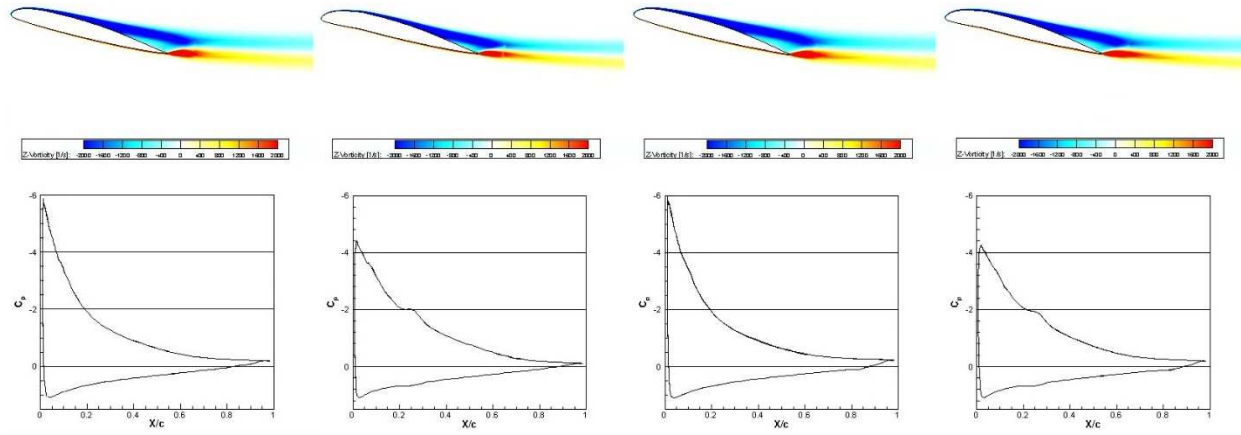
(c) 14° AoA

Fig. 24. Static deflection upstroke from 14 to -2° vorticity contours (top) and *C$_p$* distribution (bottom) at Re=250,000: baseline (1st), LE6 (2nd), TE2.5 (3rd), combination (4th)
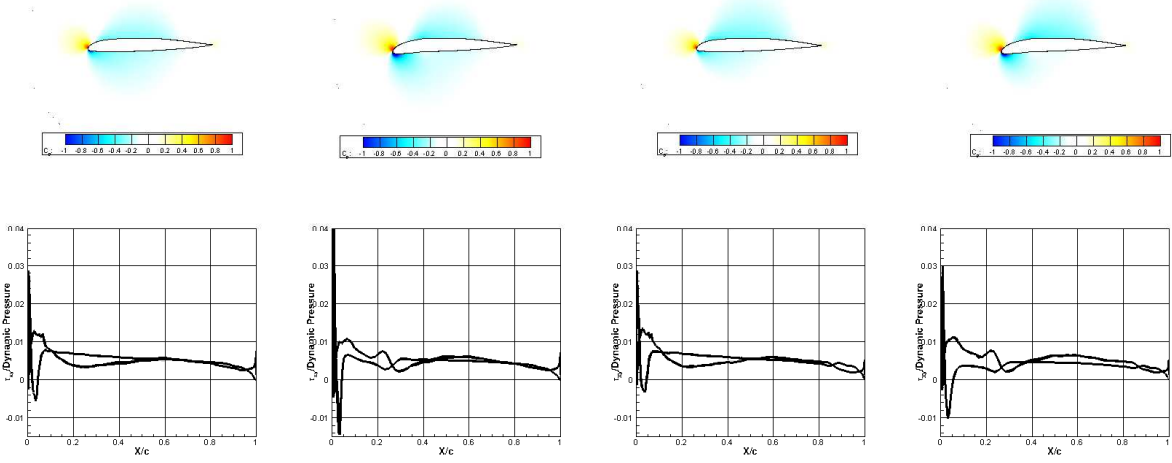
(a) -2° AoA
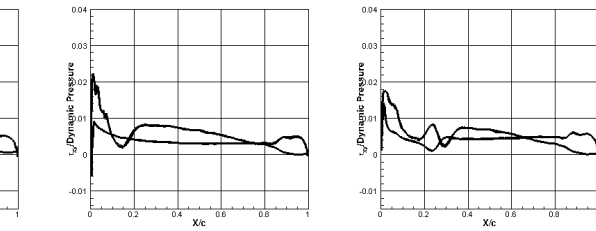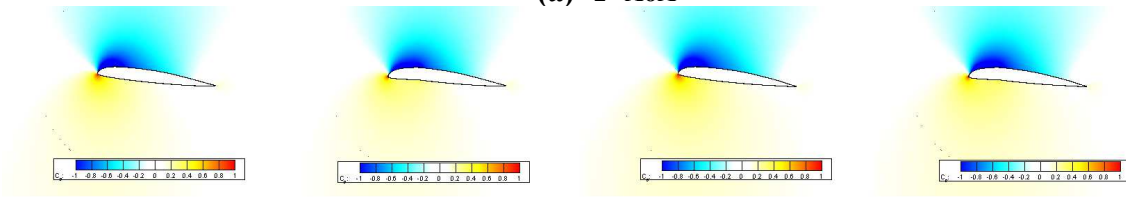
(b) 6° AoA
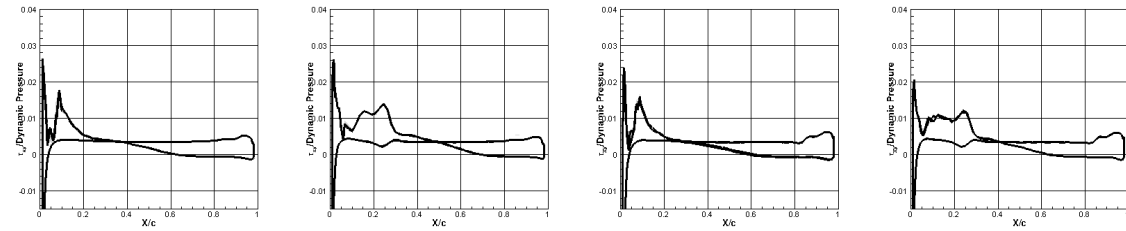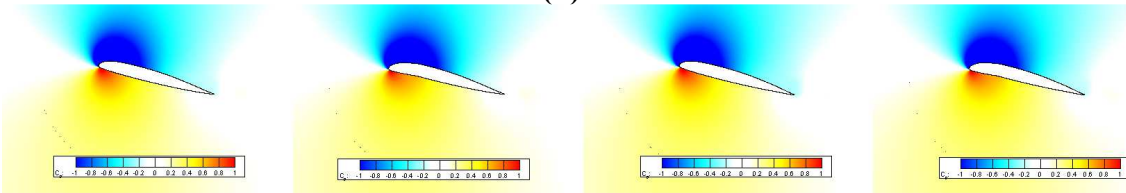
(c) 14° AoA

Fig. 25. Static deflection upstroke from 14 to -2° coefficient of pressure contours (top) and τ_{xy}/Dynamic pressure (bottom) at Re=250,000: baseline (1st), LE6 (2nd), TE2.5 (3rd), Combination (4th)

The coefficient of pressure distributions for the downstroke from 14° to -2° angle of

attack can be seen below in figure 26. The first set of data in figure 26a at -2° angle of attack

shows that the 2.5° trailing edge deflection produces greater pressure differential when compared

to the baseline. The leading edge and combination cases also create a larger pressure differential

than the baseline case. Figure 26b shows the four cases at the median angle of attack of 6°, here

the combination case is showing the largest pressure differential when compared to all other

cases. This shows that the combination case is going to create the most lift. Figure 26c shows the

comparison at 14° angle of attack, here the trailing edge deflection case shows the largest

pressure differential. When looking at the leading edge and combination case they show very

similar pressure distributions.

Figure 27a and 27b show very no flow reaching a value below zero signifying that there

is no recirculating flow to cause extra drag on the airfoil. Figure 27c shows a reduction in the

length of separation by 0.8c which correlates to a 20% reduction in the size of separation. This
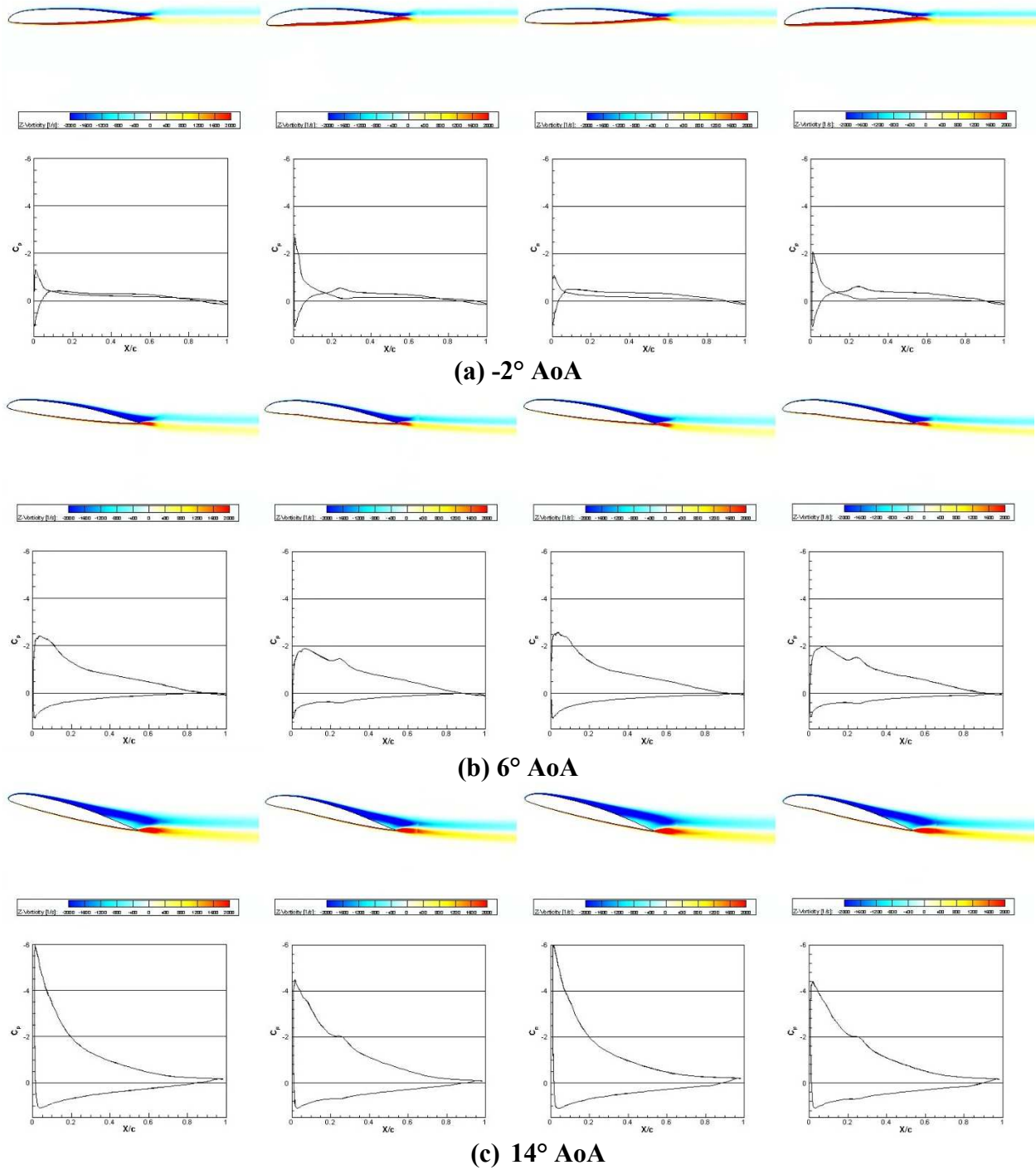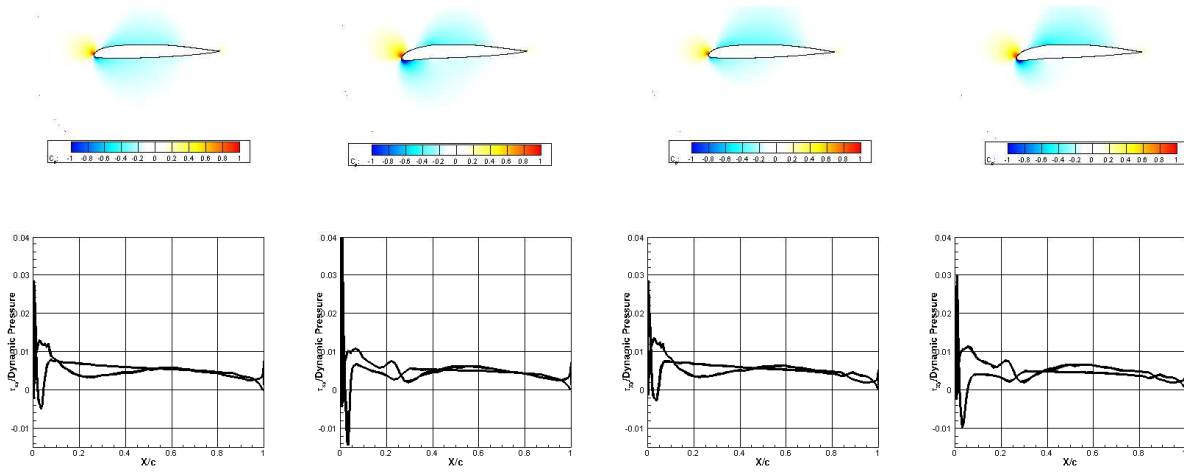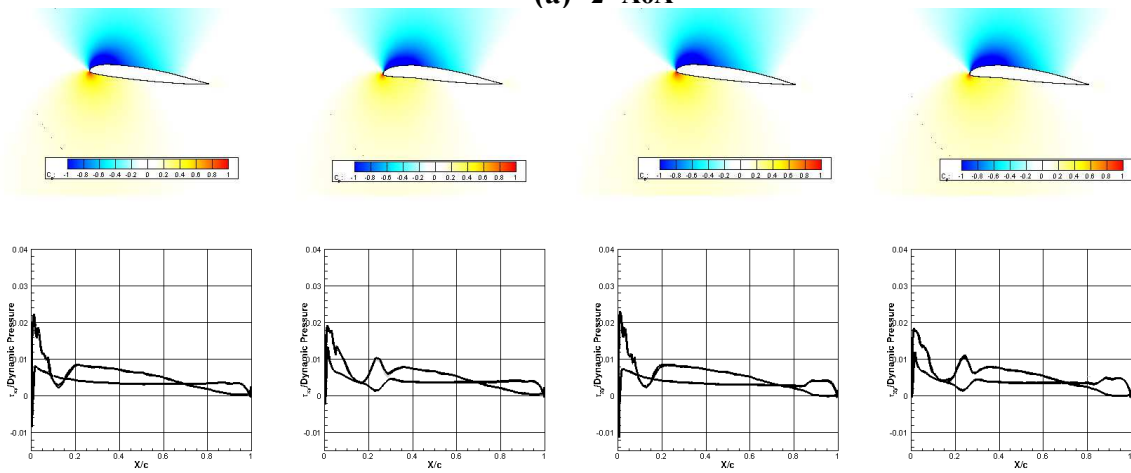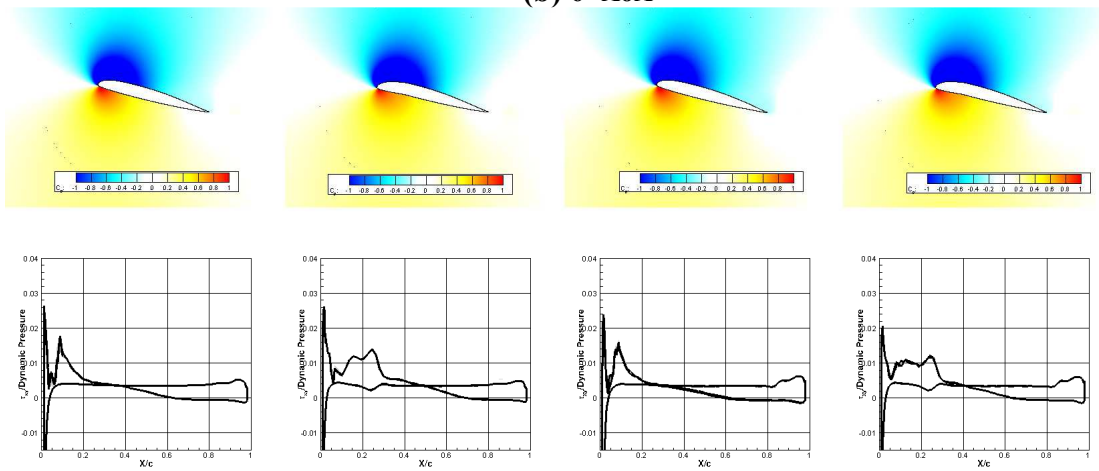
results in a reduction in drag due to recirculating flow.

(a) -2° AoA

(b) 6° AoA

(c) 14° AoA

Fig. 26. Static deflection downstroke from 14 to -2° vorticity contours (top) and C_p distribution (bottom) at Re=250,000: baseline (1st), LE6 (2nd), TE2.5 (3rd), combination (4th)

60

(a) -2° AoA

(b) 6° AoA

(c) 14° AoA

Fig. 27. Static deflection downstroke from 14 to -2° coefficient of pressure contours (top) and τ_{xy}/Dynamic pressure (bottom) at Re=250,000: baseline (1st), LE6 (2nd), TE2.5 (3rd), Combination (4th)

7.2.2. Pitching Dynamic Morphing Airfoil

Using the data from the static morphed pitching airfoil tests from the previous section as an initial guide to developing a dynamic morphing airfoil regime that will outperform the baseline VR-12 airfoil, the following morphing regime was developed. The airfoil will begin at -2° angle of attack with a trailing edge deflection of 4°, as it is pitching up the trailing edge deflection will begin to relax as the leading edge deflection begins to increase. At the median angle of attack of 6° the leading edge deflection will be at 3° while the trailing edge deflection will be at 2°. As the angle of attack begins to pass the halfway point of 8° the leading edge deflection will continue to increase until it reaches its max of 6° deflection at 14° angle of attack, the trailing edge will continue to relax until it reaches zero deflection at 14° angle of attack. This same regime will be repeated for the down stroke starting with a leading edge deflection of 6° and ending in a trailing edge deflection of 4°. The motion described is visualized in figure 28 below.
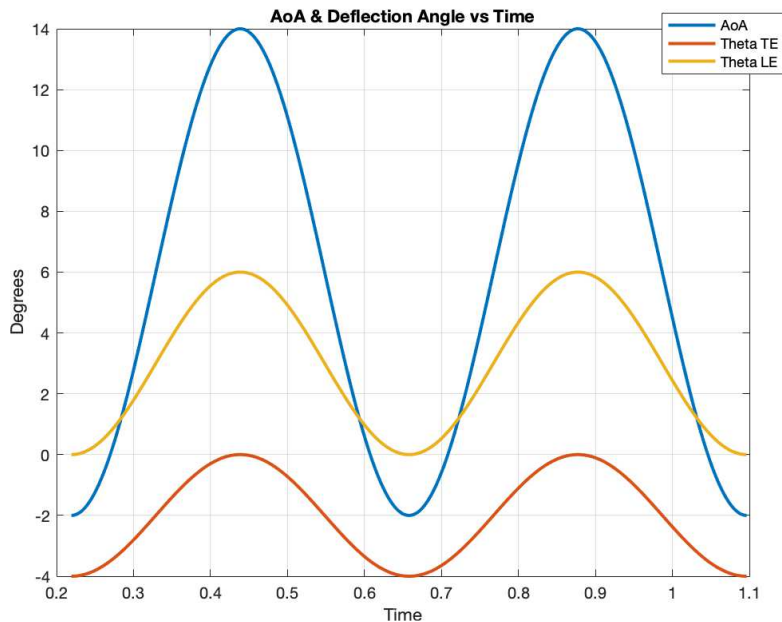

Fig. 28. Angle of attack (blue), leading edge deflection (yellow), and trailing edge deflection (orange) vs Time for the dynamic morphing and pitching case

62

It is important to note that the frequency for pitching, leading edge morphing, and trailing edge morphing is 2.28 Hz. All three motions will use the same pitching frequency so that the morphing regime will perfectly line up with the pitching regime as to mimic the optimal results found from static testing in the previous section.
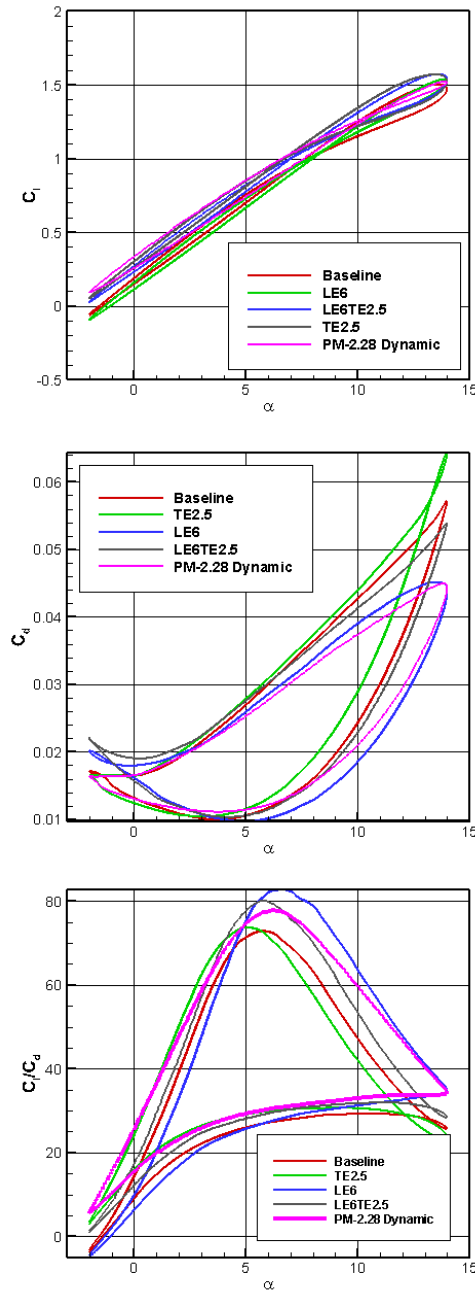

Fig. 29. Computed coefficient of lift, drag, and lift over drag vs AoA at Re=250,000, C_l (top), C_d (middle), C_l/C_d (bottom)

The initial test results of the dynamic morphing and pitching case can be seen above in figure 29, the dynamic morphing and pitching case corresponds to the pink line and is compared with the results of the static morphed pitching airfoil tests. The dynamic morphing case shows that it does in fact perform better than the baseline case. Looking at the far right plot of C_l/C_d, there is a 7% to 16% increase in performance for the dynamic morphing case when compared to the baseline case.
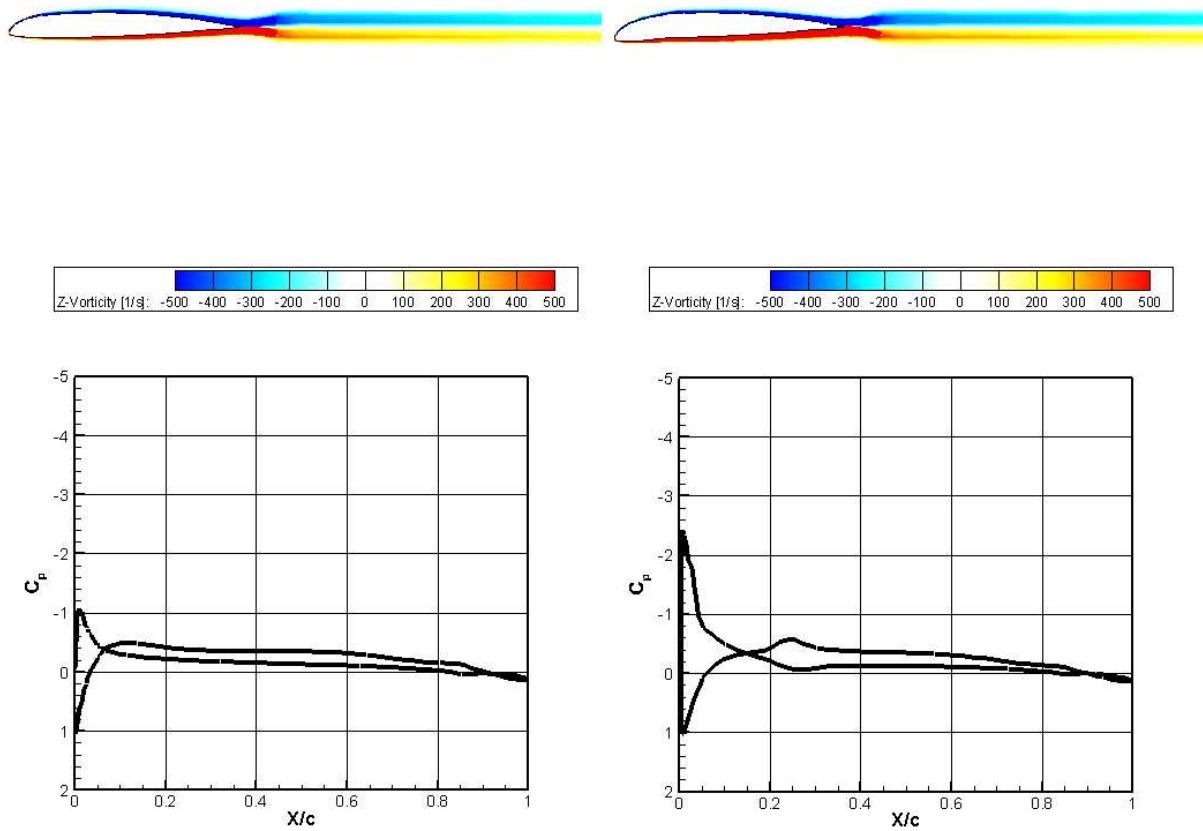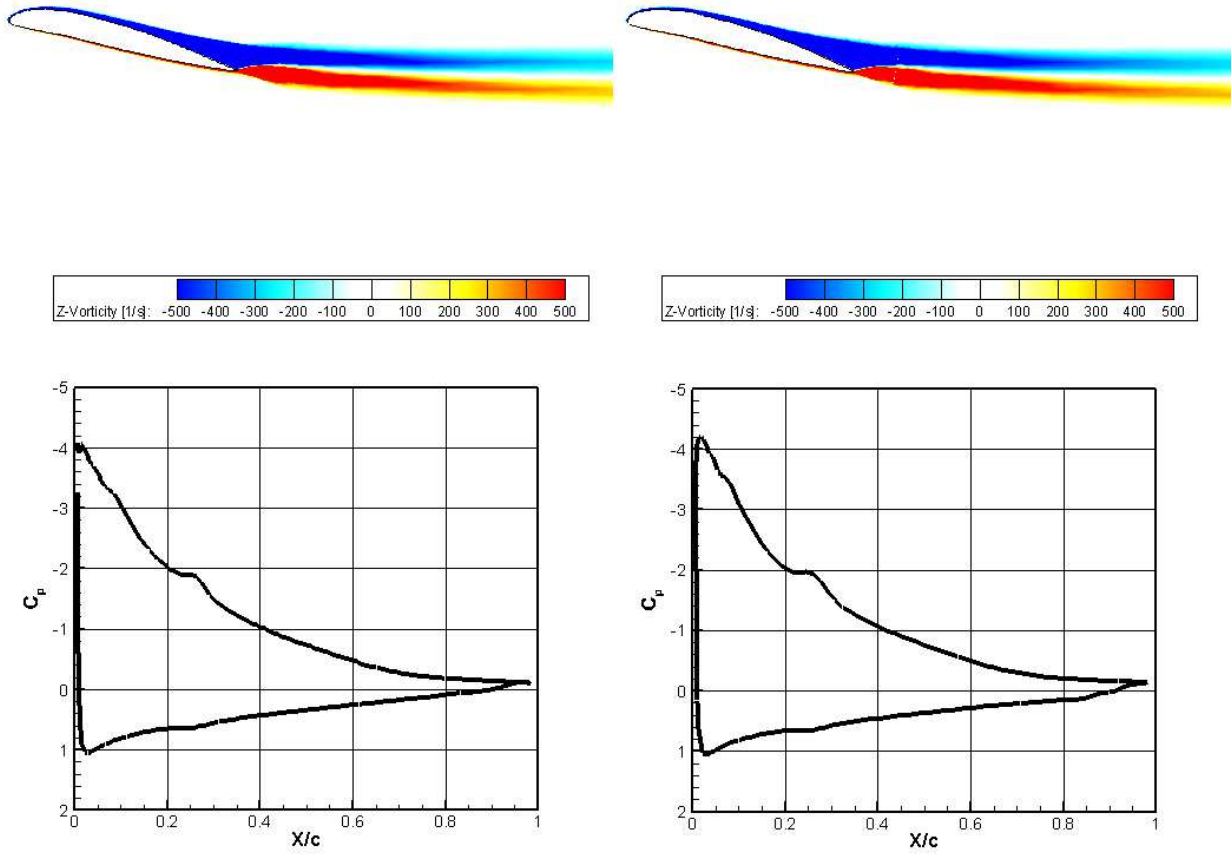

(a) -2° AoA

Fig. 30. Dynamic Morphing (left) vs Combination Deflection (right) upstroke from 14 to -2° vorticity contours (top) and coefficient of pressure distribution (bottom) at Re=250,000
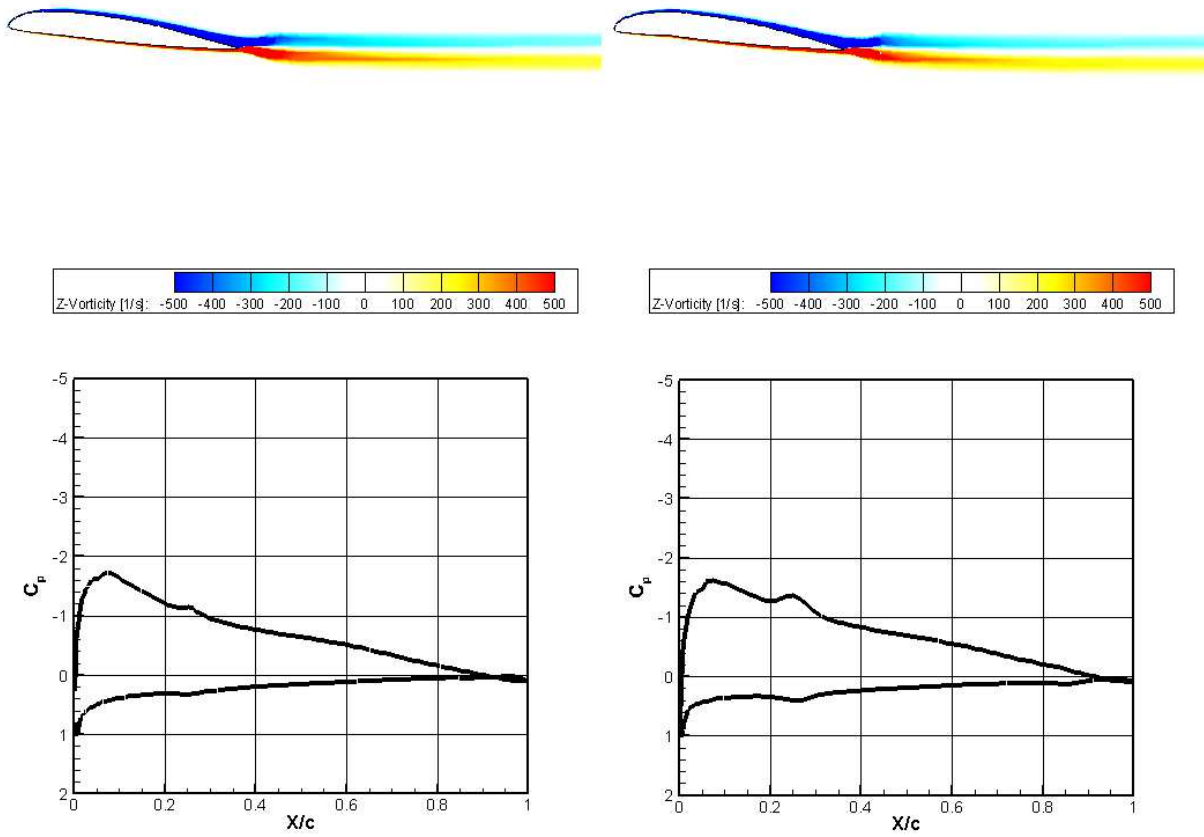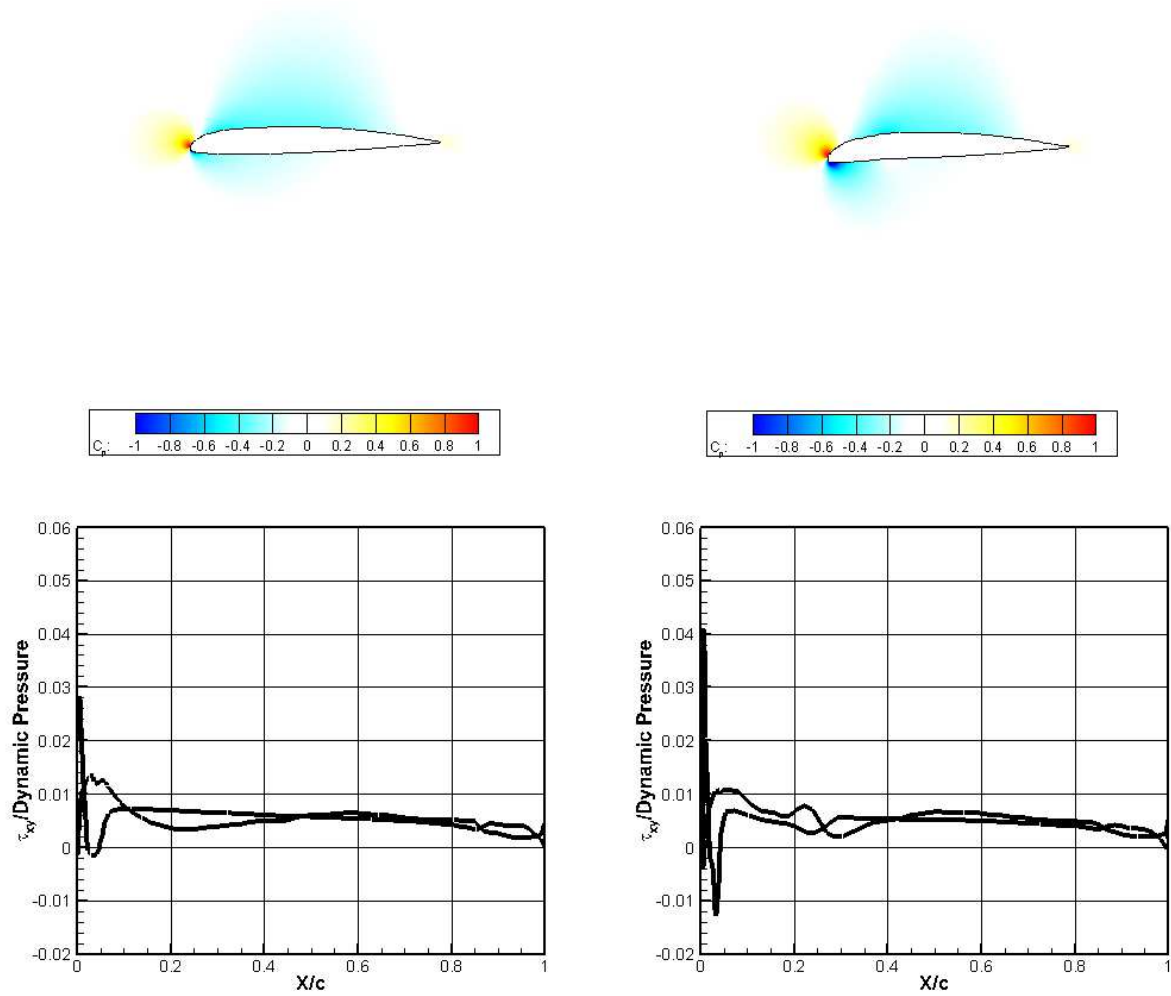
(b) 6° AoA

**Fig. 30. Dynamic Morphing (left) vs Combination Deflection (right) upstroke from 14 to -2°
vorticity contours (top) and coefficient of pressure distribution (bottom) at Re=250,000
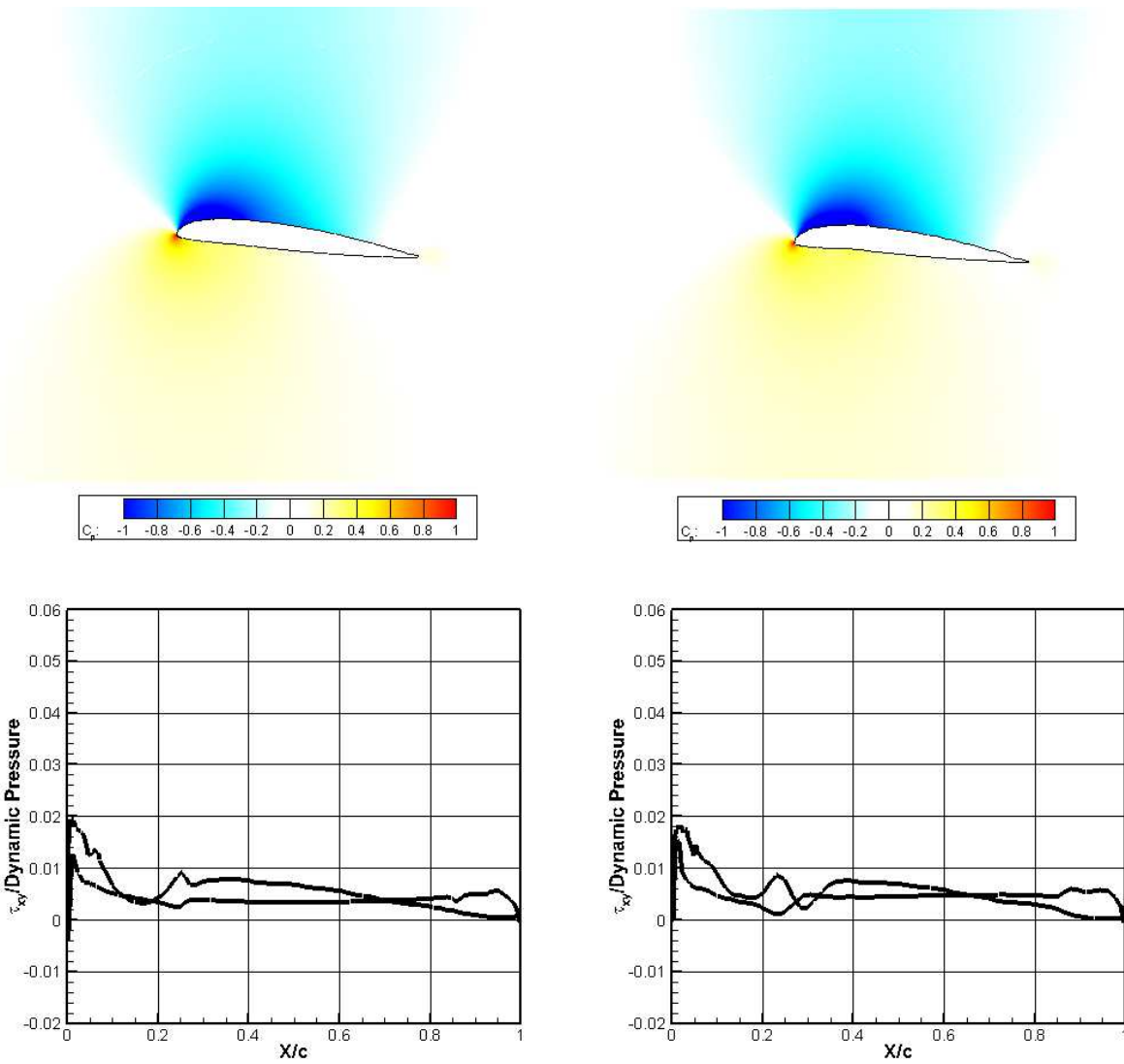(continued)**

(c) 14° AoA

Fig. 30. Dynamic Morphing (left) vs Combination Deflection (right) upstroke from 14 to -2° vorticity contours (top) and coefficient of pressure distribution (bottom) at Re=250,000 (continued)
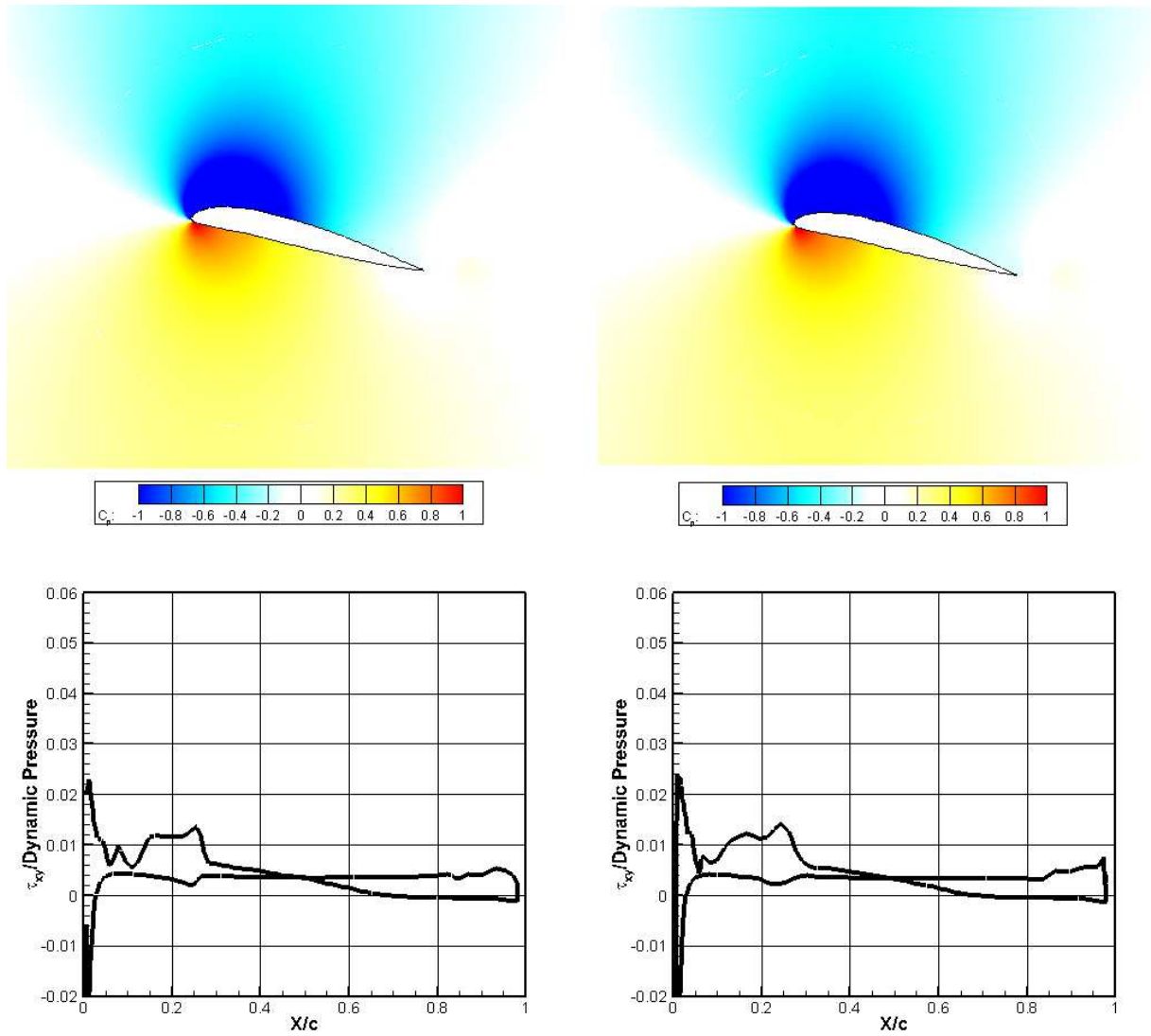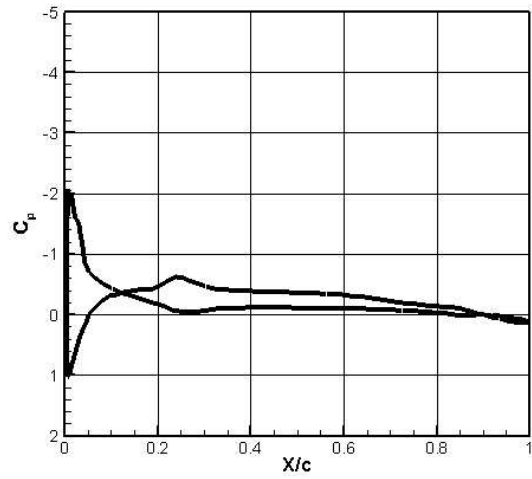
(a) -2° AoA

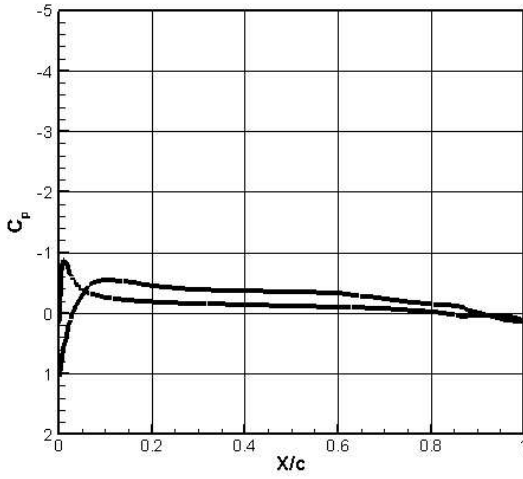**Fig. 31. Dynamic Morphing (left) vs Combination Deflection (right) upstroke from 14 to -2° coefficient of pressure contours (top) and τ_{xy}/Dynamic pressure (bottom) at Re=250,000**

(b) 6° AoA

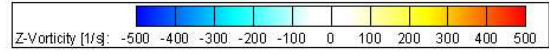**Fig. 31. Dynamic Morphing (left) vs Combination Deflection (right) upstroke from 14 to -2° coefficient of pressure contours (top) and τ_{xy}/Dynamic pressure (bottom) at Re=250,000 (continued)**

(c) 14° AoA

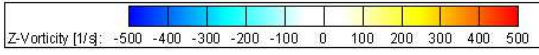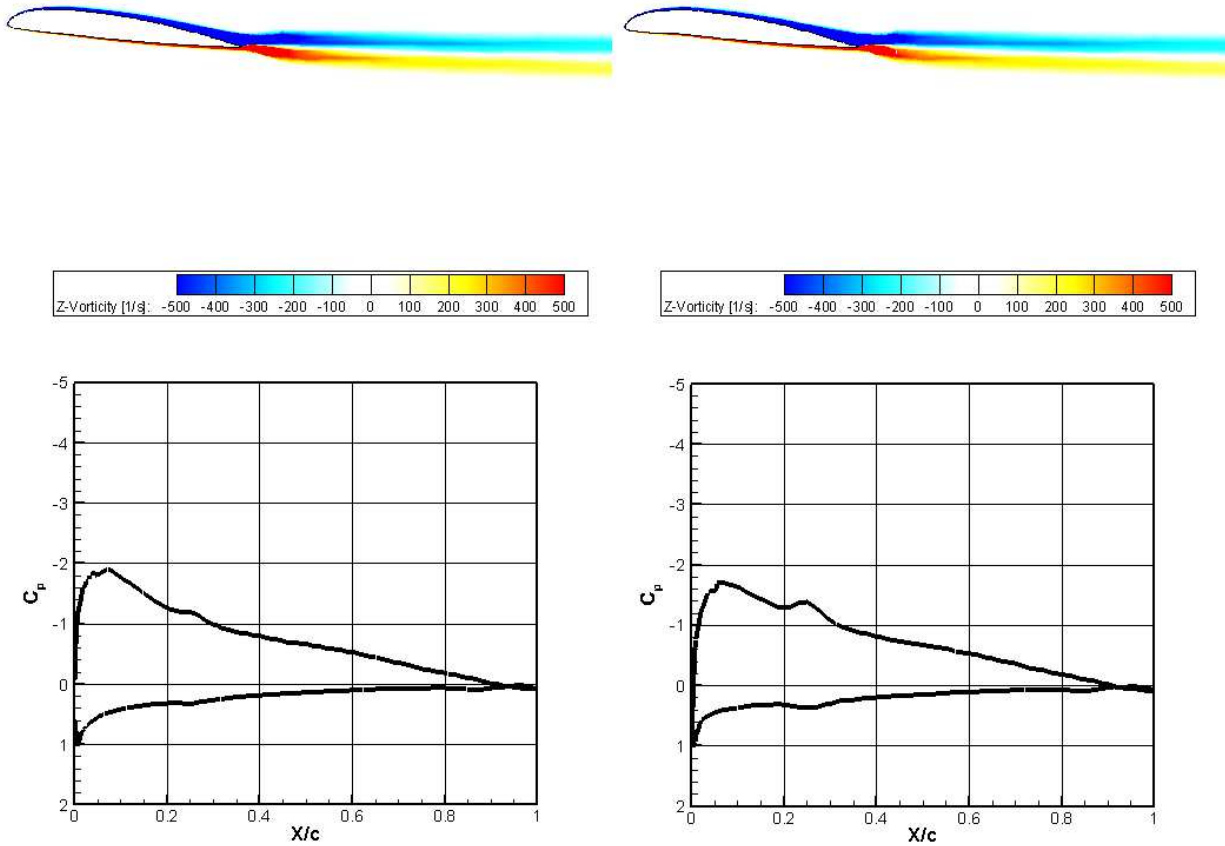**Fig. 31. Dynamic Morphing (left) vs Combination Deflection (right) upstroke from 14 to -2°
coefficient of pressure contours (top) and τ_{xy}/Dynamic pressure (bottom) at Re=250,000
(continued)**

The coefficient of pressure distributions and contours seen above in figures 30 and 31 show the difference in performance when comparing the dynamic morphing case (left) with the static morphed combination case (right) on the upstroke. Starting at -2° in figures 30a and 31a the dynamic case shows less pressure differential along the lower surface when compared to the static combination case. The reduced pressure differential may result in slightly less lift but also a reduction in drag due to less separation near the leading edge overall improves the $\frac{c_l}{c_d}$ for the dynamic morphing airfoil. Next, in figures 30b and 31b at 6° angle of attack there is little to no discernable difference between the static and dynamic morphing airfoil. Referencing table 1 the two cases are expected to show very similar performance near 6° angle of attack. Lastly, in figure 30c and 31c at 14° angle of attack the static and dynamic cases show very similar pressure differentials resulting in similar lift, but the dynamic airfoil takes advantage of the ability to relax the trailing edge deflection at higher angles of attack and this resulted in less separation.
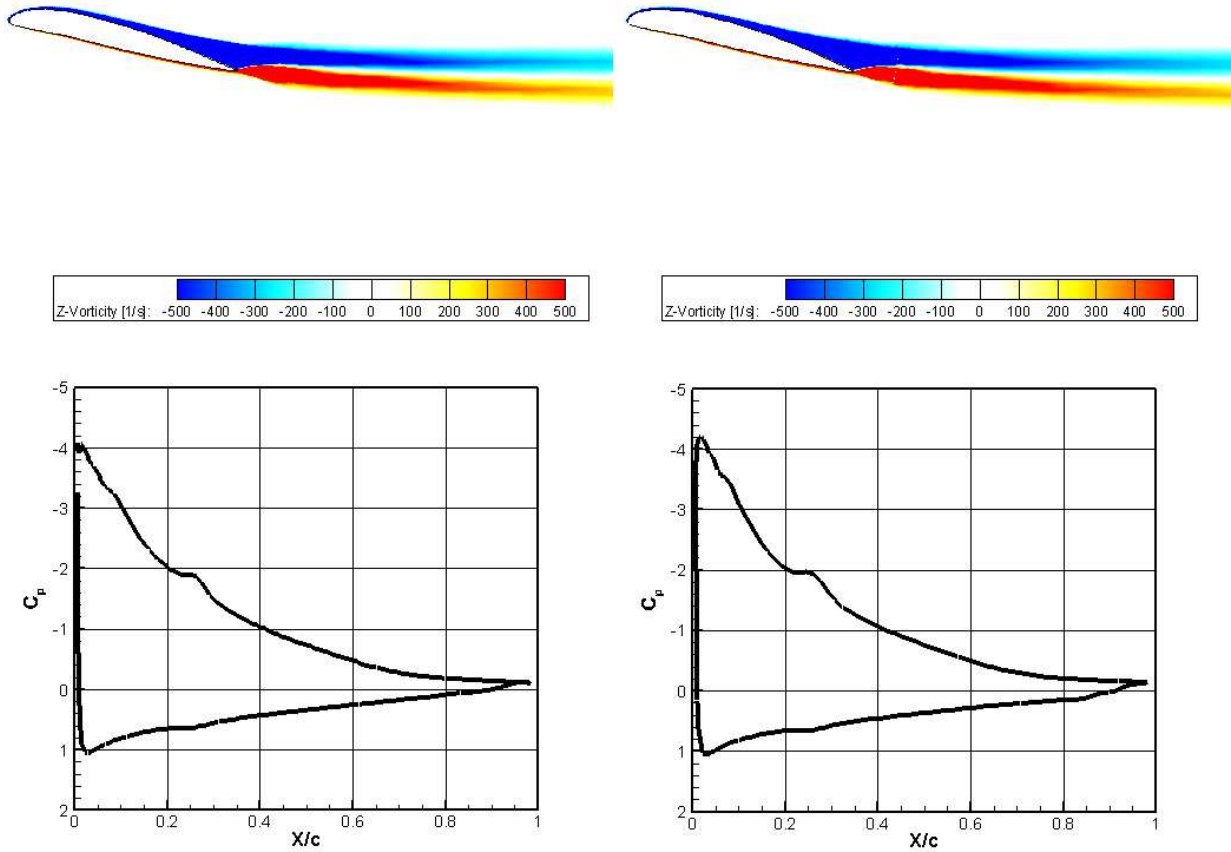
(a) -2° AoA

Fig. 32. Dynamic Morphing (left) vs Combination Deflection (right) downstroke from 14 to -2° vorticity contours (top) and coefficient of pressure distribution (bottom) at Re=250,000

(b) 6° AoA

Fig. 32. Dynamic Morphing (left) vs Combination Deflection (right) downstroke from 14 to -2° vorticity contours (top) and coefficient of pressure distribution (bottom) at Re=250,000 (continued)

(c) 14° AoA

Fig. 32. Dynamic Morphing (left) vs Combination Deflection (right) downstroke from 14 to -2° vorticity contours (top) and coefficient of pressure distribution (bottom) at Re=250,000 (continued)
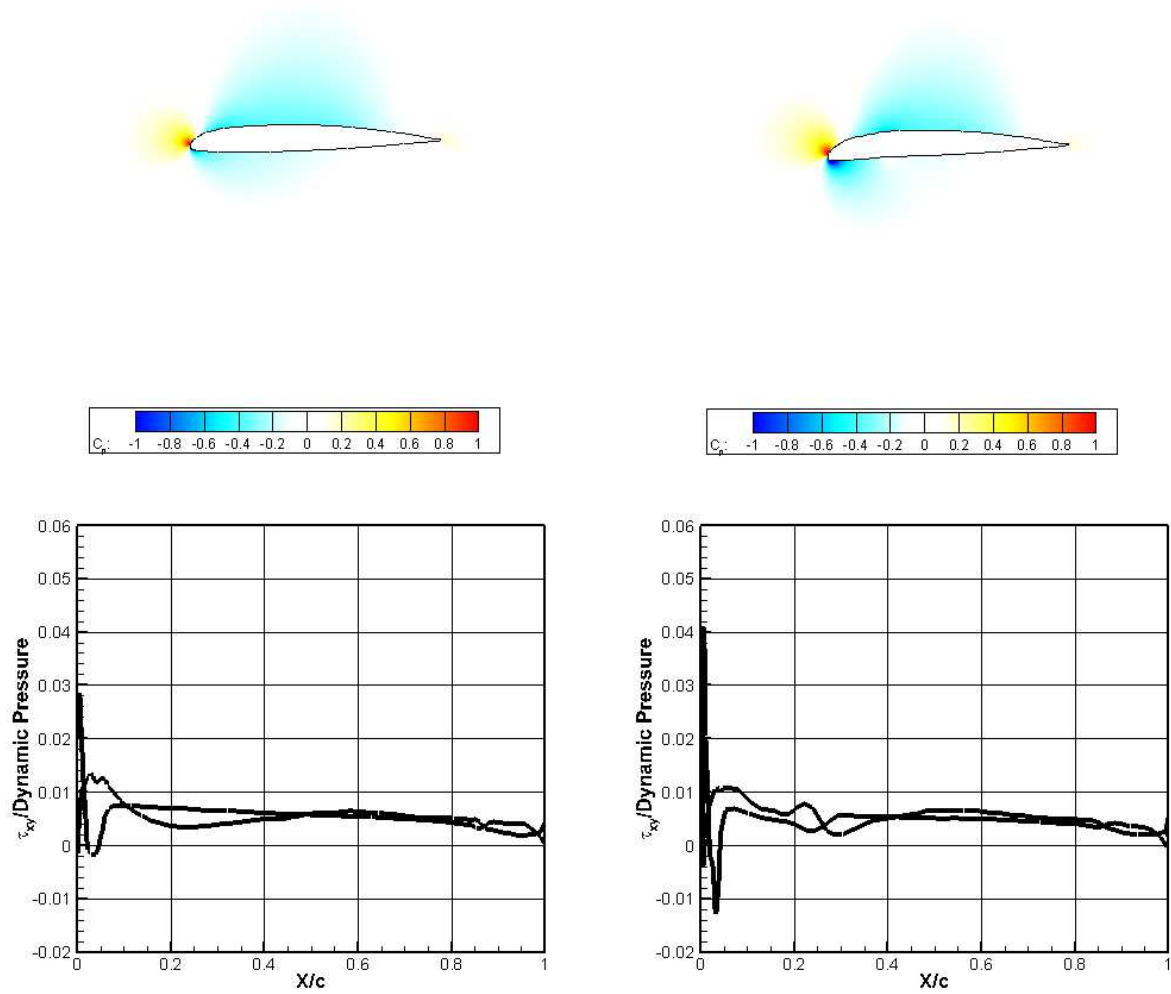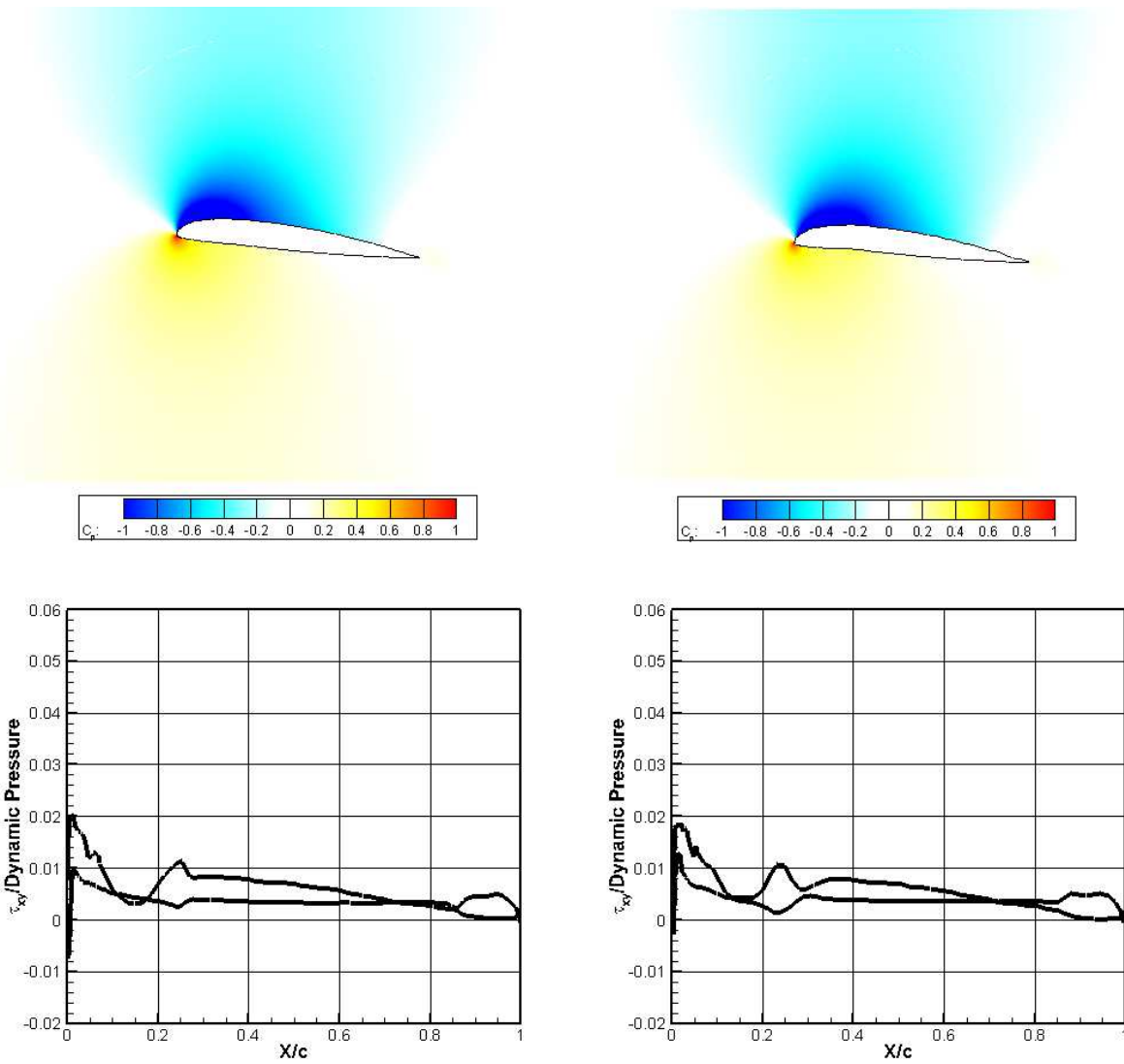
(a) -2° AoA

Fig. 33. Dynamic Morphing (left) vs Combination Deflection (right) downstroke from 14 to -2° coefficient of pressure contours (top) and τ_{xy}/Dynamic pressure (bottom) at Re=250,000

(b) 6° AoA

Fig. 33. Dynamic Morphing (left) vs Combination Deflection (right) downstroke from 14 to -2° coefficient of pressure contours (top) and τ_{xy}/Dynamic pressure (bottom) at Re=250,000 (continued)
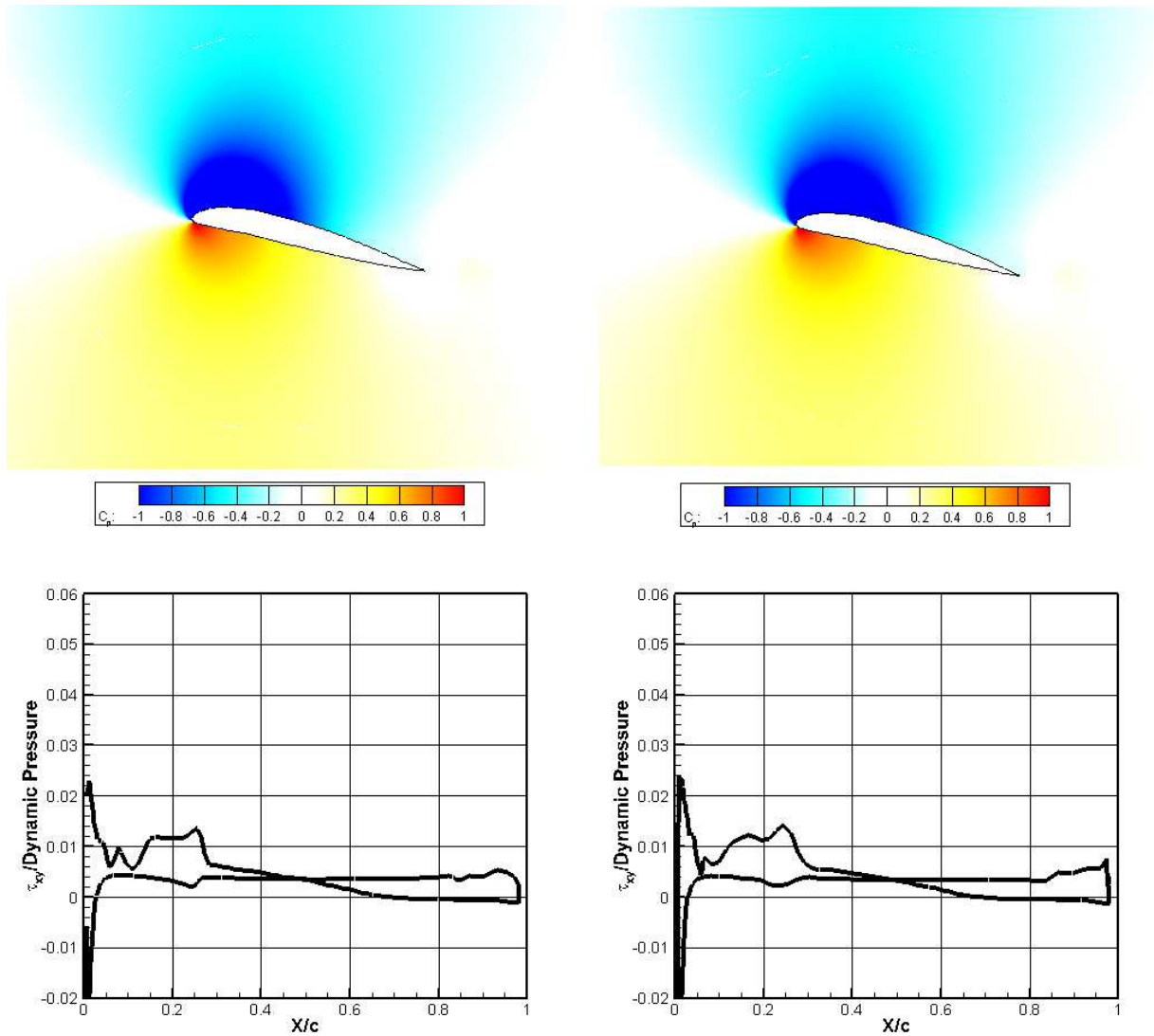
(c) 14° AoA

Fig. 33. Dynamic Morphing (left) vs Combination Deflection (right) downstroke from 14 to -2° coefficient of pressure contours (top) and τ_{xy}/Dynamic pressure (bottom) at Re=250,000 (continued)

The plots seen above in figures 31 and 32 show the difference in performance when comparing the dynamic morphing case (left) with the static morphed combination case (right) on the downstroke. This data represents the down stroke from 14° to -2° angle of attack. In figures 32a and 33a the dynamic case is producing a smaller pressure distribution which will equate to less lift but it's producing much separation along the bottom surface when compared to the

combination case, which is caused by the deflected leading edge. This means that although the morphing case is producing less lift its also producing much less drag which requires less lift to overcome making it the superior case when comparing the aerodynamic efficiency. In figures 32b and 33b the dynamic morphing case produces a larger pressure differential as well as producing less separation, showing improved performance over the static morphed case. Last, in figures 32c and 33c at 14° angle of attack the two cases produce very similar pressure differentials, but the dynamic morphing case produces much less, resulting in lower overall drag on the airfoil. All three instances shown suggest that the dynamically morphing airfoil will outperform the static morphed airfoil as it can be set to a more optimal LE and TE deflection over a range of angles of attack.

Analysis of the data above shows that the range of angle of attack doesn't reach the upper limit of angel attack required to enter the dynamic stall region. In order to characterize the morphing leading and trailing edge performance in dynamic stall the range of angle of attack needed to be expanded. This resulted in two additional tests; baseline VR-12 and dynamic morphing VR-12 following the same dynamic morphing regime as the previous test, these tests were performed at range of angle of attack from -10 to 22°.
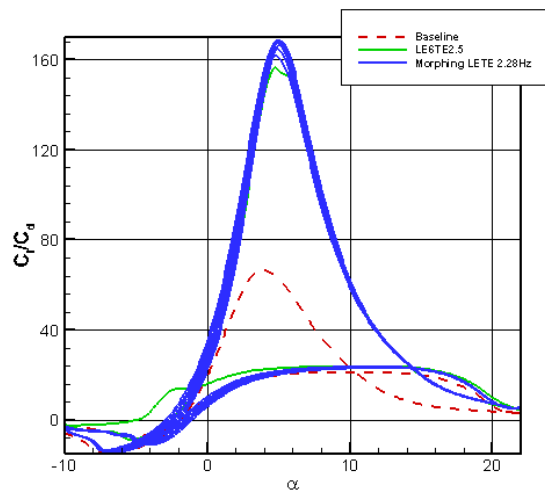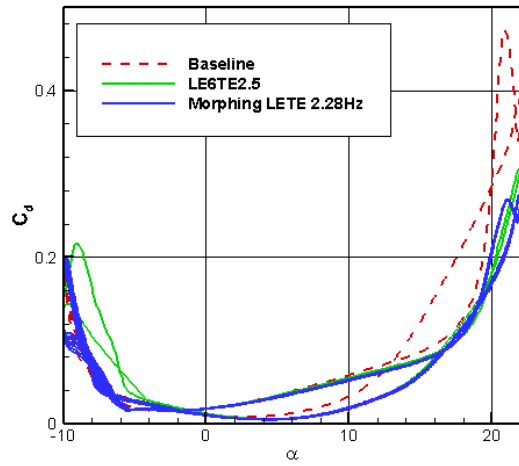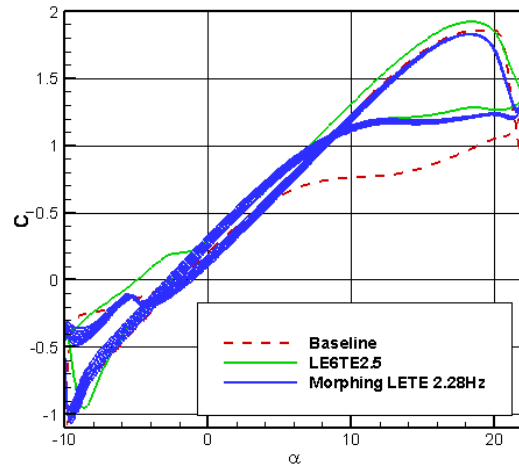
77

Fig. 34. Computed coefficient of lift, drag, and lift over drag vs AoA at Re=250,000, C_l (left), C_d (middle), C_l/C_d (right)

Utilizing the large range of angle of attack shows that the airfoil begins to experience dynamic stall near 20° angle of attack. Looking at the coefficient of lift above in figure 34 the baseline airfoil delays stall further until 21° when compared to the dynamic morphing case which enters stall closer to 18°. While the baseline airfoil reaches a higher angle of attack before entering the dynamic stall region, when it does enter dynamic stall it has a massive drop in coefficient of lift from 1.8 to 1.1 and continues to fall drastically until the angle of attack reaches 6°, compared to the dynamic morphing case which shows a drop in lift coefficient from 1.8 to 1.3 then remains very close to 1.3 until it recovers near 10° angle of attack, roughly 4° sooner than the baseline airfoil. The utilization of the dynamic drooping leading edge brings the airfoil out of stall nearly 4° sooner when compared to the baseline airfoil. Looking at the coefficient of drag and lift over drag it is clear the dynamic leading and trailing edge deflections allow for a reduction in drag due to maintaining flow attachment over the airfoil ultimately allowing for a great increase in the aerodynamic efficiency of the airfoil.

Also compared in figure 34, is the performance of the static combination deflection airfoil. This airfoil shows performance increase over the baseline and the morphing airfoil near the dynamic stall regime. The static combination airfoil doesn't enter stall until 21° similar to the baseline airfoil, then once in dynamic stall it shows similar performance to that of the morphing airfoil when the coefficient of lift only drops to about 1.3 then remains steady until recovery out of dynamic stall near 10° angle of attack on the downstroke.

Further analysis of different frequencies of morphing and combinations of morphing deflections near the dynamic stall region are required in order to properly identify an optimal morphing regime to alleviate the effects of dynamic stall.
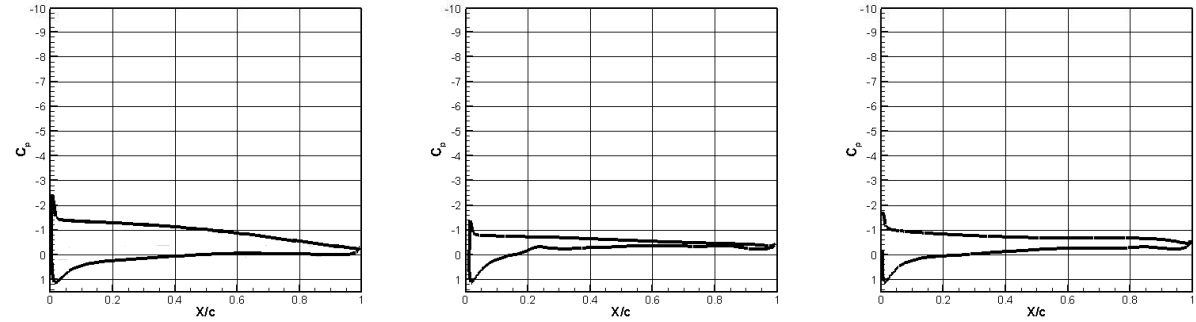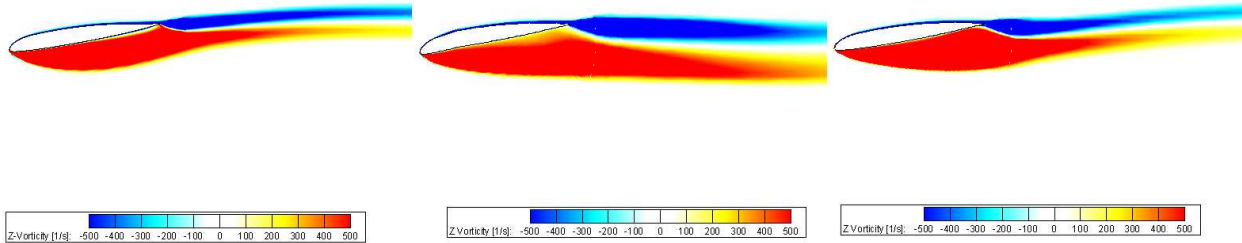
(a) AoA=-10, $\theta_{LE} = 0, \theta_{TE} = 4$
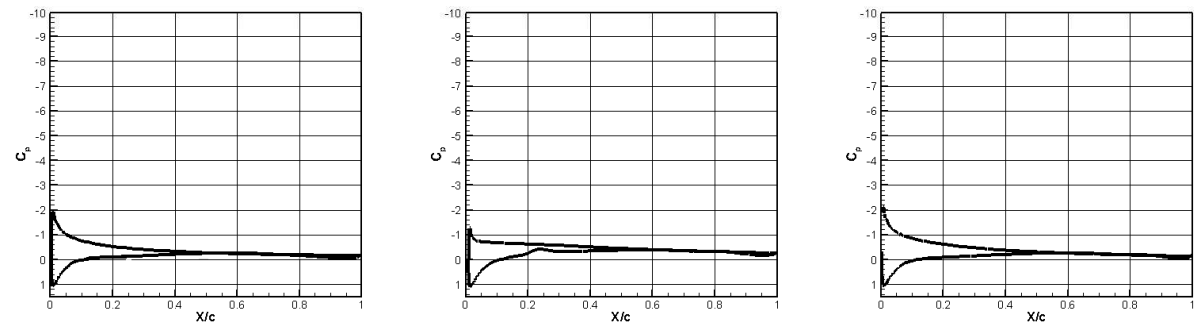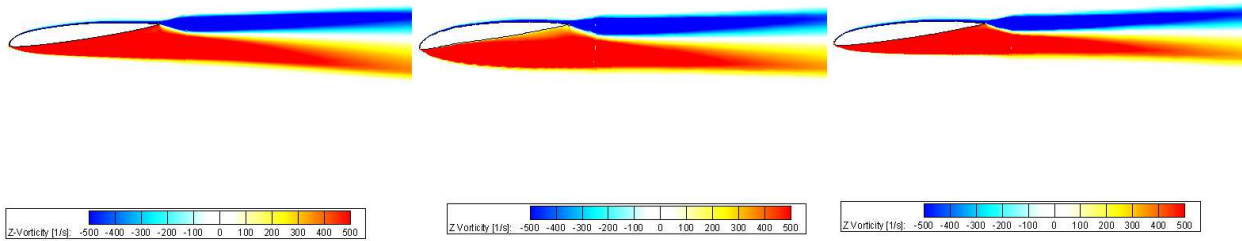
(b) AoA=-7.7, $\theta_{LE} = -0.4, \theta_{TE} = 3.7$

Fig. 35. Baseline VR-12 (left) vs Dynamic Morphing (middle) vs Combination (right) upstroke from -10 to 22° vorticity contours (top) and coeffecient of pressure distribution (bottom) at Re=250,000

(c) AoA=14.7, $\theta_{LE} = -4.6, \theta_{TE} = 1$

(d) AoA=21.3, $\theta_{LE} = -5.9, \theta_{TE} = 0.08$

Fig. 35. Baseline VR-12 (left) vs Dynamic Morphing (middle) vs Combination (right) upstroke from -10 to 22° vorticity contours (top) and coeffecient of pressure distribution (bottom) at Re=250,000 (continued)

(e) AoA=22, $\theta_{LE} = -6, \theta_{TE} = 0$

Fig. 35. Baseline VR-12 (left) vs Dynamic Morphing (middle) vs Combination (right) upstroke from -10 to 22° vorticity contours (top) and coeffecient of pressure distribution (bottom) at Re=250,000 (continued)
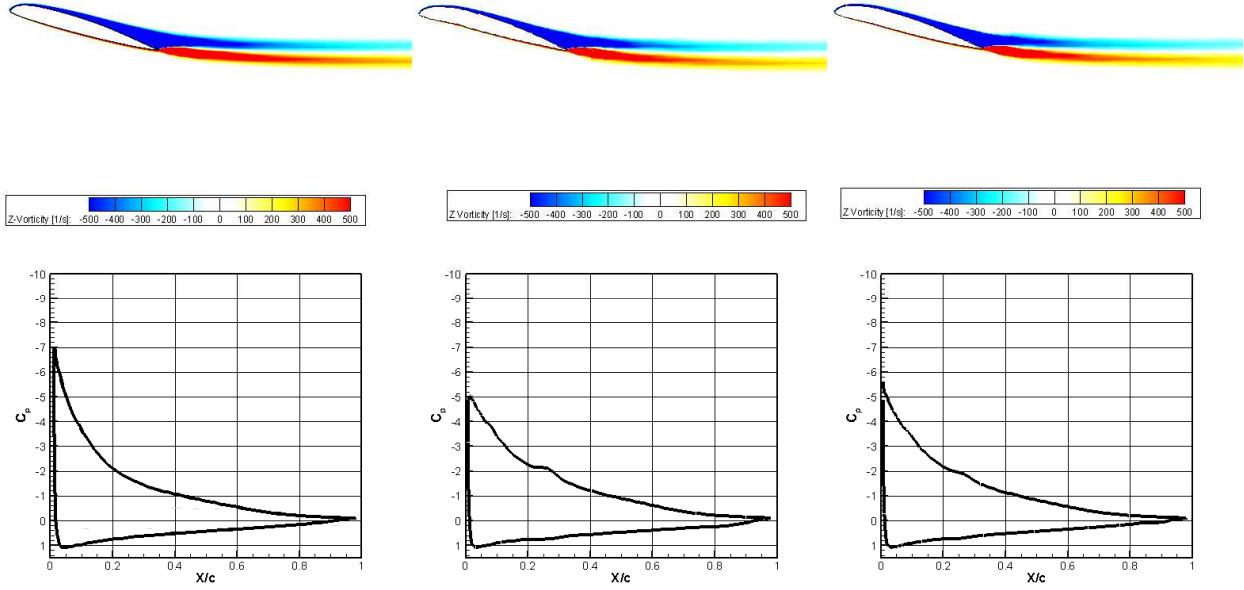
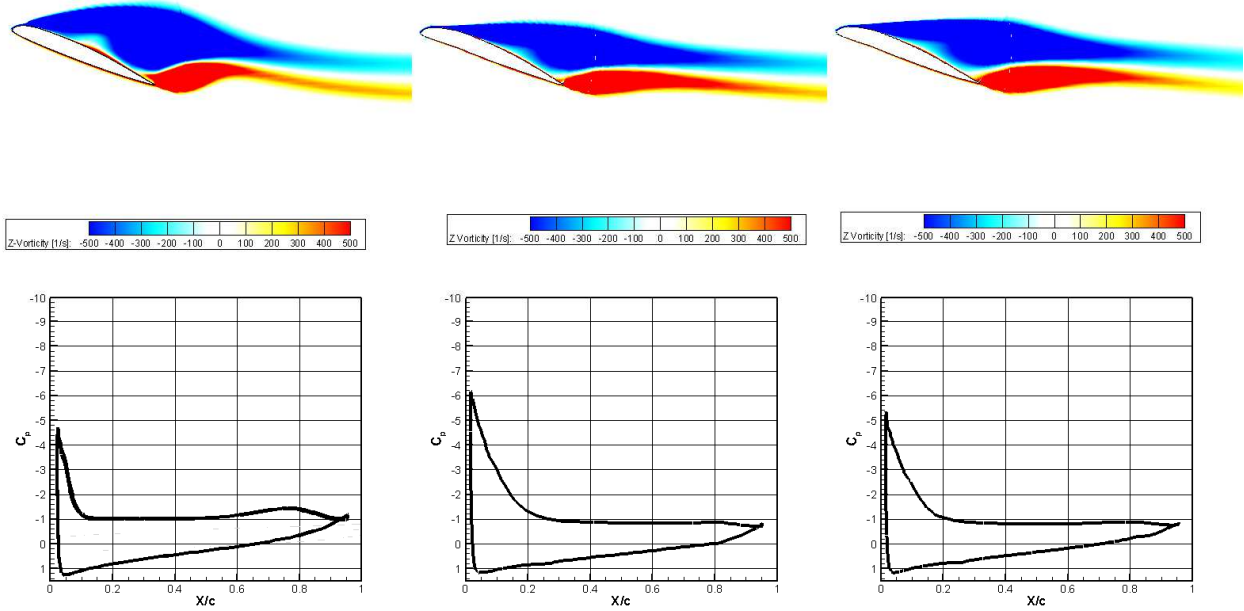**(a) AoA=-10, $\theta_{LE} = 0$, $\theta_{TE} = 4$**

(b) AoA=-7.7, $\theta_{LE} = -0.4$, $\theta_{TE} = 3.7$
Fig. 36. Baseline VR-12 (left) vs Dynamic Morphing (middle) vs Combination (right)
upstroke from -10 to 22° coefficient of pressure (top) and τ_{xy}/Dynamic pressure (bottom) at
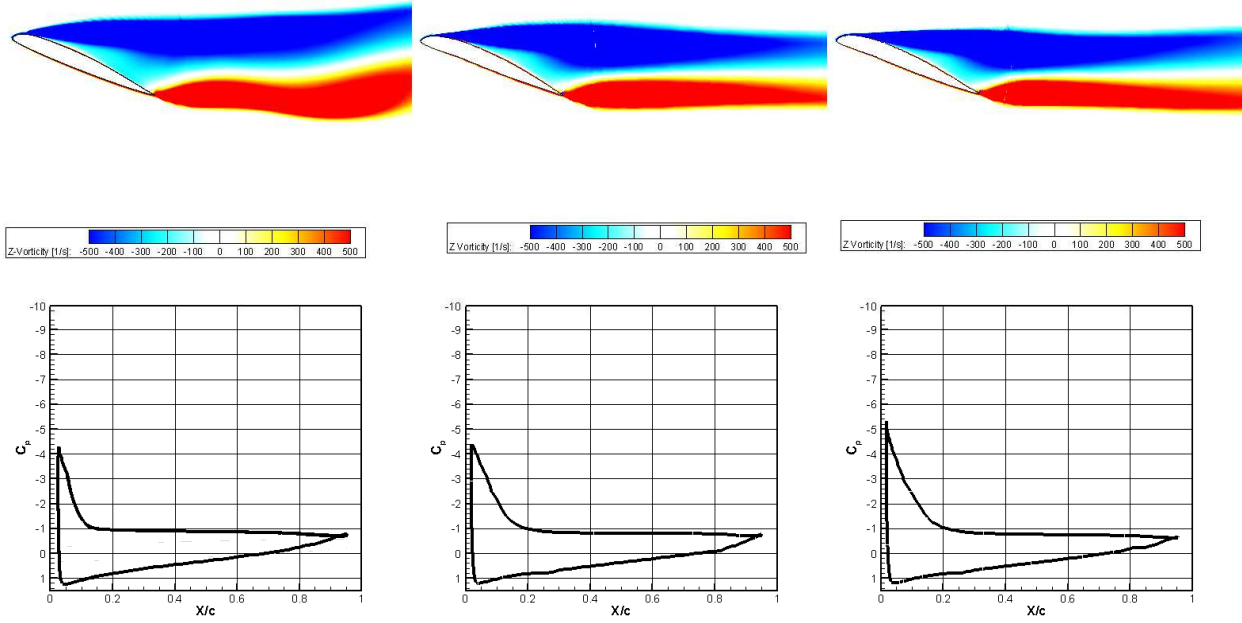**Re=250,000**

83
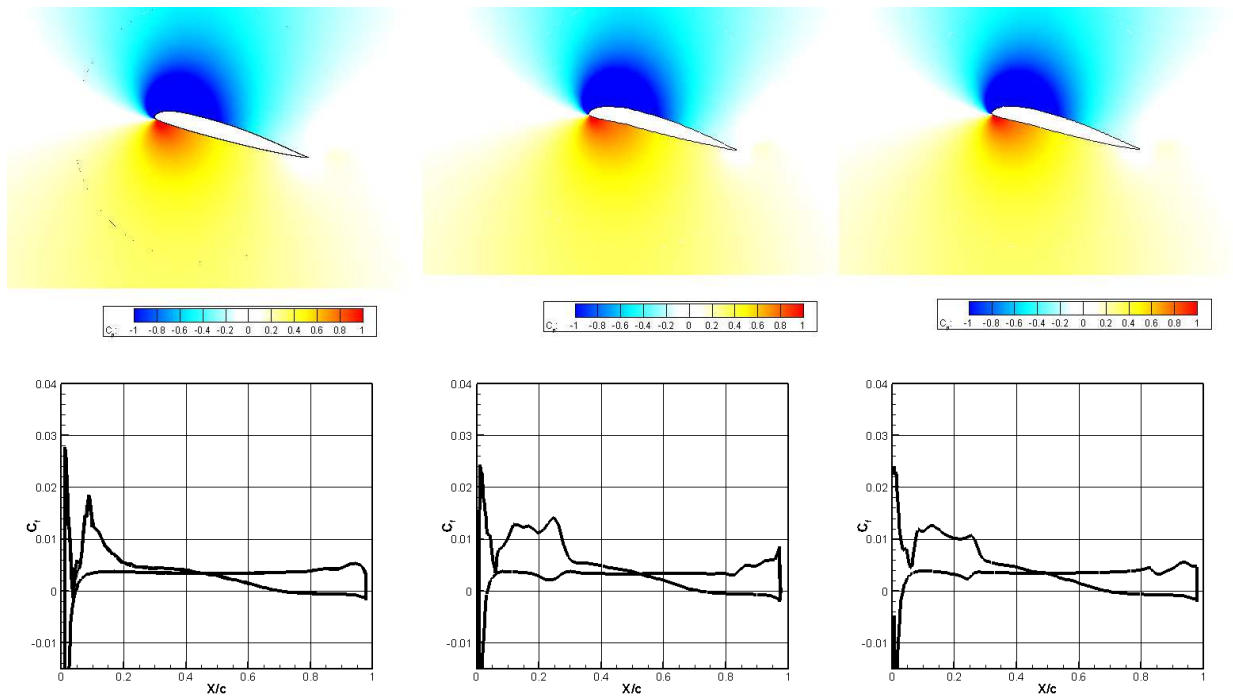
(c) AoA=14.7, $\theta_{LE} = -4.6, \theta_{TE} = 1$

(d) AoA=21.3, $\theta_{LE} = -5.9, \theta_{TE} = 0.08$

Fig. 36. Baseline VR-12 (left) vs Dynamic Morphing (middle) vs Combination (right) upstroke from -10 to 22° coefficeint of pressure (top) and τ_{xy}/Dynamic pressure(bottom) at Re=250,000 (continued)
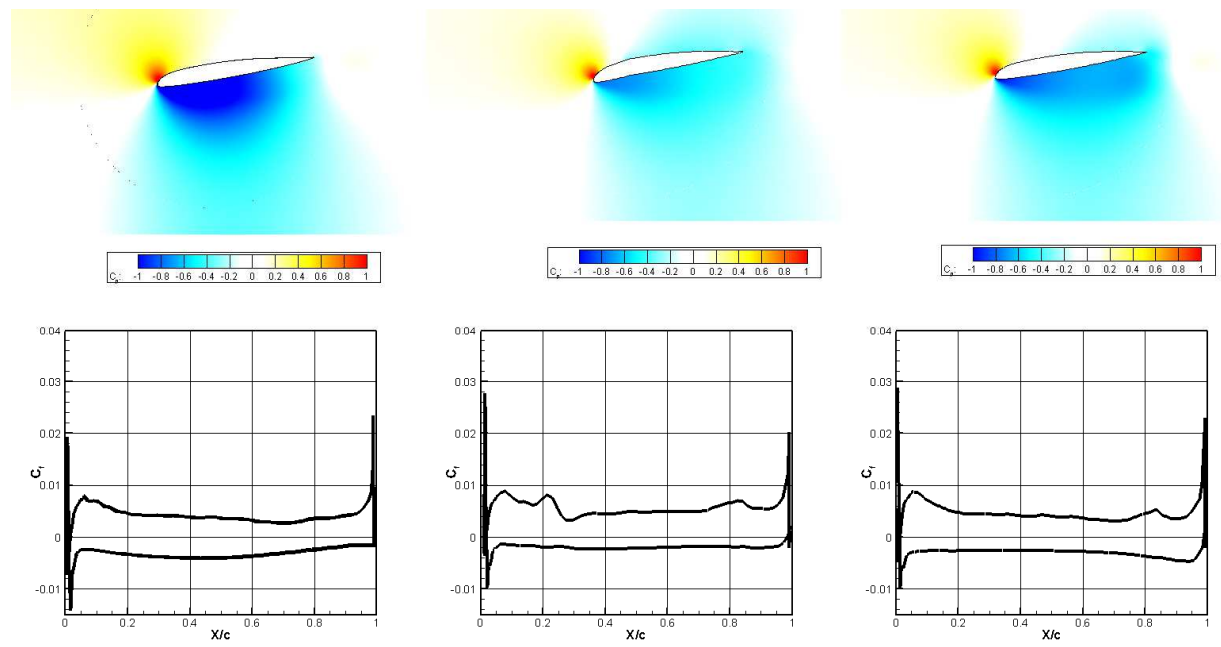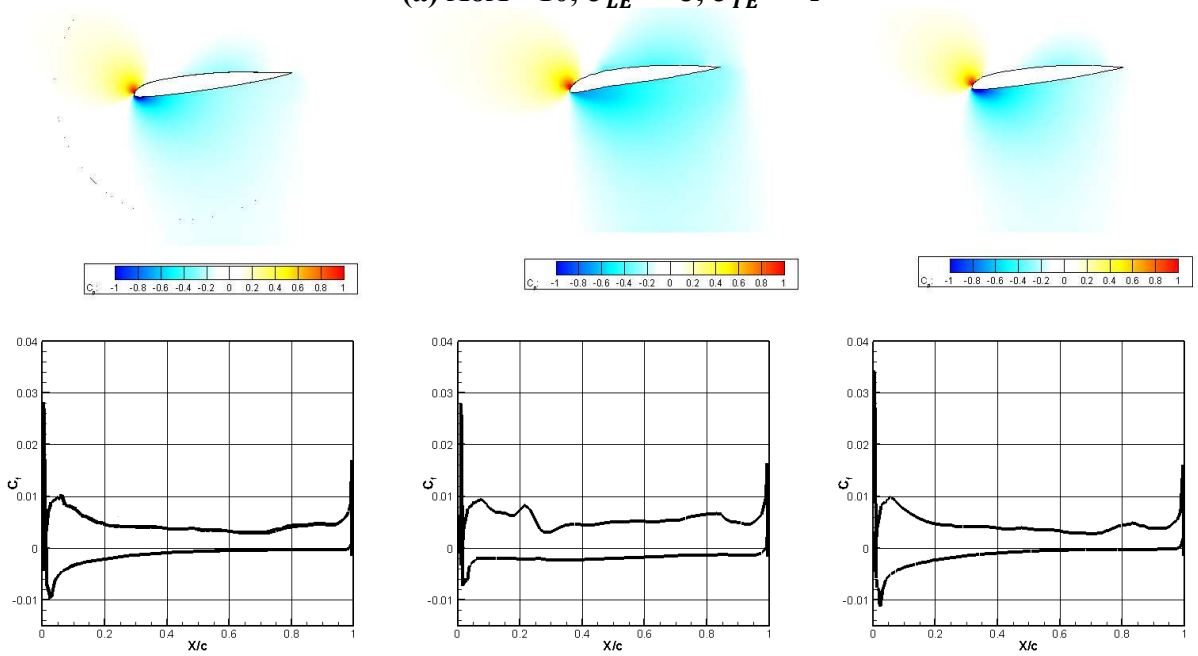
(e) AoA=22, $\theta_{LE} = -6, \theta_{TE} = 0$

Fig. 36. Baseline VR-12 (left) vs Dynamic Morphing (middle) vs Combination (right) upstroke from -10 to 22° coefficeint of pressure (top) and τ_{xy}/Dynamic pressure(bottom) at Re=250,000 (continued)
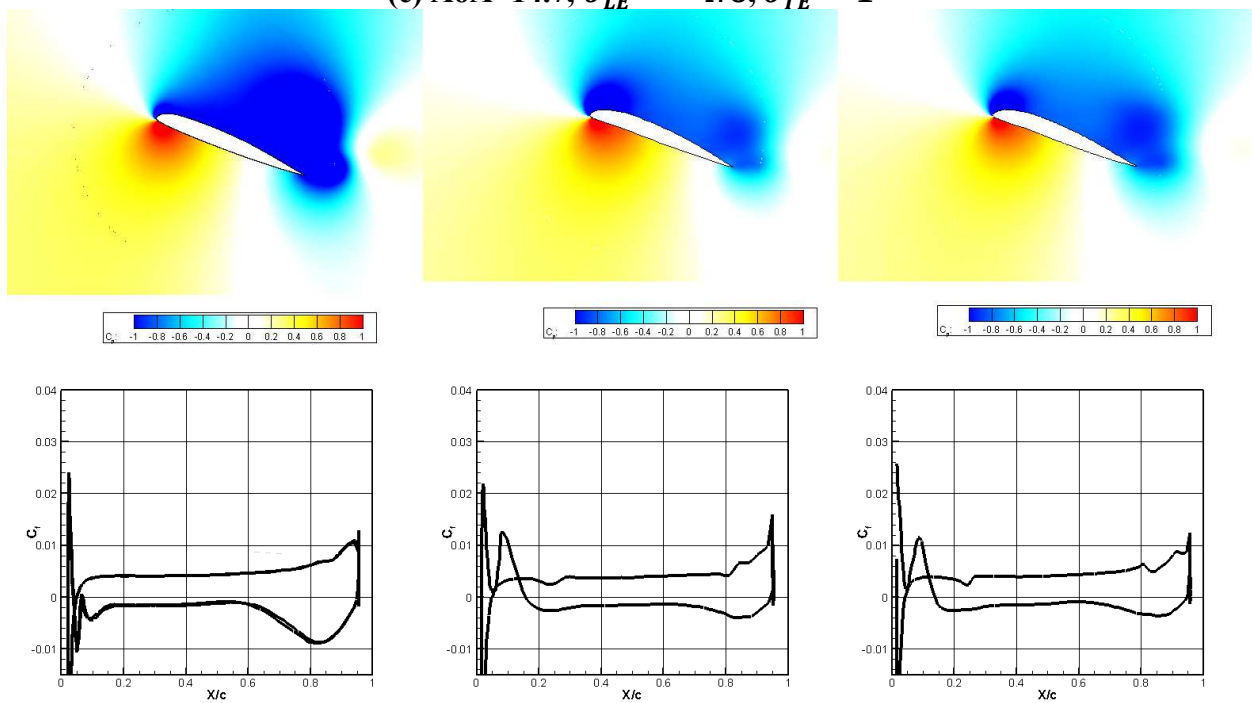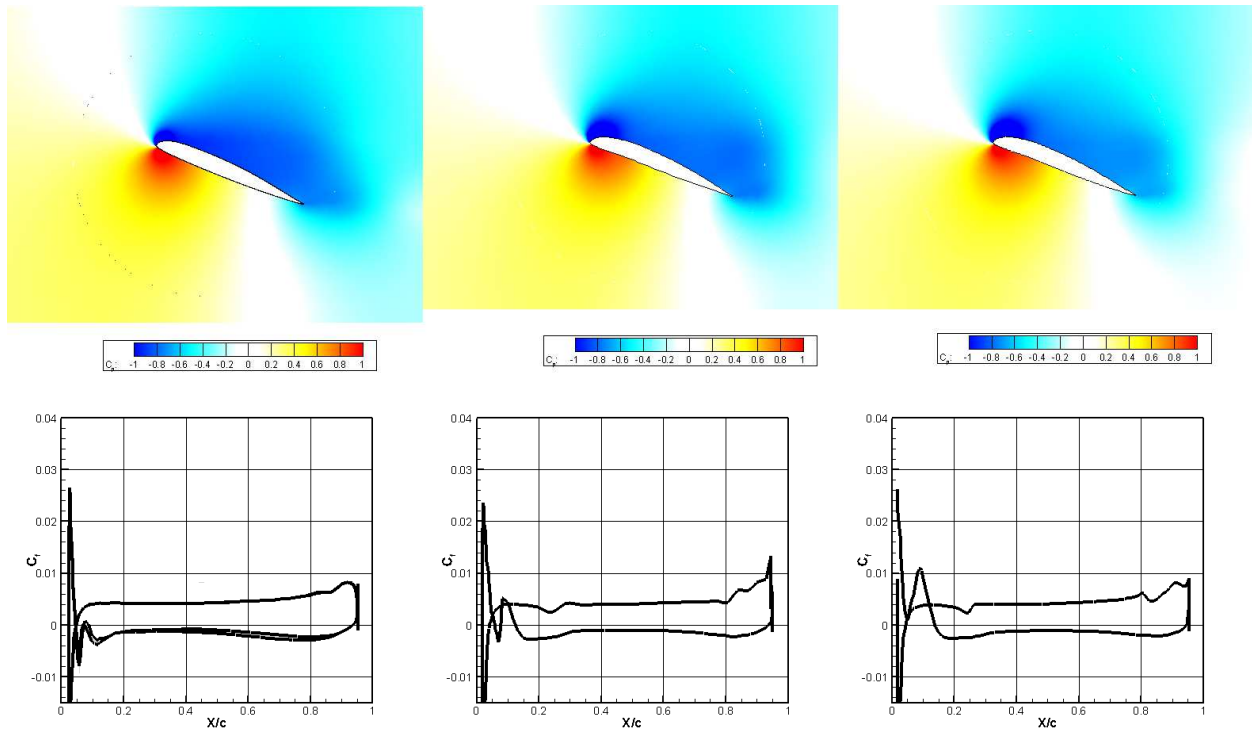
Figures 35 and 36 represent the upstroke of the two aforementioned airfoils from -10 to 22 to°. Figures 35a and 36a shows the comparison between the baseline VR-12 and dynamic morphing airfoil at -10° angle of attack, looking back on figure 34, there is no expected performance from the dynamic morphing airfoil at this low of angle of attack. It isn't until the airfoil begins pitching up that a performance increase is seen in the dynamic morphing case. This is an area that would require further investigation to see what configuration of trailing edge deflection will show performance increase at such low angle of attack. Figures 35b and 36b represent the two airfoils at -7.7° angle of attack pitching up, here there is a slight reduction in in the leading edge separation of the morphing airfoil, resulting in less drag. The dynamic airfoil also shows a slight increase in pressure difference past $X/c=0.4$ that is not seen in the baseline VR-12. Figures 35c and 36c at 14.7° angle of attack, shows that the morphing airfoil has a reduction the size of separation leading to less drag, but it also shows a small reduction in pressure difference near the leading edge, shortly past the leading edge both airfoils maintain very similar pressure differentials. Figures 35d and 36d at 21.3° angle of attack shows that the morphing airfoil delays flow separation from 0.1c to nearly 02.c. The morphing airfoil pressure distribution also shows a much more gradual and smooth distribution when compared to the baseline VR-12. Figure 31e at 22° angle of attack shows near identical results to those discussed for figure 31d.

The static combination airfoil does not show any improvement in performance over the baseline or morphing airfoils. In figure 35d, 36d, 35e, and 36e the combination airfoil pictured on the right of the figure shows very similar if not improved performance when compared to the middle figure of the morphing airfoil. The combination airfoil shows a minor reduction in separation and a very similar pressure differential. The difference between the morphing airfoil

86

and the combination airfoil at these angles of attack is that the combination airfoil has 2.5 degrees of downward trailing edge deflection. This trailing edge deflection could add benefit in the dynamic stall region when compared to the baseline and morphing airfoil. Further refinement of the dynamic morphing regime could easily incorporate the increase in trailing edge deflection at higher angles of attack by increasing its deflection frequency so that the trailing edge is induced at low angles of attack then again at the extreme angles of attack.
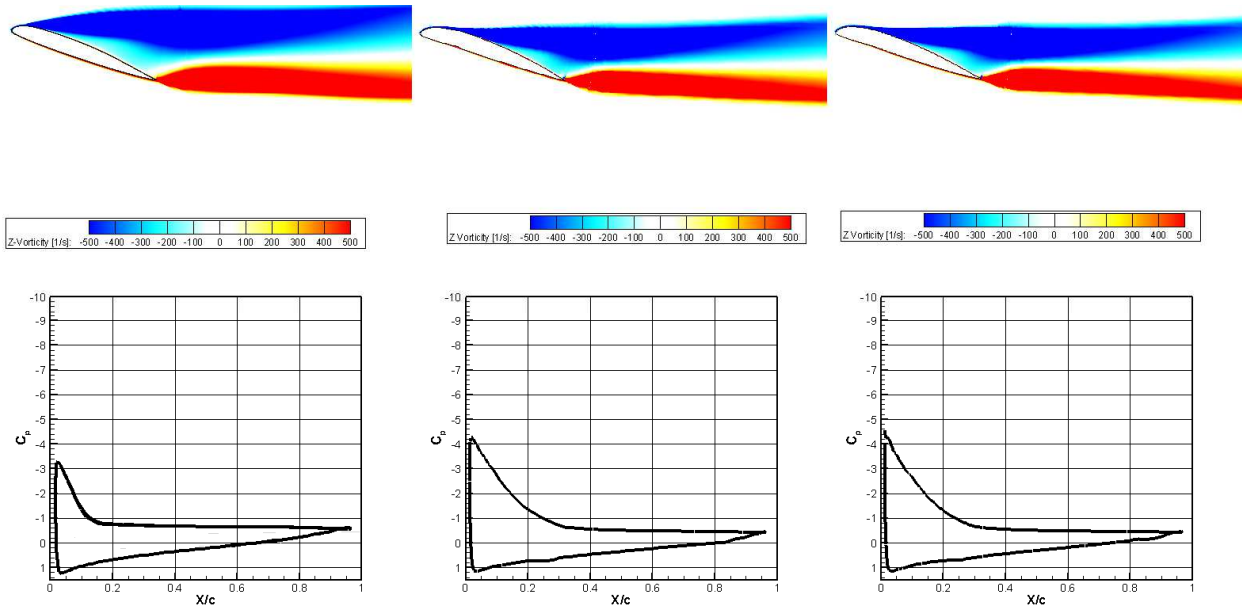
(a) AoA=18.7, $\theta_{LE} = -5.4, \theta_{TE} = 0.4$
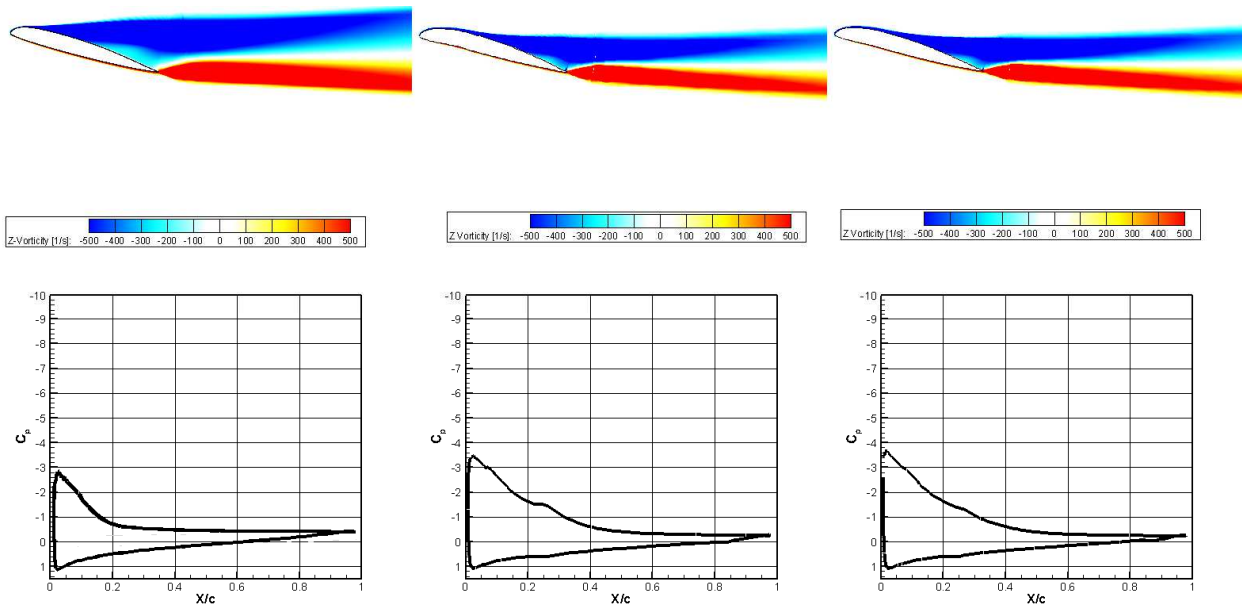
(b) AoA=14.5, $\theta_{LE} = -4.6, \theta_{TE} = 0.9$

Fig. 37. Baseline VR-12 (left) vs Dynamic Morphing (middle) vs Combination (right) downstroke from -10 to 22° vorticity contours (top) and coeffecient of pressure distribution (bottom) at Re=250,000

(c) AoA=12.4, $\theta_{LE} = -4.2, \theta_{TE} = 1.1$

(d) AoA=8.6, $\theta_{LE} = -3.7, \theta_{TE} = 1.7$

Fig. 37. Baseline VR-12 (left) vs Dynamic Morphing (middle) vs Combination (right) downstroke from -10 to 22° vorticity contours (top) and coeffecient of pressure distribution (bottom) at Re=250,000 (continued)

(e) AoA=-4.8, $\theta_{LE} = -1, \theta_{TE} = 3.4$

Fig. 37. Baseline VR-12 (left) vs Dynamic Morphing (middle) vs Combination (right) downstroke from -10 to 22° vorticity contours (top) and coeffecient of pressure distribution (bottom) at Re=250,000 (continued)
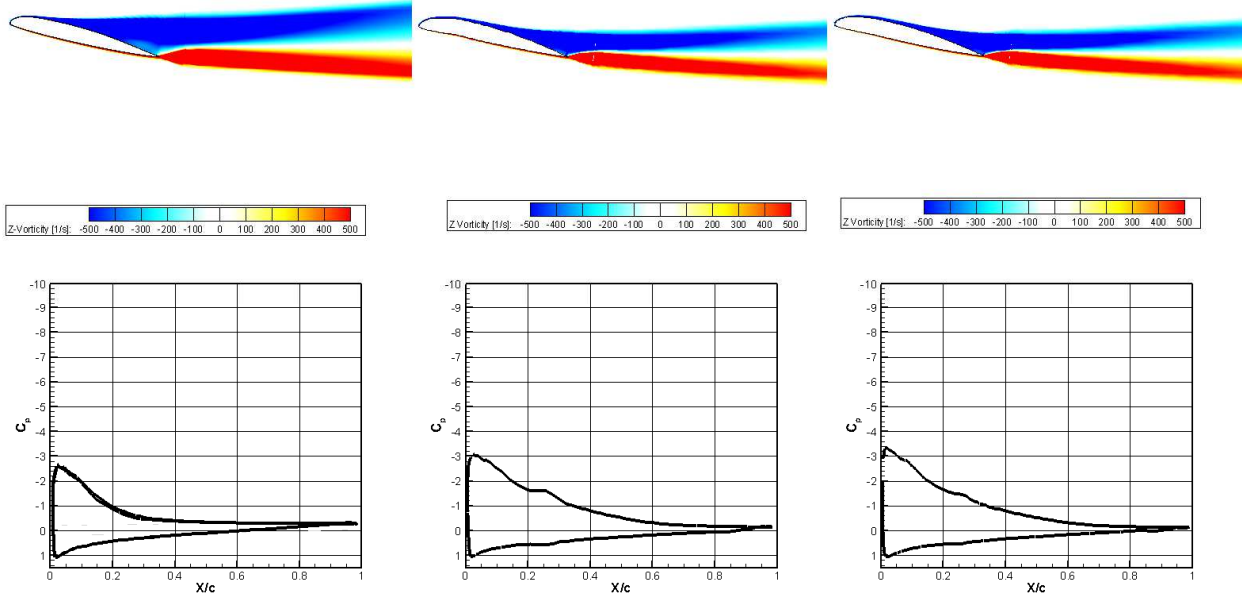
(a) AoA=18.7, $\theta_{LE} = -5.4, \theta_{TE} = 0.4$

(b) AoA=14.5, $\theta_{LE} = -4.6, \theta_{TE} = 0.9$

Fig. 38. Baseline VR-12 (left) vs Dynamic Morphing (middle) vs Combination (right) downstroke from -10 to 22° coefficient of pressure (top) and τ_{xy}/Dynamic pressure (bottom) at Re=250,000
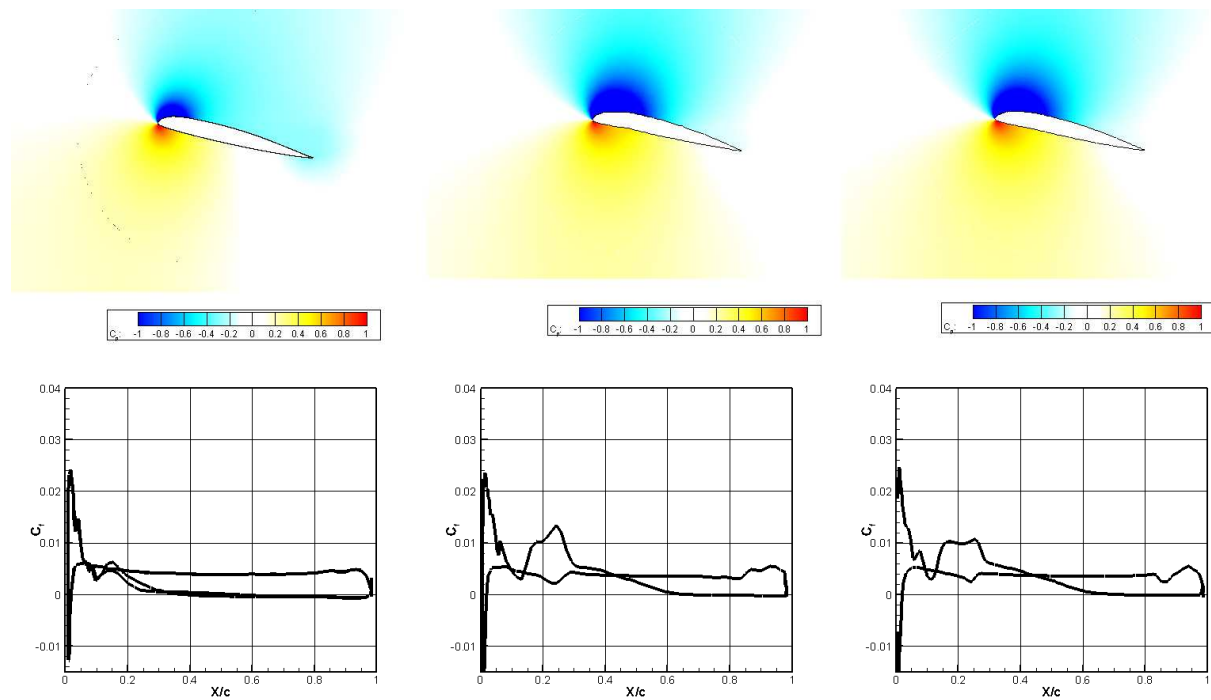
(c) AoA=12.4, $\theta_{LE} = -4.2, \theta_{TE} = 1.1$
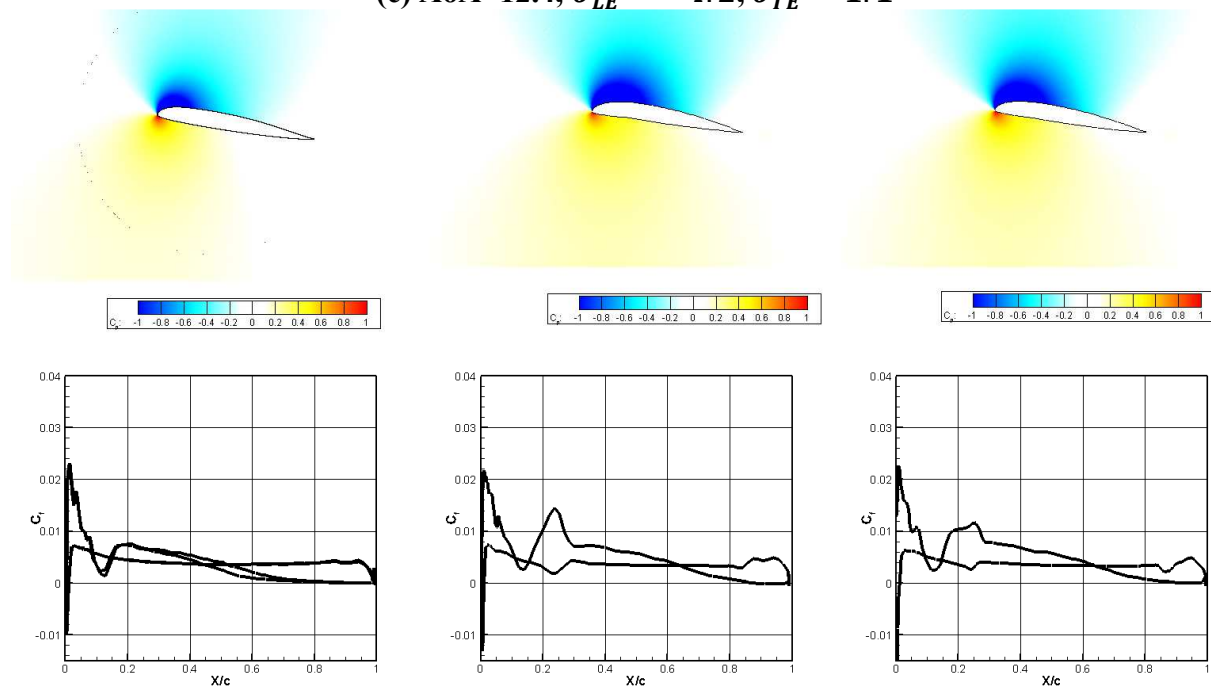
(d) AoA=8.6, $\theta_{LE} = -3.7, \theta_{TE} = 1.7$

Fig. 38. Baseline VR-12 (left) vs Dynamic Morphing (middle) vs Combination (right) downstroke from -10 to 22° coefficeint of pressure (top) and τ_{xy}/Dynamic pressure(bottom) at Re=250,000 (continued)
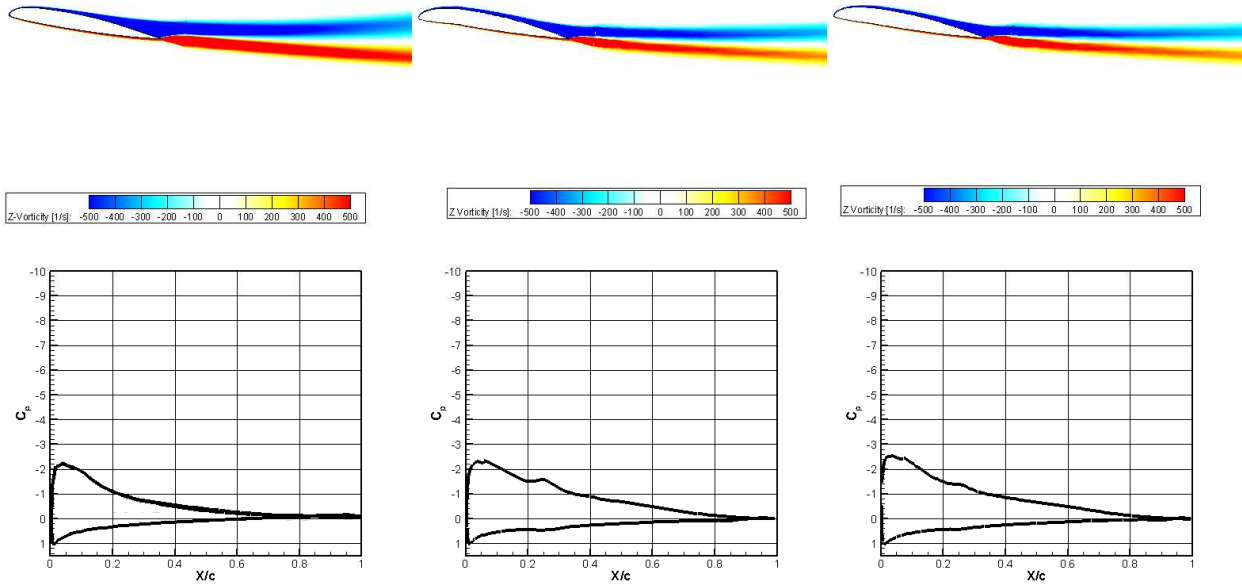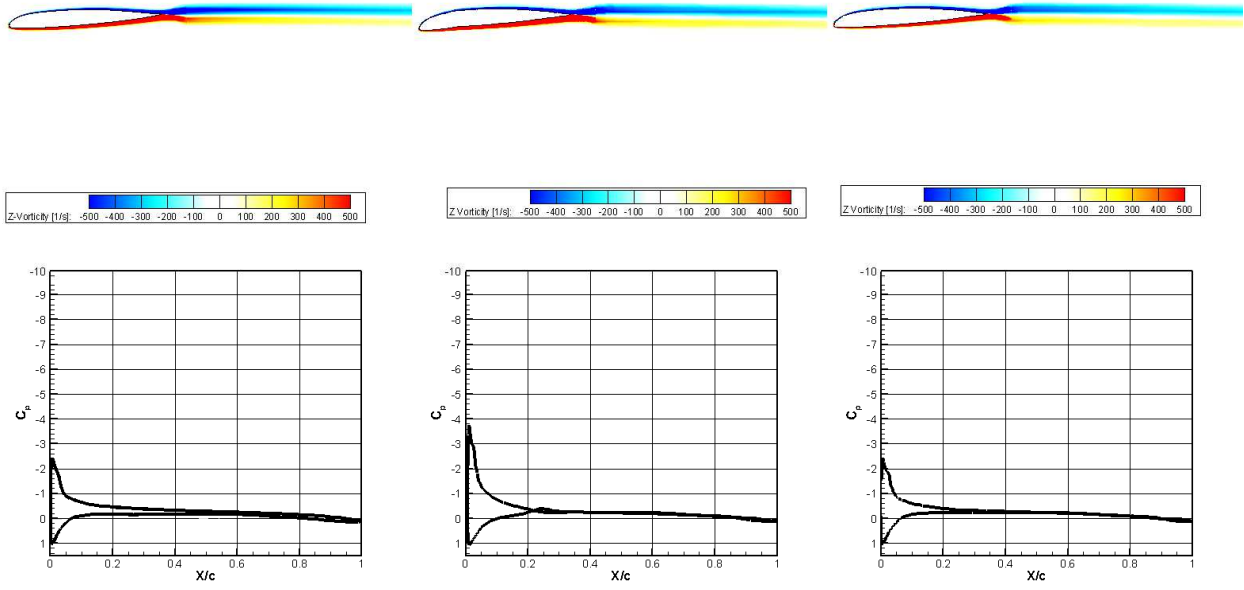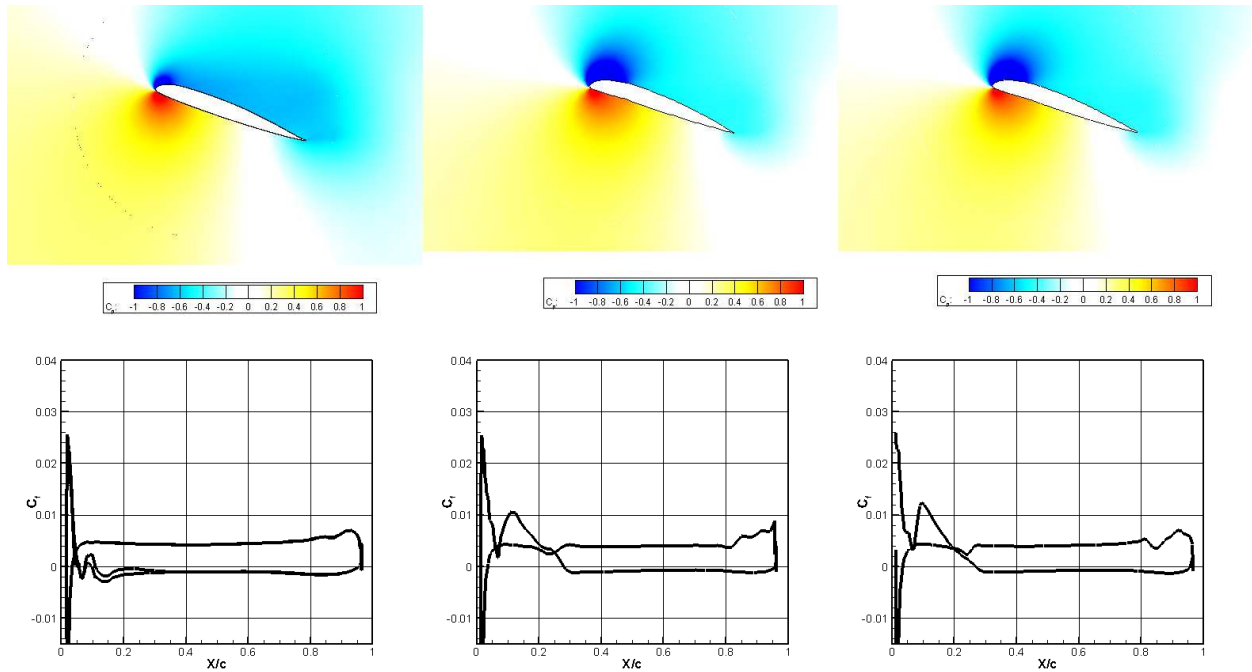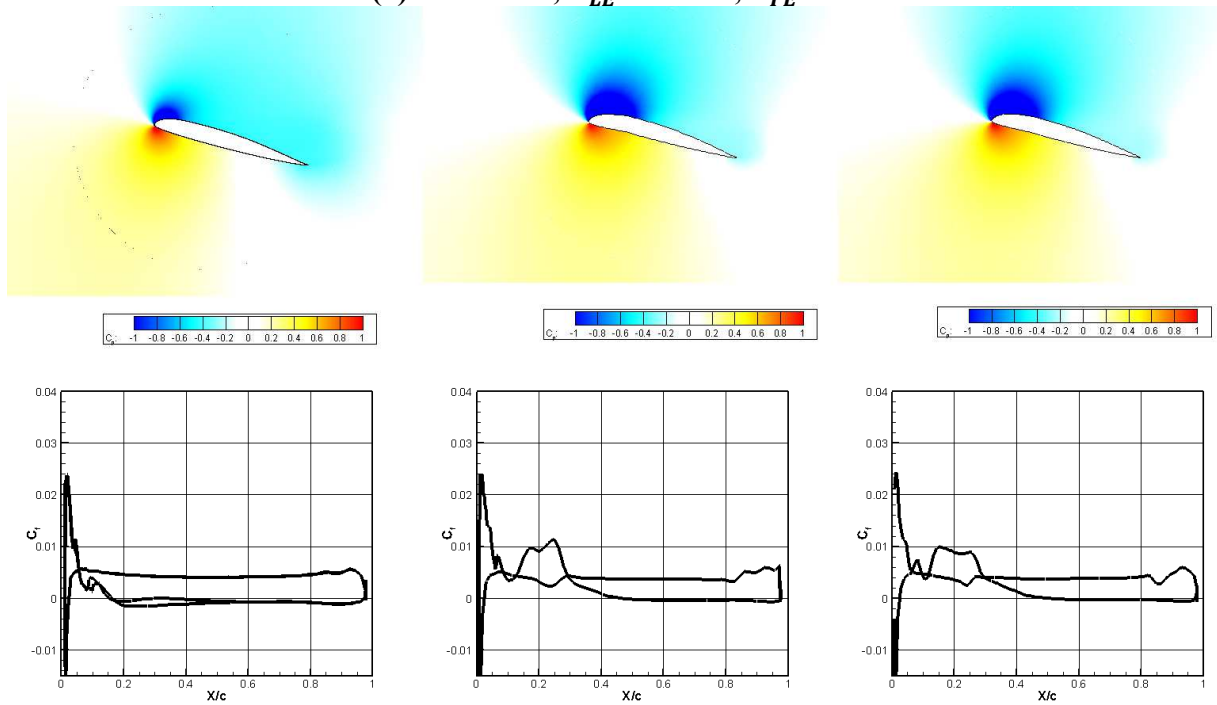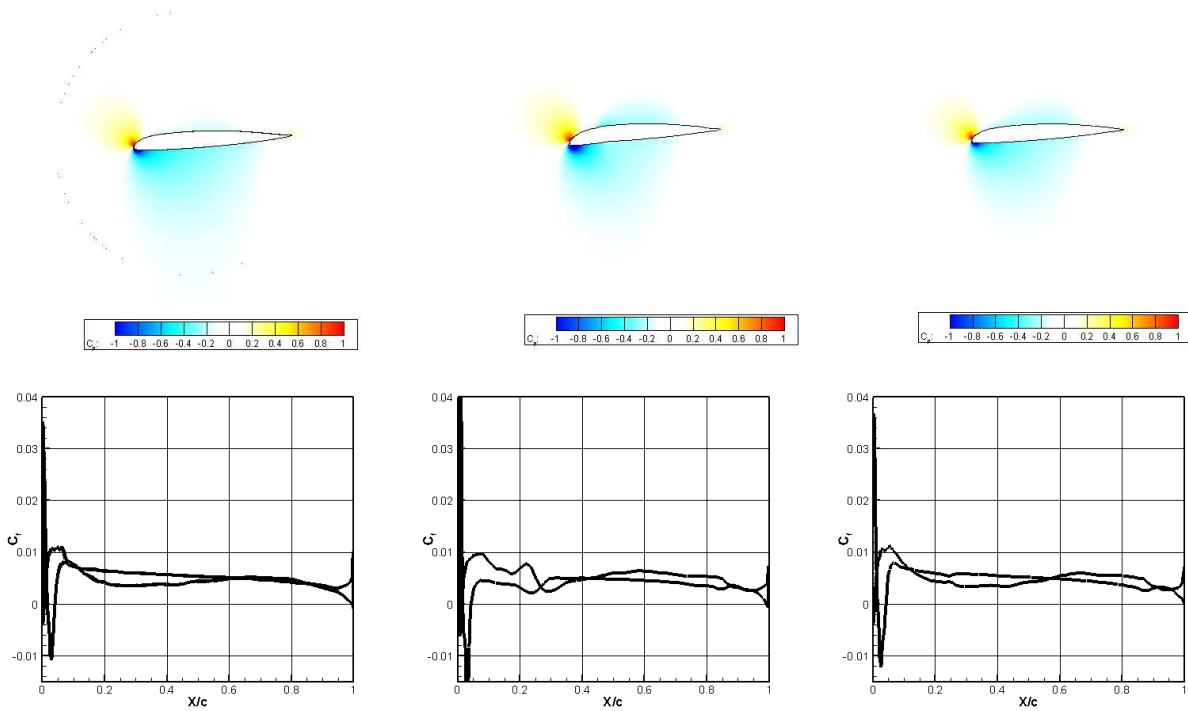
(e) AoA=-4.8, $\theta_{LE} = -1, \theta_{TE} = 3.4$

Fig. 38. Baseline VR-12 (left) vs Dynamic Morphing (middle) vs Combination (right) downstroke from -10 to 22° coefficeint of pressure (top) and τ_{xy}/Dynamic pressure(bottom) at Re=250,000 (continued)

Figures 37 and 38 represent the downstroke from 22 to -10° angle of attack. Figures 37a and 38a show the airfoils at 18.7° angle of attack on the downward stroke. The data shown in figure 34 suggest that the dynamic morphing case recovers from the dynamic stall phenomenon faster than the baseline VR-12, figure 32a also shows evidence that this is true. The morphing airfoil has flow re-attachment near 0.5c whereas the baseline VR-12 only shows flow re-attachment near 0.2c. This results in faster lift recovery as well as a reduction in drag on the airfoil. Figures 37b and 38b at 14.5° angle of attack shows flow re-attachment for the dynamic airfoil near 0.85c for the morphing airfoil and 0.5c for the dynamic airfoil. Again, this results in faster recovery of lift and a reduction in drag for the morphing airfoil. Figures 37c and 38c shows that at 12.4° angle of attack the morphing airfoil reaches near perfect re-attachment of flow,

representative of what was seen on the upstroke. This signifies that the airfoil is out of the dynamic stall phenomenon and performing under normal operation. The baseline VR-12 still shows flow separation near 0.7c suggesting that it is still experiencing the effects of the dynamic stall phenomenon. Figures 37d and 38d at 8.6° shows that the baseline VR-12 is reaching the end of dynamic stall and returning to its normal operation, at this point the morphing airfoil has completely recovered and shows drastically less separation than the baseline VR-12 resulting in overall better performance. Figures 37d and 38d show that at -4.8° angle of attack both airfoils have completely recovered from dynamic stall. This plot also shows that the benefit of the morphing airfoil diminishes as the angle of attack decreases.

The static morphed combination airfoil shows very similar results to the morphing airfoil, even slightly higher pressure differentials in all three cases, further proving that further investigation needs to be done on the effects of a combination of leading and trailing edge deflection during dynamic stall. In figures 37d, 38d, 37e, and 38e the combination airfoil does not show any major improvements over the morphing airfoil.

7.3. SBES Results

The stress blended eddy simulation model or SBES model was utilized to perform high order simulations of the trailing edge 2.5° deflected case. The simulation was performed using a Re=250,000 and range of angle of attack from -2 to 14°. Utilizing the SBES method will allow for better insight into the small-scale structure in the flow field. The results of the SBES simulations are presented using the Q-Criterion ISO surfaces as a way of visualizing the turbulent vortices of the flow. The Q-Criterion is calculated in Tecplot and is representative of the anti-symmetric and symmetric components of the velocity-gradient tensor. (**Tecplot22**) The Q-Criterion is calculated using equation 11.

$$Q = \frac{1}{2}(|\Omega|^2 + |S|^2) \tag{11}$$

Where Ω represents the vorticity magnitude and S represents the strain rate magnitude.

(a) AoA = -2°

(b) AoA = 4°

(c) AoA = 10°

(d) AoA = 12°

Fig. 39. TE2.5 SBES upstroke from -2° to 14° Q-Criterion = 500, colored in spanwise velocity variation at Re=250,000

Figure 39 shows the iso surfaces of Q=500 for the TE2.5 airfoil during its upstroke from -2 to 14°. In figure 39a the airfoil is at -2° and the majority of flow over the upper surface of the airfoil remains laminar, then as the flow approaches the trailing edge of the airfoil the camber of the VR-12 helps to induce a transition of flow from laminar turbulent flow. The last roughly 0.4c can be seen experiencing laminar to turbulent flow transition. Figure 39b shows the airfoil as it begins its upstroke, it can be seen that as the airfoil begins pitching upwards the transition region begins to grow over the mid chord of the airfoil and the turbulent region begins to grow further up the airfoil closer to the leading edge. Figure 39c shows the airfoil at 10° angle of attack. At

this higher angle it can be seen that the turbulent region has moved up the chord to the leading edge, but flow remains mostly attached to the upper surface. Lastly, figure 34d shows the airfoil at its max of 14° angle of attack, it can be seen that the flow has settled near the leading edge of the airfoil into a laminar region with large vortical structure seen near the trailing edge and clear separation of flow.

(a) AoA = 12°

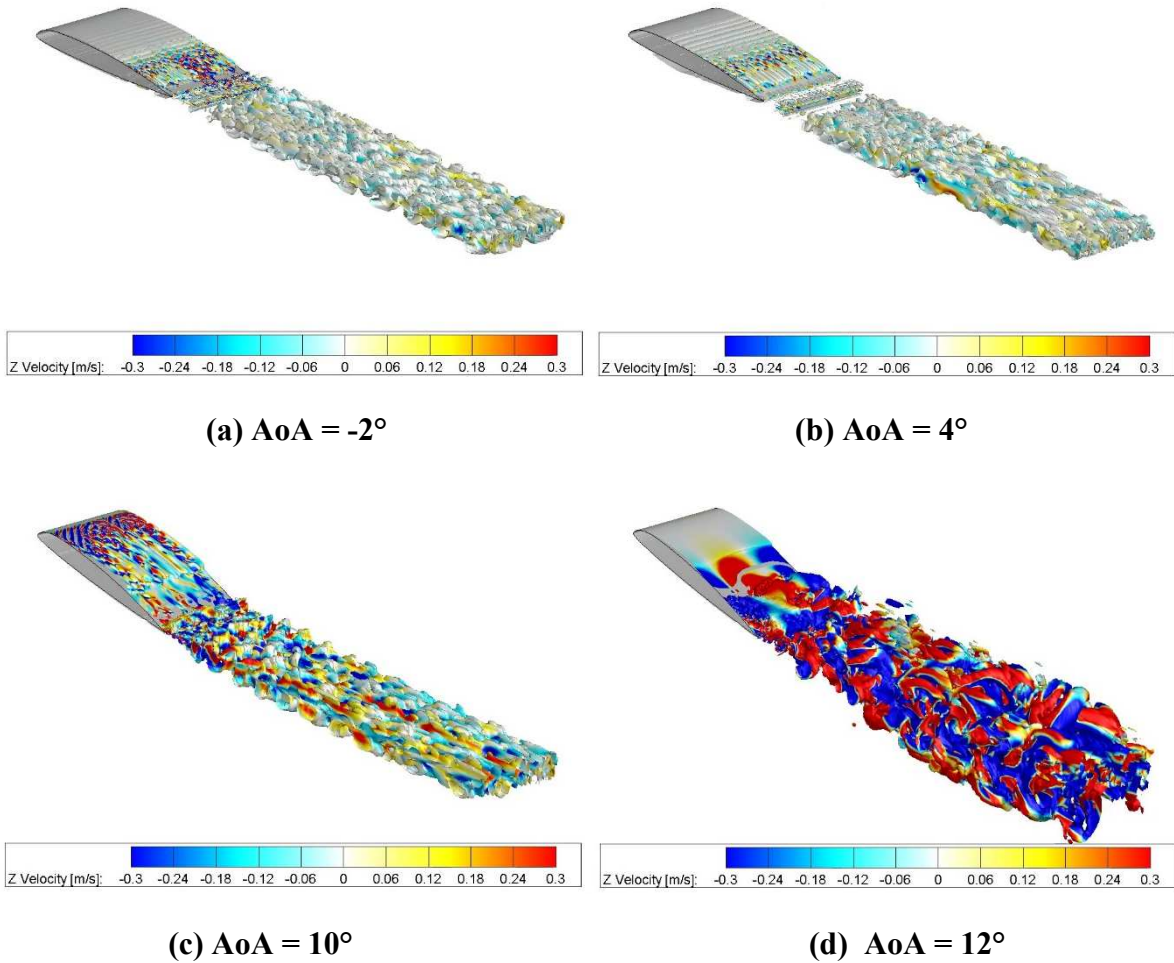(b) AoA = 10°

(c) AoA = 4°

(d) AoA = -2°
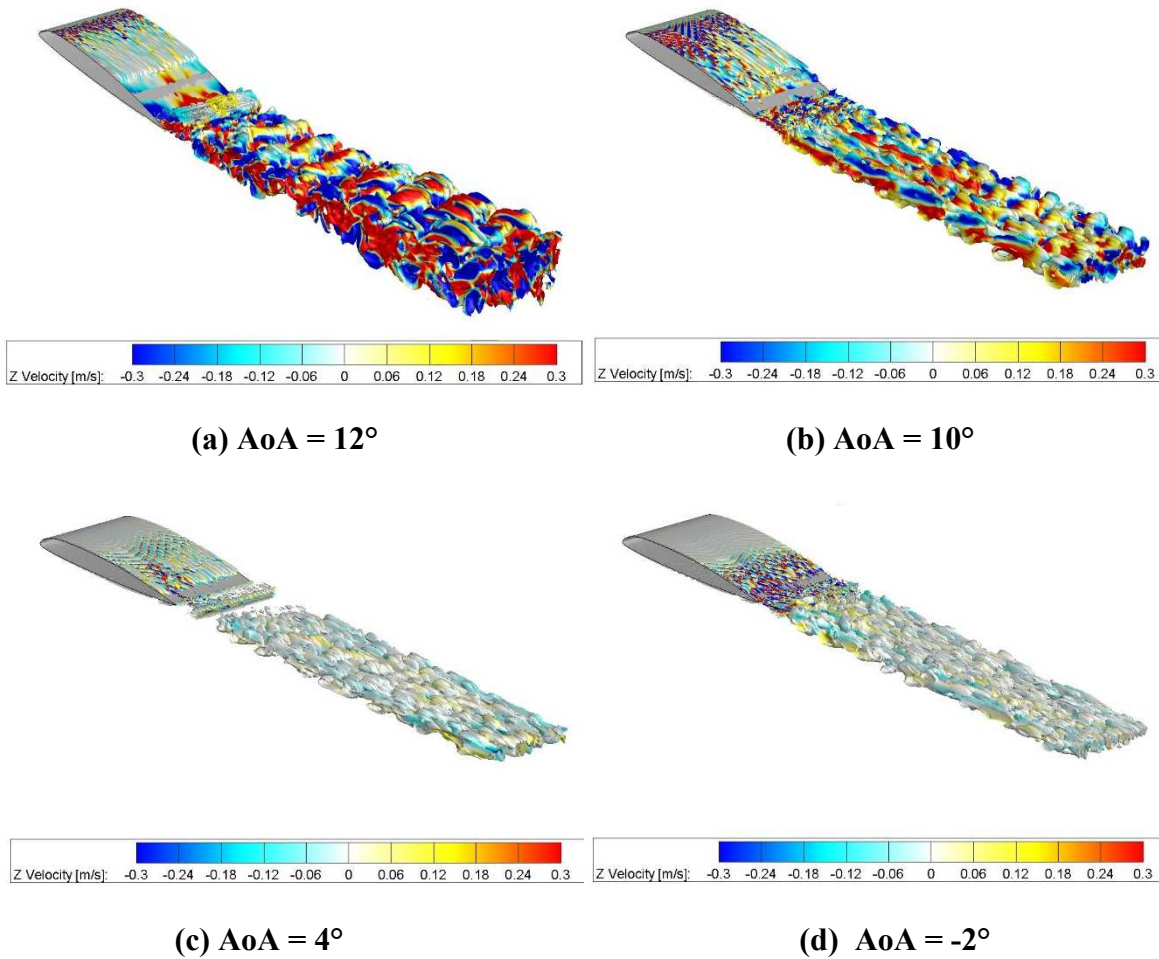
Fig. 40. TE2.5 SBES downstroke from 14° to -2° Q-Criterion = 500, colored in spanwise velocity variation at Re=250,000

Figure 40 shows the iso surfaces of Q=500 for the TE2.5 airfoil during its downstroke from 14 to -2°. Figure 40a shows the beginning of the downstroke where the turbulent flow has moved back up the chord of the airfoil approaching the leading edge and the amount of vortical

structure shedding from the trailing edge begins to diminish. Figure 40b shows a large reduction in vortical shedding from the trailing edge and the turbulent region beginning to recede from the leading edge as the airfoil approaches lower angles of attack. Figure 40c shows the turbulent region approaching its starting point near the trailing edge of the airfoil with the majority of the flow near the leading edge remaining laminar. Lastly, figure 40d shows the airfoil as it reaches its initial starting point of -2° angle of attack where the majority of the airfoil is covered in a laminar sheet and the turbulent flow near the trailing edge leads to small vortical shedding.

Fig. 41. Computed coefficient of lift, drag, and lift over drag vs AoA at Re=250,000, C_l (left), C_d (middle), C_l/C_d (right)

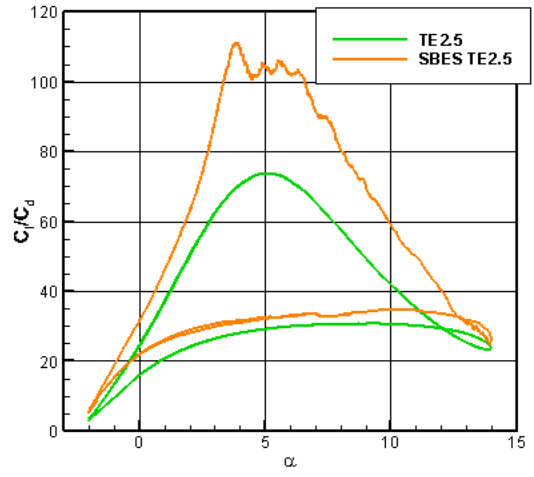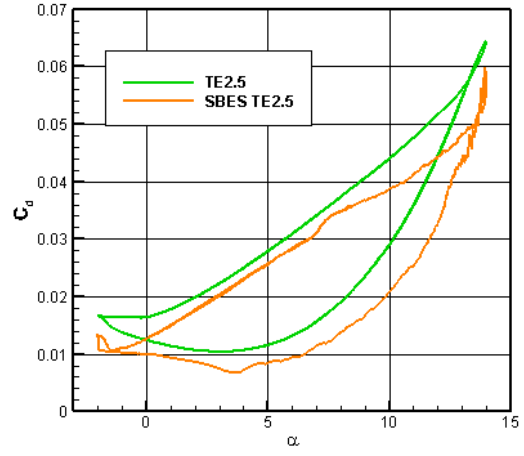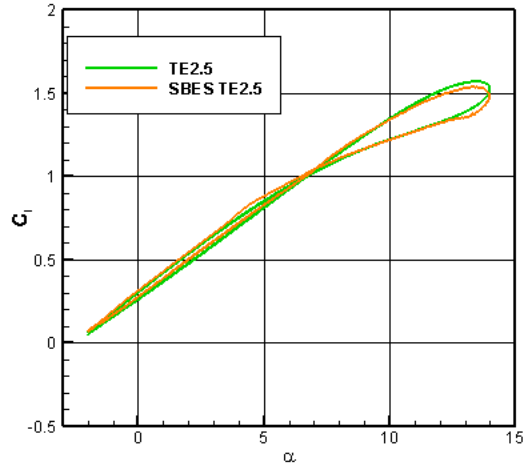Figure 41 shows the computed coefficients of lift and drag for the trailing edge deflection of 2.5° when pitching from -2° to 14° ° comparing the SBES model to the RANS model. The first plot of coefficient of lift shows that the SBES and RANS overall show very similar results with only minor differences near the max angle of attack of 14°, where it can be seen that the SBES model begins to show a minor reduction in C_l as well as some minor fluctuation most likely due to the lack of averaging and smoothing present in the SBES model. This will be more prevalent in the drag calculations discussed next.

The second plot shows the coefficient of drag, here it can be seen that the SBES and RANS models shows a similar shape, except that the SBES model shows consistently less drag over the entire hysteresis curve. Along with the reduction in drag there is also oscillations or instabilities in the drag values near its max and min angles of attack. This is most likely due to the lack of averaging and smoothing that would be seen in URANS calculations. This is seen in better detail in the next plot of coefficient of lift over drag.

The last plot showing the coefficient of lift over drag shows a larger value over the entire hysteresis curve with some unsteadiness seen as the airfoil approaches the max angle of attack and partially in the down stroke. When the airfoil is at the lower and median angles of attack the data appears very smooth similar to the results of the URANS tests. Overall, the SBES case shows a more accurate prediction of what is occurring to the lift and drag created by the airfoil especially near its max and min angles of attack.
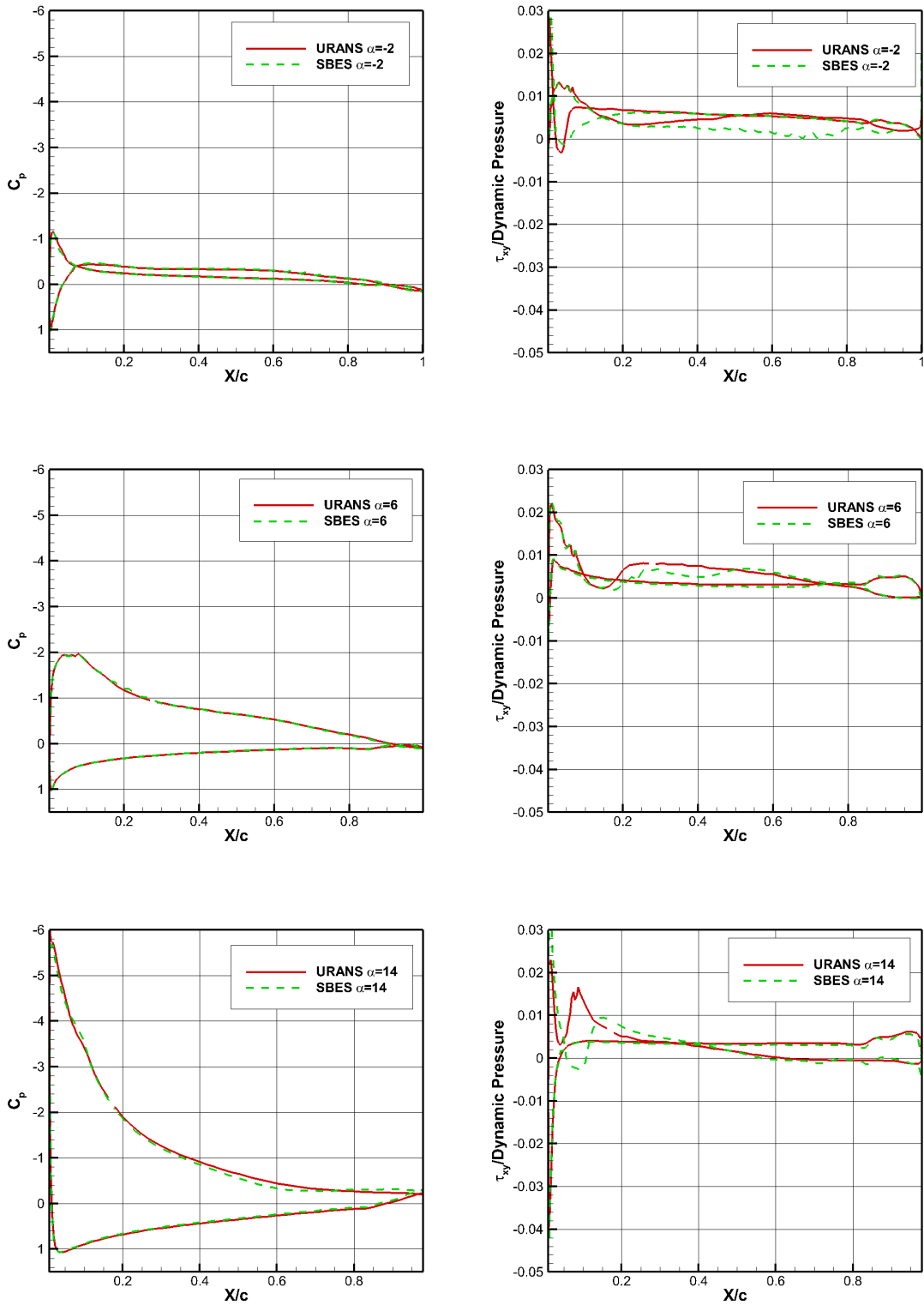
Fig. 42. SBES vs URANS comparison of computed coefficient of pressure and τ_{xy}/Pressure at Re=250,000

When looking at the comparison of coefficient of pressure between the SBES case and the URANS case above in figure 42 the URANS case is presented in solid red and the SBES case is presented in dashed green. The SBES and URANS case show very good aggreement when comparing the coefficient of pressure at all thee angles of attack. The coefficient of pressure curve follows its normal trend of increasing pressure differential as the the angle of attack increases. When looking at the value of τ_{xy}/Pressure the SBES and URANS case don't show the exact same trends. This corresponds to the lift and drag curve, where the lift values are very similar but there is more discrepency in the drag calculations, where drag is more dependent on the shear force on the airfoil. At -2 degrees angle of attack the SBES case shows less shear force along the pressure surface when compared to the URANS case. At 6 degrees the SBES case shows slightly less shear force from X/c=0.2 to 0.5 then agrees very well with the URANS case. Lastly, at 14 degrees angle of attack the SBES case predicts the laminar seperation bubble near the leading edge which is not present in the URANS results. Then, near the trailing edge the SBES case and URANS case show very good agreement both showing the sepearation point at X/c=0.6 and show no flow re-attatchment after that point.

8. CONCLUSIONS AND FUTURE WORK

8.1. Conclusions

Using the 2D XFLR5 and 2D & 3D ANSYS-Fluent to simulate different static deflections applied to the VR-12 airfoil proved to be successful in rapidly testing optimal shape changes to utilize as a starting point for further advancement.

Then using the static shape deflections and introducing a sinusoidal pitching motion using a 3D ANSYS-Fluent simulations allowed for the different shape changes to be analyzed in a pitching regime to represent the pitching motion of a rotorcraft more closely. The results of 3D URANS simulations showed that static LE deflection of 6° performed the best at the max angle of attack and the TE deflection of 4° performed the best at the minimum angle of attack and in between the minimum and a combination of both was optimal at intermediate angles of attack.

This data was then used as the starting point for the dynamic morphing and pitching case. Using ANSYS-Fluent and its ability to mesh morphing using UDFs an initial morphing regime was developed based on the results of the static deflection pitching cases. While not optimal the results of these dynamic morphing cases proved that the dynamic airfoil would outperform the baseline VR-12.

Further analysis of the morphing airfoil in the dynamic stall phenomenon was performed. The dynamic stall phenomenon was not completely avoided, but the behavior was changed drastically. The morphing airfoil started to stall roughly 1 degree sooner than the baseline. Once the morphing airfoil entered the dynamic stall the coefficient of lift stayed above 1.2 until it recovered at an angle of attack of 10 degrees, while the baseline airfoil consistently dropped until a coefficient of lift of 0.7 and recovered near 6 degrees. The morphing airfoil application can be

used in order to reduce the effects of dynamic stall most notable reduce the time to recovery of lift.

Initial simulations of static deflections utilizing the hybrid SBES turbulence model were prepared and the TE2.5 static deflection pitching from -2 to 14° case was run. The simulations utilizing the SBES model allow for more fine detail in the flow field. This level of detail in the flow field will create the opportunity to see specifically how the different deflections will affect the flow field on a much smaller scale. This gives the ability to directly locate the regions of laminar, transitional, and turbulent flow. This level of detail will create the opportunity to analyze the different airfoil shapes in a much more in depth manner in order to provide further optimization.

8.2. Future Work

Future work will include further development of a method to test different frequencies of oscillation for the leading and trailing edge deflections in the dynamic morphing regime, in order to optimize the airfoil for specific applications.

 The collection of a large set of data for different oscillation frequencies will allow for the use of a machine learning algorithm to sort through the data using regression and optimization algorithms to find what oscillation frequencies are going to provide the greatest improvement to the target variable like C_l/C_d, C_l, or C_d.

The running of all URANS cases with the hybrid SBES turbulence model in order to compare with experimental results. This will allow for a deeper understanding of the effects of morphing in the flow field and can lead to further development and optimization of the morphing regime.

REFERENCES

[1]   Weisshaar, T. A., "Morphing Aircraft Systems: Historical Perspectives and Future Challenges," *Journal of Aircraft,* 2013, pp. 337-353. https://doi.org/10.2514/1.C031456

[2]   Murat, A., Guleren, K. M.," "A Short Brief on the Aircraft History and Anatomy," Sustainable Aviation. Springer International Publishing, Germany, 2019.

[3]   W. Refling, T. Sprengeler, Y. B. Suzen, and J. Estevadeordal, "Experimental Investigation of Morphing Flow Control for Unsteady Aerodynamic Applications," Submitted to AIAA SciTech 2022. https://doi.org/10.2514/3.12149

[4]   Wang, S., Tomovic, M., and Liu, H., "Commercial aircraft hydraulic systems: Shanghai Jiao Tong University Press aerospace series," Academic Press, Massachusetts, 2016.

[5]   Young, A. D., "The aerodynamic characteristics of flaps," *Aeronautical Research Council Reports & Memoranda*, 1947.

[6]   Poling, D. R., Dadone, L., and Telionis, D. P., "Telionis Blade-vortex interaction." *AIAA Journal* 1989 Vol. 27, No. 6, 1989, pp. 694-699. https://doi.org/10.2514/3.10167

[7]   Costes, M., Renaud, T., and Rodriguez, B., "Rotorcraft simulations: a challenge for CFD," *International Journal of Computational Fluid Dynamics* 2012, Vol. 26.6, No. 8, 2012, pp. 383-405. https://doi.org/10.1080/10618562.2012.726710

[8]   Fincham, J. H. S., and Friswell, M. I., "Aerodynamic optimisation of a camber morphing aerofoil." *Aerospace Science and technology,* Vol 43, 2019, pp. 245-255. https://doi.org/10.1016/j.ast.2015.02.023

[9]   Yee, K., Joo, W., and Lee, DH. "Aerodynamic performance analysis of a Gurney flap for rotorcraft application." *Journal of Aircraft,* Vol, 44, 2007, pp. 1003-   1014. https://doi.org/10.2514/1.26868

[10]   Martin, P. B., McAlister, K. W., Chandrasekhara, M. S., and Geibler, W., "Dynamic stall measurements and computations for a VR-12 airfoil with a variable droop leading edge," *American Helicopter Society 59th Annual Forum,* 2003.

[11]   Glaz, B., Friedmann, P. P., and Liu, L., "Vibration reduction and performance enhancement of helicopter rotors using an active/passive approach," *49th AIAA/ASME/ASCE/AHS/ASC Structures, Structural Dynamics, and Materials Conference,* 2008. 10.2514/6.2008-2178

[12]   Maughmer, M. D., and Bramesfeld, G., "Experimental investigation of Gurney flaps," *Journal of Aircraft,* Vol. 45, No. 6, 2008. https://doi.org/10.2514/1.37050

[13]   Khoshlahjeh, M., and Gandhi, F., "Extendable chord rotors for helicopter envelope expansion and performance improvement," *Journal of the American Helicopter Society* Vol. 59 No. 1, 2014, pp. 1-10. https://doi.org/10.4050/JAHS.59.012007

[14]   Marouf, A., Tekap, Y. B., Simiriotis, N., To, JB., Rouchon, JF., Hoarau, Y., and Braza, M., "Numerical investigation of frequency-amplitude effects of   dynamic morphing for a high-lift configuration at high Reynolds number," *International Journal of Numerical Methods for Heat & Fluid Flow,* Vol. 31, No. 2, 2020, pp. 599-617. https://doi.org/10.1108/HFF-07-2019-0559

[15]   Abdessemed, C., Yao, Y., Abdessalem, B., Narayan, P., "Aerodynamic analysis of a harmonically morphing flap using a hybrid turbulence model and dynamic meshing," *Applied Aerodynamics COnfrence2018 applied aerodynamics conference.* 2018. https://doi.org/10.2514/6.2018-3813

[16]   Mishra, A., Ananthan, S., and Baeder, J., "Coupled CFD/CSD prediction of the effects of trailing edge flaps on rotorcraft dynamic stall alleviation," *47th AIAA aerospace sciences meeting including the new horizons forum and aerospace exposition*, 2009. https://doi.org/10.2514/6.2009-891

[17]   Menter, F. "Stress-blended eddy simulation (SBES)—A new paradigm in hybrid RANS-LES modeling" *Symposium on Hybrid RANS-LES methods*. Springer, Cham, 2016. https://doi.org/10.1007/978-3-319-70031-1_3

[18]   Menter, F., Huppe, A., Matyushenko, A., and Kolmogrov, D., "An overview of hybrid RANS–LES models developed for industrial CFD," *Applied Sciences,* Vol. 11, No. 6, 2021, pp. 2459. https://doi.org/10.4050/JAHS.59.012007

[19]   "XFLR5 Potential Flow Solver," [online] Available: http://www.xflr5.tech/xflr5.htm. [Accessed 15 August 2020].

[20]   G. Goecks, Vinicius, Camara Leal, Pedro, White, Trent, Valasek, John, Hartl, Darren, "Control of Morphing Wing Shapes with Deep Reinforcement Learning," *2018 AIAA Information Systems-AIAA Infotech @ Aerospace,* 2018. https://doi.org/10.2514/6.2018-2139

[21]   P. Plantim De Hugues, K. W. McAlister, and C. Tung, "Effect of an Extendable Slat on the Stall Behavior of a VR-12 Airfoil," *NASA Technical Paper* 3407, 1993.

[22]   Qing Wang, Qijun Zhao, "Rotor aerodynamic shape design for improving performance of an unmanned helicopter," *Aerospace Science and Technology*, Vol. 87, 2019, pg. 478-487. https://doi.org/10.1016/j.ast.2019.03.006

[23]   P. Martin and K. Mcalister and M. Chandrasekhara and W. Geissler, "Dynamic Stall Measurements and Computations for a VR-12 Airfoil with a Variable Droop Leading Edge," *American Helicopter 59th Annual Forum, Phoenix, Arizona, May 6 – 8*, 2003.

[24]   "Ansys CFX | Industry-leading CFD Software" [online] Available: https://www.ansys.com/products/fluids/ansys-cfx. [Accessed 1 June 2021].

[25]   Menter, F. R., "Two-Equation Eddy-Viscosity Turbulence Models for Engineering Applications," *AIAA Journal*, Vol. 32, No. 8, August 1994, pp. 1598-1605.

[26] Menter, F. R., Langtry, R. B., Likki, S. R., Suzen, Y. B., Huang, P. G., and Völker, S. "A Correlation-Based Transition Model Using Local Variables—Part I: Model Formulation." ASME. *J. Turbomach*. July 2006; 128(3): 413–422. https://doi.org/10.1115/1.2184352

[27] Langtry, R. B., Menter, F. R., Likki, S. R., Suzen, Y. B., Huang, P. G., and Völker, S. "A Correlation-Based Transition Model Using Local Variables—Part II: Test Cases and Industrial Applications." ASME. *J. Turbomach*. July 2006; 128(3): 423–434. https://doi.org/10.1115/1.2184353

[28] "Introduction to ANSYS ICEM CFD | Ansys Training" [online] Available: https://www.ansys.com/training-center/course-catalog/fluids/introduction-to-ansys-icem-cfd. [Accessed June 1, 2021].

[29] Alam Mohammad, Suzen, Y., Ol, Michael, "Numerical Simulations of Pitching Airfoil Flow Fields for MAV Applications," AIAA-2009-4029, 39th AIAA Fluid Dynamics Conference, 22-25 June 2009, San Antonio, Texas.

[30] "Tecplot 360 User's Manual" [online] Available: https://tecplot.azureedge.net/products/360/current/360_users_manual.pdf [Accessed 9 May 2022].

APPENDIX A. FLUENT SET UP

General

- Solver Type: **Pressure-Based**
- Solver Velocity Formulation: **Absolute**
- Solver Time: **Transient**

Models

- Viscous: **Transition SST (4 eqn)**
- All others: **Off**

Cell Zones

- Type: **Fluid**
- Material: **Air**

Boundary Conditions

- Outlet: **Pressure-Outlet**
- Top, Bottom, Upper, Lower: **No-slip Wall**
- Inlet: **Velocity-Inlet**
  - o Specification Method: **Intermittency, K and Omega**
- Sym1, Sym2: **Symmetry**

Mesh Interfaces

- New Interface → Auto create → Select the two interfaces (Automatically creates fluid-interface)

Methods

- Scheme: **Pressure**
- Spatial Discretization: **Set all to Second Order**
- Transient Formulation: **Second Order**

Report Definition

- New → Force Report → Lift
- New → Force Report → Drag

Initialization

- Methods: **Hybrid Initialization**

Solving Tab→ Advanced

- Time Step Size (s): **0.0007 for URANS and 0.000075 for SBES**
- No. of Time Steps: **Set accordingly**
- Max Iterations/Time Step: **20**

Solving Tab→ Residuals

- Set all residuals to: **1e-06**

Rotate Airfoil to Propper Starting Angle of Attack

- Cell Zone Conditions → Right click and deactivate the outer domain → Setting Up Domain Tab → Transform → Rotate → Set rotation angle CCW-Positive CW-Negative → Cell Zone Conditions → Right click and activate the outer domain

Initializing

- Solving Tab → Initialize → Autosave→ Set Save Data File Every (Time Steps) Accordingly → Data File Quantities to add additional variables to output list

Saving Case and Data Files

- File → Write → "Case & Data"

APPENDIX B. FLUENT SETUP WITH UDF

Open Fluent via Microsoft VS Compiler

- Start → Type "**x86_x64 Cross Tools Command Prompt for VS 2019**" → Open

x86_x64 Cross Tools Command Prompt for VS 2019

- In the command prompt window type "**cd..**" until you reach "**C:\\>**"
- Then Type "**cd program files**" → "**cd ansys inc**" → "**cd v182**" → "**cd fluent**" → "**cd ntbin**" → "**cd win64**" → Then type "**fluent**" and fluent will open with the Microsoft VS Compiler

Loading the previously set up Case and Data Files

- File → Read → Case & Data → Select the previously set up Case & Data file

UDF Loading

- User Defined → Functions → Compiled → Add → Select your UDF → Type new library name → Build → Load

Pitching

- Cell Zone Conditions → Right click the moving zone (inner zone) → Check Mesh Motion → Select Mesh Motion tab → Rotational Velocity → Drop menu → Select "udf Pitching"

Dynamic Mesh

- Open Dynamic Mesh → Select "Remeshing" and "Smoothing" → Settings → Set diffusion parameter to "1.5"
- Create Edit → Type: User Defined → Select "Upper" airfoil boundary → Open Mesh Motion UDF Drop Down Menu: Up::libudf### → Select Create
- Repeat for "Lower" airfoil boundary condition

APPENDIX C. SUBMITTING FLUENT JOB TO CCAST

Required Files

- Fluent Case File (.cas)
- Fluent Data File (.dat)
- UDF File (.c)
- UDF Library Folder (libudf###)
- Journal File (.jou)
- PBS Script (.pbs)

PBS Script
```
#!/bin/bash
#PBS -q preemptible
#PBS -N pitching_vr12
#PBS -j oe
#PBS -l select=5:mem=42GB:ncpus=20:mpiprocs=20
#PBS -l walltime=50:00:00
#PBS -m abe
#PBS -M first.last@ndsu.edu
#PBS -W group_list=x-ccast-prj-suzen
#

# change to directory from which job was submitted
cd $PBS_O_WORKDIR
# (list of node names is in file $PBS_NODEFILE)
nprocs=`wc -l $PBS_NODEFILE | awk '{ print $1 }'`
# specifies the version of ANSYS FLUENT to run
version=3ddp
# load ansys module so that we find the fluent command
module load ansys/v182
# fluent commands are in file Fluent_par.jou, output messages go to output_file
fluent $version -t$nprocs -cnf=$PBS_NODEFILE -g -i Transient_UDF.jou > output_file
```

Journal File
```
/file/read-case-data name_of_case_and_data_file
/file/autosave/data-frequency 5
/solve/set/time-step 0.0007
/solve/dual-time-iterate 14250 20
/exit
yes
```

APPENDIX D. SURFACE PRESSURE DATA
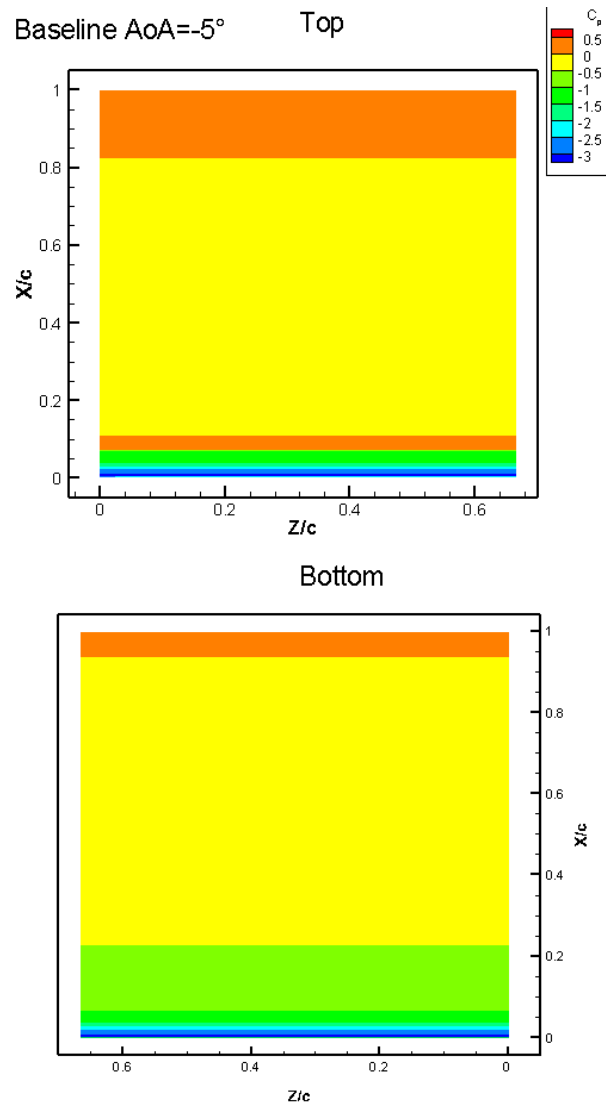
(a) -5° AoA

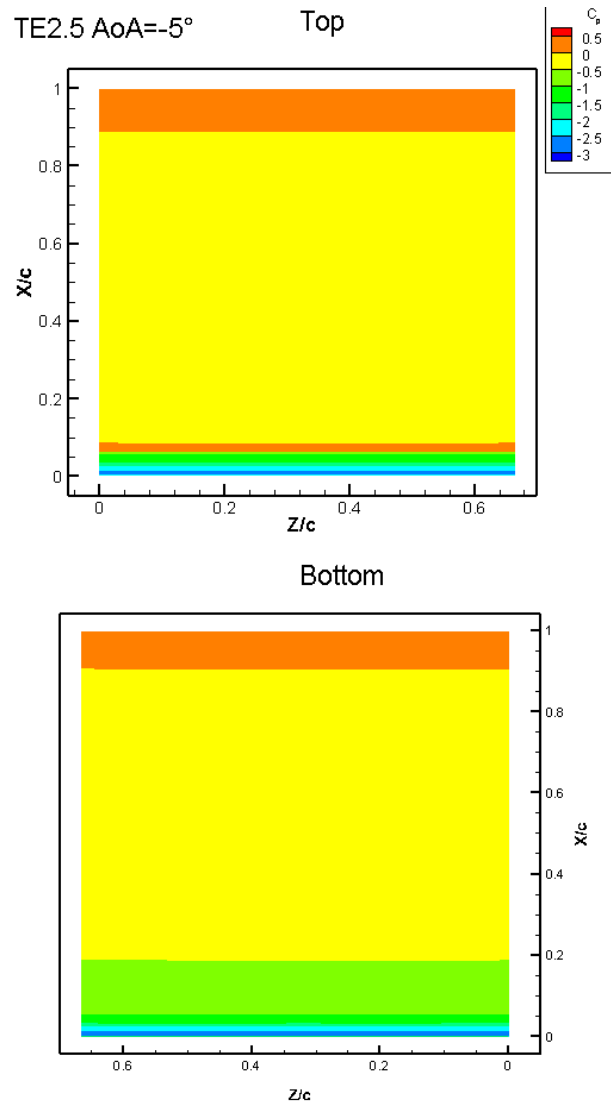**Fig. E1. Baseline VR-12 Coefficient of Pressure contours on the surface of the airfoil**
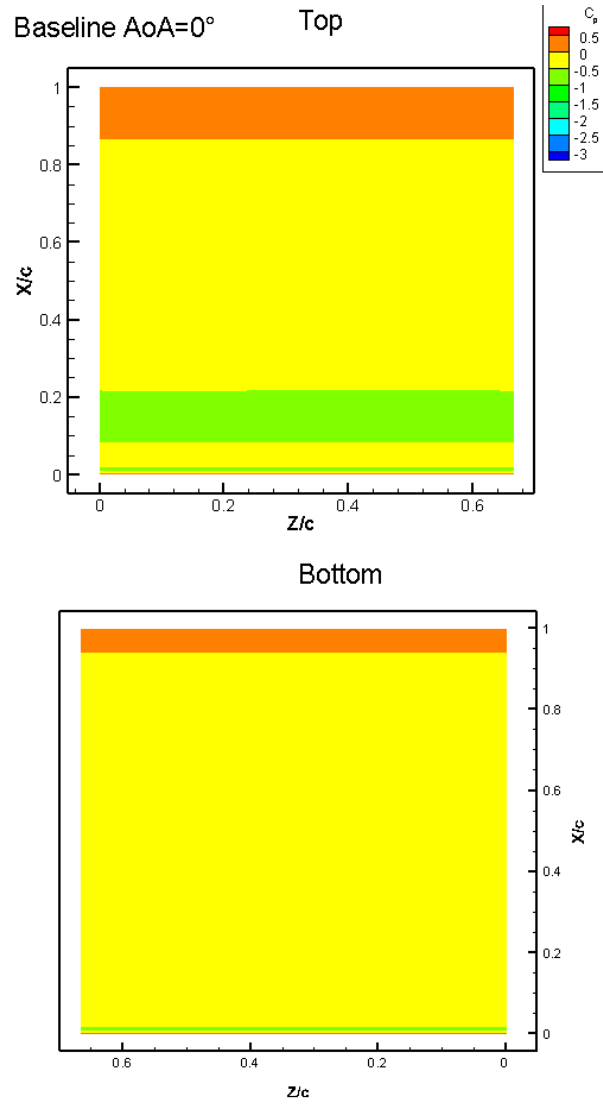
(b) 0° AoA

Fig. E1. Baseline VR-12 Coefficient of Pressure contours on the surface of the airfoil (continued)
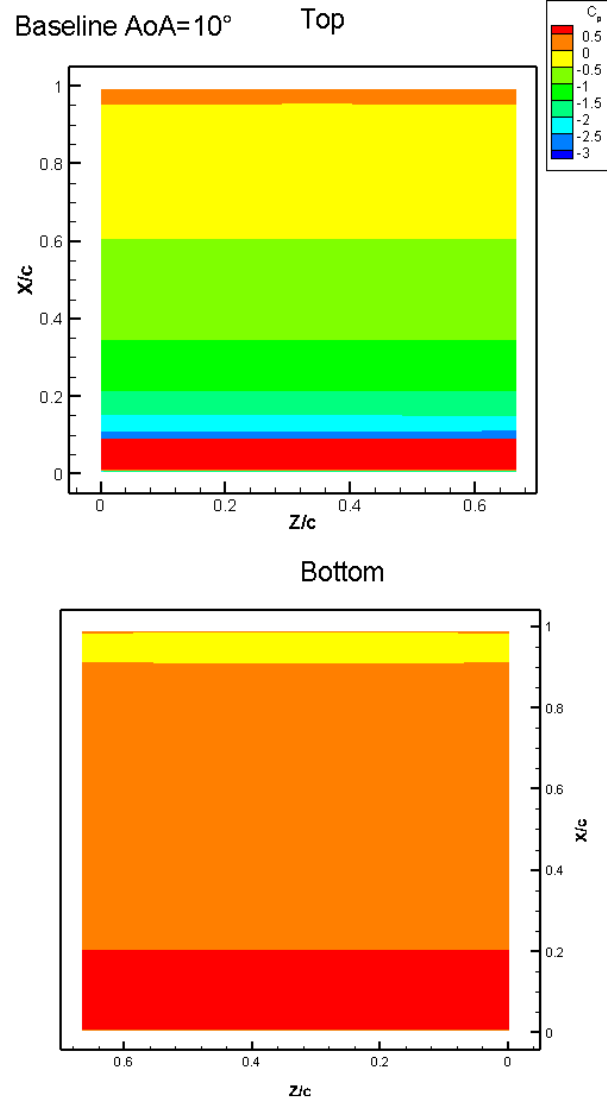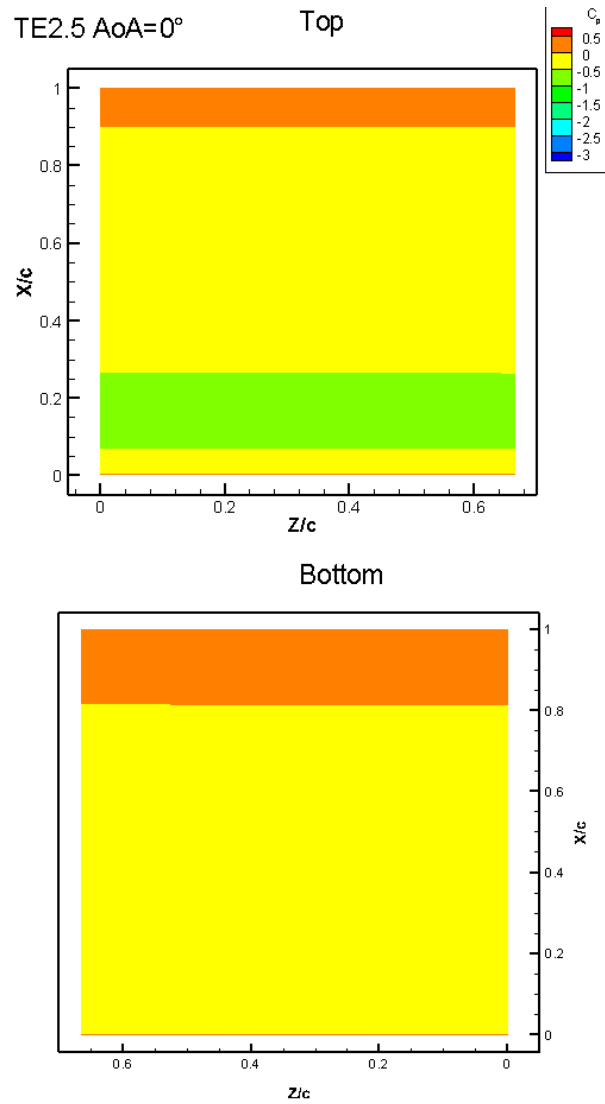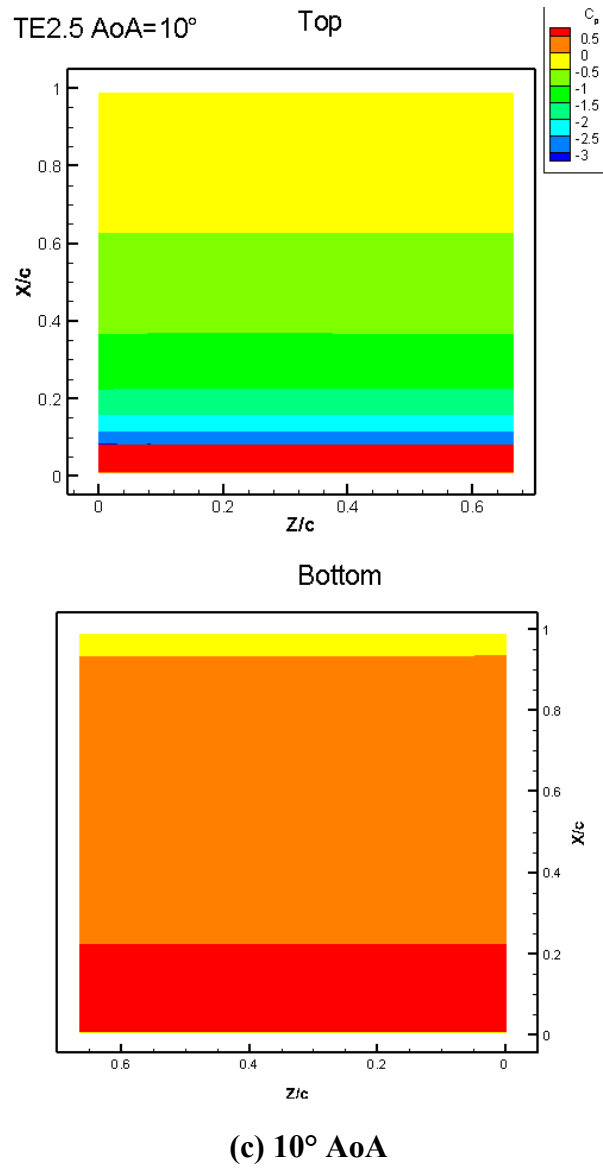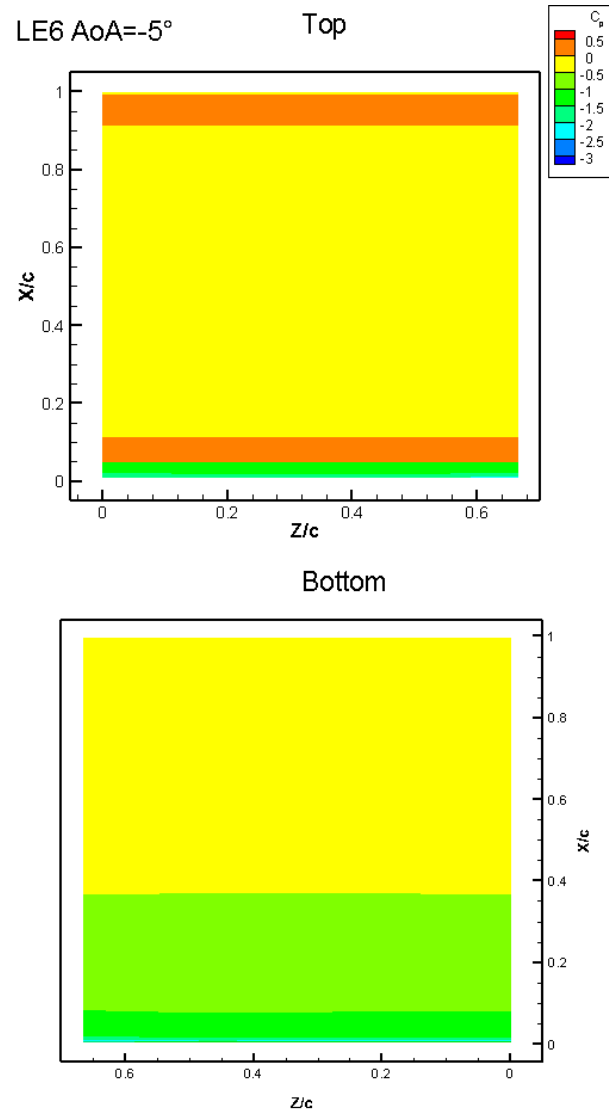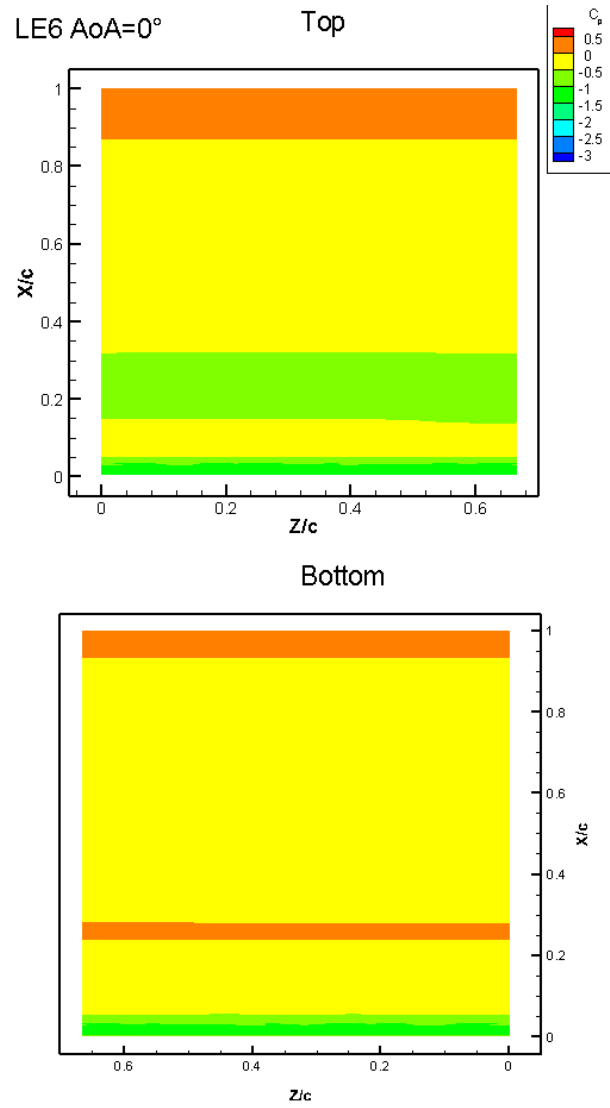
(c) 10° AoA

Fig. E1. Baseline VR-12 Coefficient of Pressure contours on the surface of the airfoil (continued)
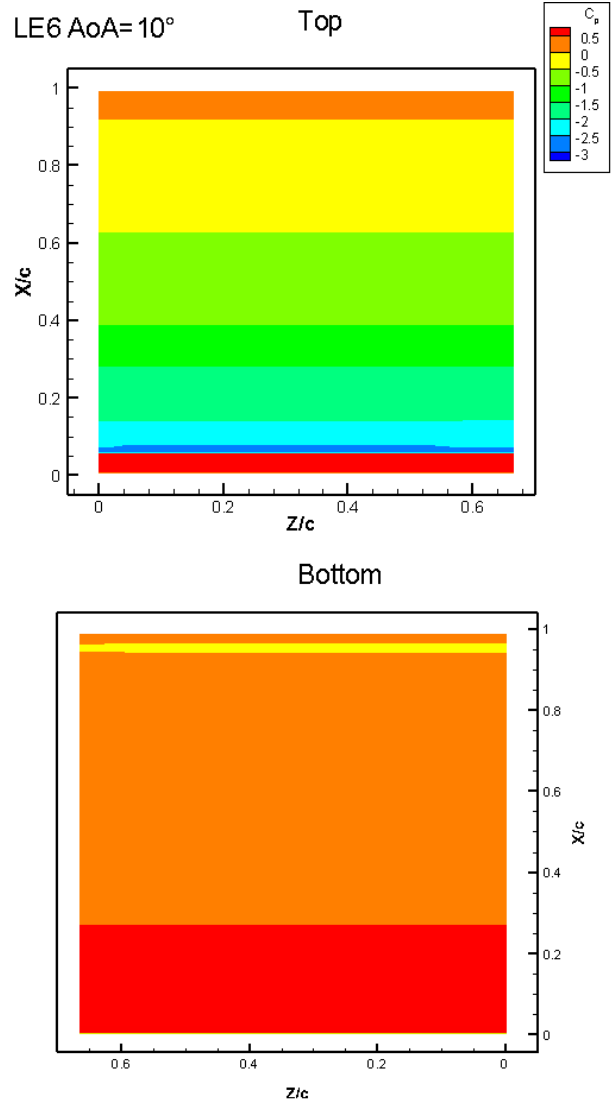
(a) -5° AoA

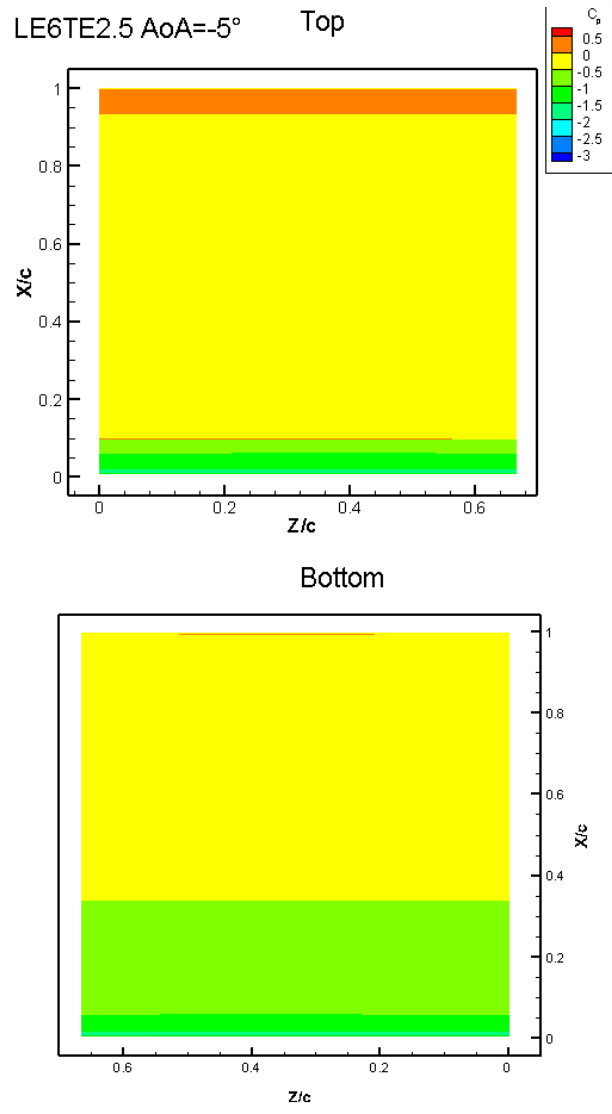**Fig. E2. TE2.5 Coefficient of Pressure contours on the surface of the airfoil**

(b) 0° AoA

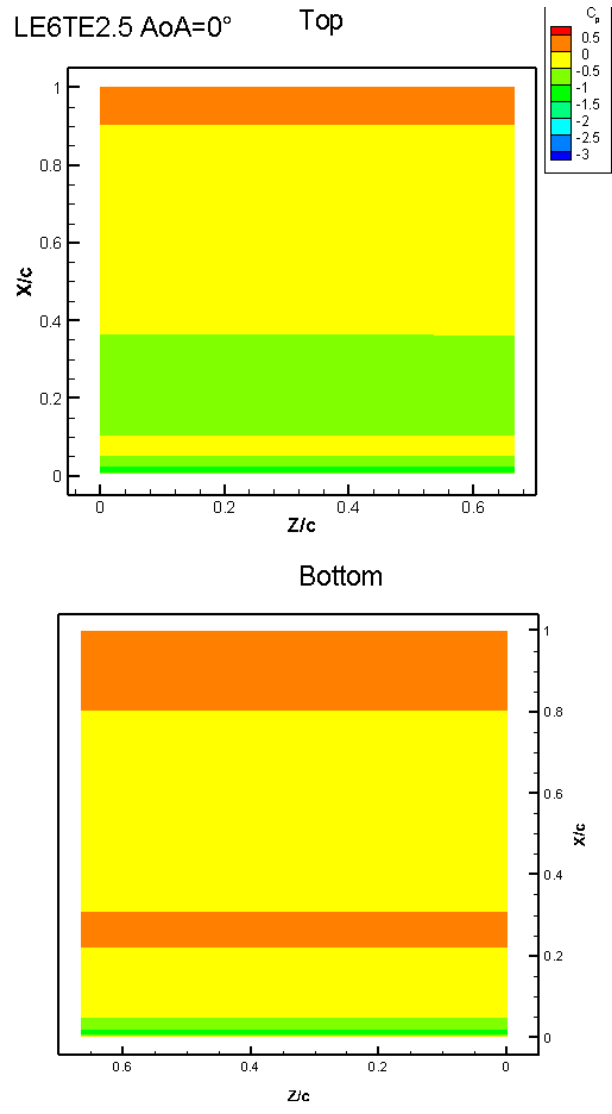**Fig. E2. TE2.5 Coefficient of Pressure contours on the surface of the airfoil (continued)**

(c) 10° AoA

Fig. E2. TE2.5 Coefficient of Pressure contours on the surface of the airfoil (continued)

(a) -5° AoA

Fig. E3. LE6 Coefficient of Pressure contours on the surface of the airfoil

(b) 0° AoA

Fig. E3. LE6 Coefficient of Pressure contours on the surface of the airfoil. (continued)

(c) 10° AoA

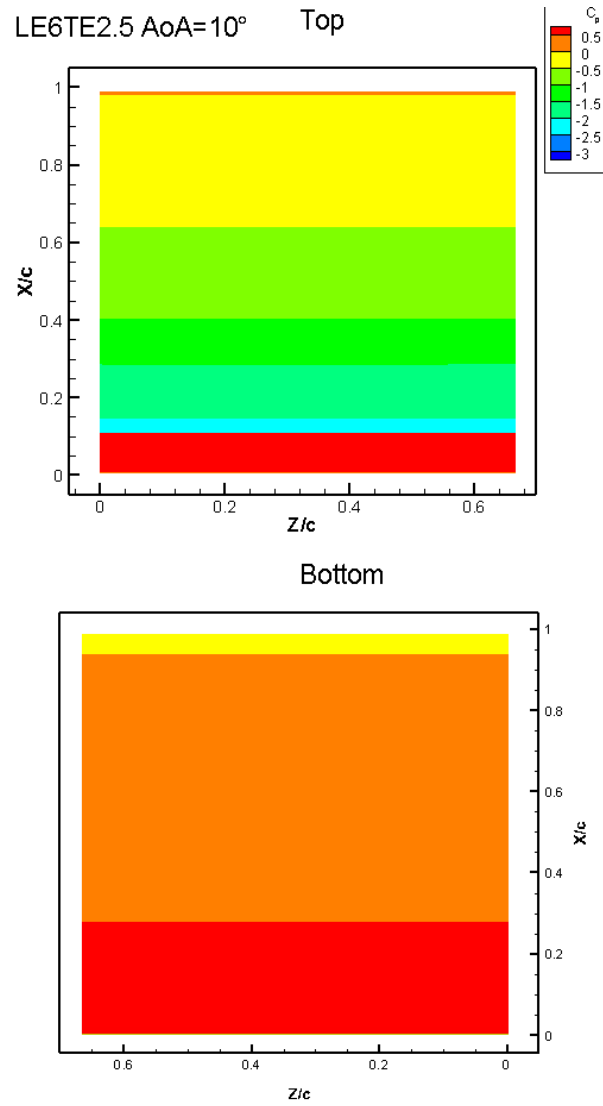**Fig. E3. LE6 Coefficient of Pressure on the surface of the airfoil. (continued)**

(a) -5° AoA

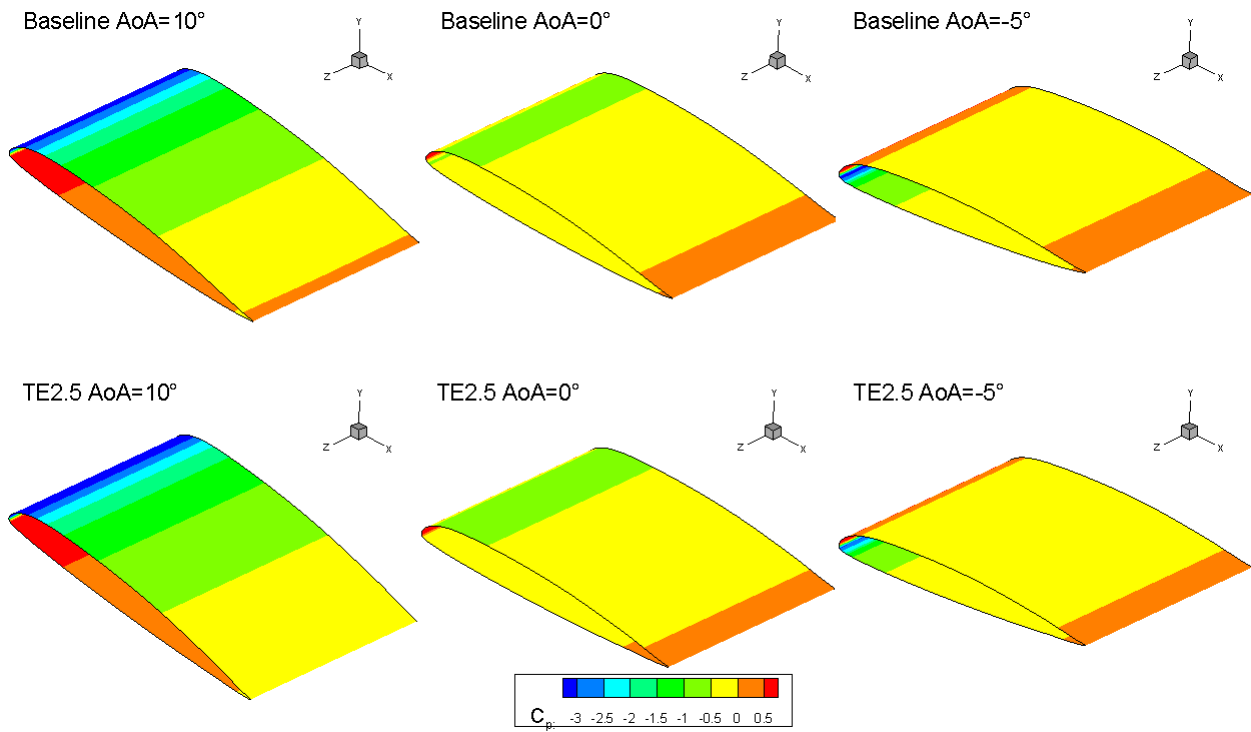**Fig. E4. LE6TE2.5 Coefficient of Pressure contours on the surface of the airfoil**

(b) 0° AoA

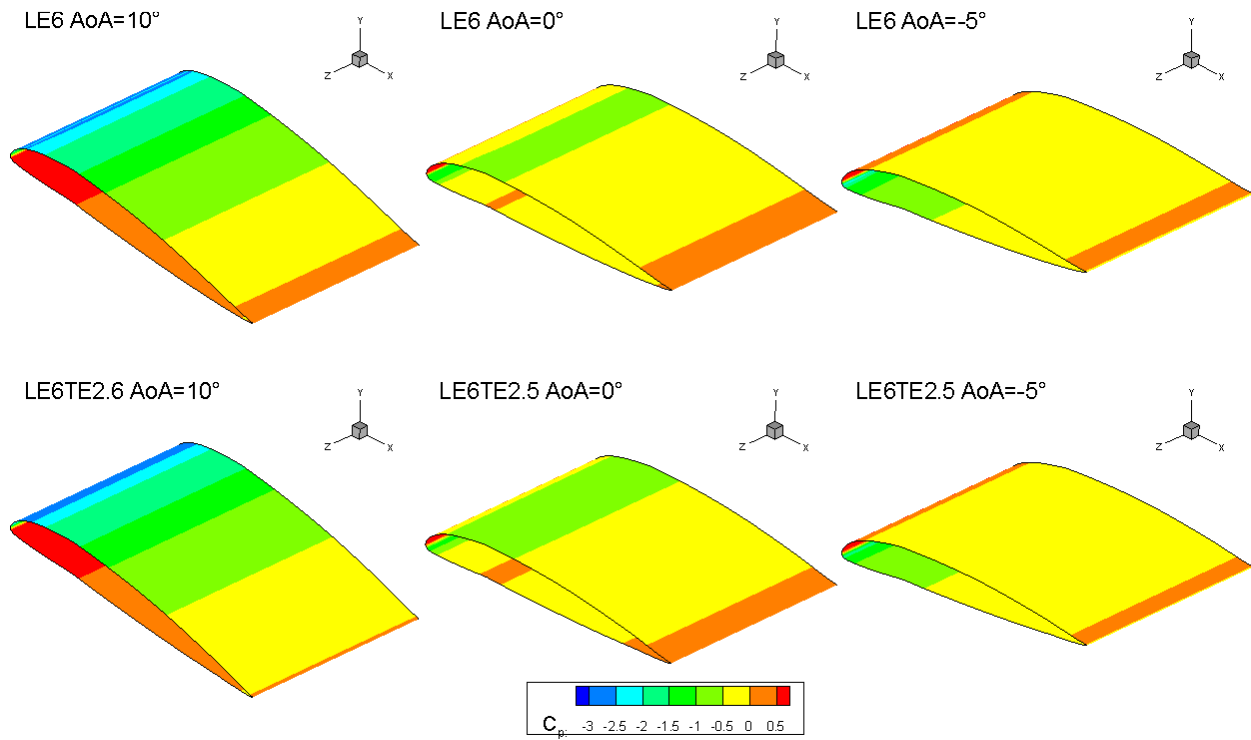**Fig. E4. LE6TE2.5 Coefficient of Pressure contours on the surface of the airfoil.
(continued)**

(c) 10° AoA

Fig. E4. LE6TE2.5 Coefficient of Pressure contours on the surface of the airfoil. (continued)

(a) Baseline and TE2.5

(b) LE6 and LE6TE2.5

Fig. E5. Isometric surface Coefficient of Pressure view of (a) Baseline an TE2.5 and (b) LE6 and LE6TE2.5 airfoils at -5, 0, and 10 degrees AoA.

124